Development of a Microwave Imaging System for Brain Injury

Guo, Wei

Awarding institution:
King's College London

Development of a Microwave Imaging System for Brain Injury

Department of Engineering

Wei Guo

King's College London

This dissertation is submitted for the degree of
Doctor of Philosophy

Declaration

I hereby certify that the contents of this dissertation are original and have not been submitted in whole or in part for consideration for any other degree or qualification in this or any other university, except for any particular references to the work of others. Except as otherwise noted in the text, everything in this dissertation is the result of my own work; it does not contain any material that was produced in partnership.

Wei Guo

Feb 2022

Acknowledgement

This journey to the completion of my Ph.D. would not have been possible without the participation of many, to whom I owe deep gratitude. First and foremost, I extend my sincere appreciation to my supervisor, Dr. Panagiotis Kosmas, whose insightful guidance, patience, and innovation were fundamental to this effort. His knowledge and wisdom were crucial in shaping this study and driving me to excel.

My heartfelt thanks go to my fiancée whose unwavering support, belief, and love have been a source of unending strength. This achievement is as much yours as it is mine. To Kiki, our dog, I extend my gratitude for your companionship and for the comfort you brought in times both challenging and joyful.

I am deeply indebted to Syed, Pan, Eleonora, Olympia, Ioannis, and Navid for their immense support and contributions. Their teachings have been invaluable to my growth and progression. Last but not least, my profound thanks to my parents for their absolute and continuous support throughout this Ph.D. journey. Your unwavering belief in me was the backbone of this accomplishment.

Abstract

This thesis presents the development of a microwave imaging (MWI) system for medical diagnostics, focusing on the design and optimisation of the antenna system. MWI technology offers several advantages over traditional imaging modalities, including safe radiation, compact and portable setups, low cost and real-time diagnosis. An efficient antenna operating within the desired MWI frequency spectrum is critical to the success of the MWI system.

The challenges of designing antennas for MWI systems are significant, and the research presented in [1]–[88] highlights the need for compact antennas due to the degree of ill-posedness of the inverse algorithm and the impact of the number and position of observations. A trade-off exists between penetration depth and imaging resolution, which necessitates an antenna operating at a compromised frequency. This frequency varies based on the dielectric properties of the brain tissue, requiring a wideband antenna operating at multiple frequencies. The number of frequencies used also affects the ill-posedness of the inverse algorithm, further emphasising the need for a wideband antenna. Our research specifically aimed to improve the antenna design of an existing MWI system to combat these challenges. Our proposed designs focused on optimising the dimensions of the antenna structures to achieve efficient operation in the 0.5 – 1.5 GHz frequency range, which is critical in microwave tomography.

The research is based on a comprehensive comparison of various antenna designs proposed in the literature, considering their size, operating frequency range, surface current, gain and other performance characteristics. During the research process, numerous antenna types were investigated but ultimately only printed monopole and aperture-coupled antenna were chosen due to their suitability for brain stroke detection.

This thesis focuses on the design and optimisation of the antenna system, with a particular emphasis on the printed monopole edge-coupled antenna (ECA) and aperture-coupled antenna (ACA). The thesis begins by describing the optimisation and dimensions of the proposed spear-shaped patch antennas using CST simulations. The performances of the proposed antennas were then compared by studying their radiation characteristics and transmission levels in the desired frequency range.

Various factors that affect the performance of our MWI system, including the detection capability of helmet-shaped vs headband-shaped scanners, the imaging sensitivity of edge-coupled arrays vs aperture-coupled arrays, and the effect of various absorbers and optimal antenna numbers in MWI scanners, were evaluated. The results showed that helmets with three rings of arrays exhibited higher transmission level differences between brains with and without targets. The effect of the absorber on the transmission level was minor. The transmission levels of the ECA arrays were higher than those of the ACA arrays. The imaging quality of ACA arrays was higher than ECA arrays due to the lower relative error and residual in ACA arrays. The 12-element antenna array is the optimal configuration for achieving the best imaging performance, compared to 8-element or 16-element antenna array. The return loss in simulation and experiments were also compared, with results suggesting good agreement between the two.

In addition to the primary contribution, the research also benefits from collaboration and interaction with other team members. This interdisciplinary teamwork informed the optimisation of the antenna design, further enhancing the performance of the microwave imaging system. Throughout this research, the author was involved in several aspects of the development of the MWI system, including simulation, experimentation and validation through the reconstruction algorithm. The author's focus on the team was on the antenna, including design, optimisation, feeding method and fabrication.

Table of Figures

Table of Tables

Table of Contents

Chapter 1 Introduction

1.1 Overview and Motivation

Microwave imaging (MWI) technology has been proposed as a promising modality for medical diagnostics because it relies on the potential to discriminate the dielectric properties between healthy and abnormal tissues [1]–[3]. In head imaging to detect stroke or haemorrhage, for example, MWI systems can feature safe radiation, compact and portable setups, low cost and real-time diagnosis [3]–[7]. These are important advantages relative to standard detection methods such as computed tomography (CT) and magnetic resonance imaging (MRI). Portable MWI brain scanners can be deployed easily in an ambulance, and their low power levels (between 0 – 20 dBm) make these scanners suitable for continuous monitoring purposes [8]–[10].

MWI for brain stroke utilises microwaves with low frequency, typically ranging from 0.3 GHz to 10.0 GHz [11]–[17], which can penetrate biological tissues with non-ionising radiation. Therefore, it is safe and convenient for brain stroke patients. Microwave imaging devices that are small and portable can be developed for continuous monitoring and used as an effective supplement to mature technologies, such as CT and MRI. Continuous monitoring is required to observe stroke areas once a brain stroke is detected. CT and MRI devices are bulky, and CT utilises ionising radiation, so they can't be used for continuous monitoring purposes [9], [10], [18]–[22]. In addition, microwave imaging technology has a high data acquisition speed and a low cost. This technology can usually collect data within milliseconds to seconds, which means its processing speed of this technology is limited only by the time needed for imaging reconstruction.

However, the penetration ability of microwaves is limited by the high attenuation of brain tissues [23]–[25]. Therefore, developing a good microwave imaging system that can solve the poor signal penetration problem is of vital importance.

Brain stroke is becoming one of the chief causes of dysfunction in the human brain and death worldwide [7], [8], [26]. There are two main types of brain stroke: ischemic, which occurs when the flow of blood is blocked, and haemorrhagic, which occurs when a blood vessel bursts. From the onset of stroke symptoms, each type of brain stroke requires timely and accurate (but different) treatment [22], [27]–[29]. An MWI method must take advantage of the inherent dielectric property contrast between the healthy brain and the stroke-affected tissue to produce a reliable diagnosis of the stroke type. To this end, MWI techniques based on either qualitative or quantitative approaches are currently being employed by various groups worldwide [30]–[33].

1.2 Literature Review

1.2.1 Microwave Imaging for Brain Stroke Detection

Early studies of medical microwave applications primarily focused on its therapeutic use. T. England, H. Cook and other researchers measured the dielectric properties of the body tissues and found it feasible to determine the characteristics in various parts of body using microwaves in 1951 [23]. Microwaves were first used in medical imaging in the 1970s. The Walter Reed Army Institute of Research(WRAIR, Silver Spring, MD, USA), L.E. Larsen and J.H. Jacobi quantified the effect of body tissue exposure to microwaves and rapidly applied this technique to their dosimetry project, calling it "the best hope for non-invasive dosimetry analysis of bio-systems exposed to microwave radiation" [34]. During the initial studies, microwaves were viewed as factors impacting body tissues, potentially resulting in modifications of the tissues' functions [35]–[37]. On the other hand, the microwave was used for medical detection purpose, which surpassed their dosimetry framework and is now considered as the triggering event of medical microwave imaging [38]–[41].

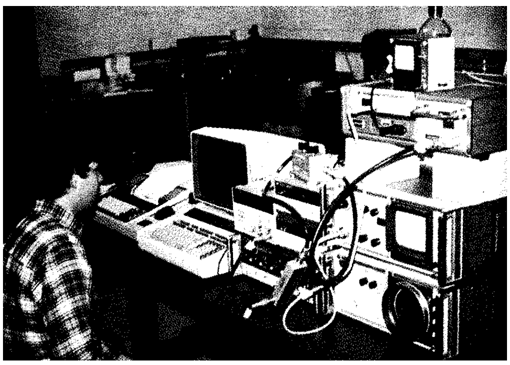

Figure 1.1 Early imaging experiment setup by Larsen and Jacobi [34].

Larsen and Jacobi successfully conducted microwave imaging detection experiments in 1979 for the first time on canine kidneys, which consist of high-water content tissues with a relative permittivity close to 80 [34]. With a simple experiment protocol, in which two antennas arranged confronting each other transmitted and received signals simultaneously in water, they obtained a clear microwave image with a good spatial resolution. Such good reconstruction of the spatial resolution was the result of applying the immersion technique, which provided four major favourable effects compared to operating in air. The first effect was improved spatial resolution, estimated at one and a half wavelengths. The second benefit was less reflection at the boundary of the organ; hence, more microwave signals penetrated the organ. Third, immersing in liquid led to strong attenuation of parasitic propagation outside the organ, resulting in lower mutual coupling between antennas and a reduction in undesired propagation outside the organ. The fourth advantage was that immersing in liquid decreased the operation wavelength from 77 mm in air to 8.5 mm in water, resulting in reduced antenna dimensions in same scenario. However, as a very early prototype, their imaging system required a lot of optimisations. The major drawback was the long duration, as it took approximately 4.5 hours. In addition, this early-stage study imaged an isolated animal organ, did not consider the complicated surrounding tissues and their system did not apply to human tissues, which have quite different relative permittivity. Despite these drawbacks, their experiments on animal tissue were considered the triggering point of experimental medical microwave imaging applications.

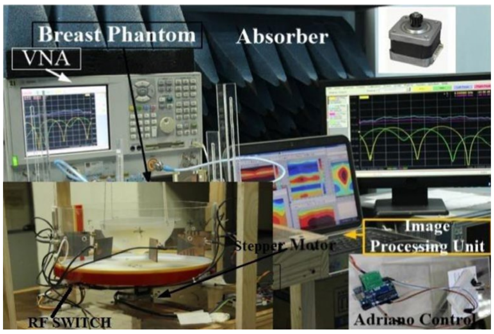

Figure 1.2 An experimental setup of breast imaging system by Islam *et al.* [42].

Since this first experimental trial, a series of medical applications has been studied. Breast imaging is one of the most widely investigated medical applications [42]–[47], [47], [48]. The objective of breast imaging is to detect cancer and tumour based on the relatively high dielectric property contrast between breast tumour and healthy fat tissues, which makes tumour stand out from healthy tissues. Two main methods have been applied to breast imaging. The first method is radar-based method [43]–[45], according to which various approaches have been used for breast imaging. These include confocal imaging approach, the Tissue Sensitive Adaptive Radar algorithm approach, the space-time beamforming approach and the multi-static adaptive microwave imaging approach. Tomographic technique has also been used for breast imaging by reconstructing the dielectric properties of breast area [46]–[48]. The tomographic approaches include Newton-type iterative algorithms, the Newton-type conjugate gradient method, the Gauss–Newton reconstruction, the distorted Born iterative method, and the CSI method [49]–[51].

Bone microwave imaging has been studied for detecting leukaemia in bone marrow and osteoporosis by imaging the dielectric property of bone [52], [53]. Leukaemia causes a significant increase in cellular population, which leads to increased relative permittivity and decreased conductivity by a factor of 2. In contrast, osteoporosis leads to a decreased number of cells in bone. Based on changes in dielectric property, the quantitative tomographic approach is used for bone imaging. Soft tissue and joint imaging are another microwave imaging technique applications [54]. Injuries of soft tissues are not detectable by X-ray. However, due to the existence of dielectric contrast, these abnormalities are detectable by microwave imaging technique although it might be difficult to pronounce a significant dielectric property difference between injuries and healthy tissues as the dielectric property contrast between heathy tissues and bones is higher. Heart imaging has also been investigated to detect any pathological conditions based on the dielectric property of myocardial tissues, which are strongly dependent on the blood flow of coronary [55].

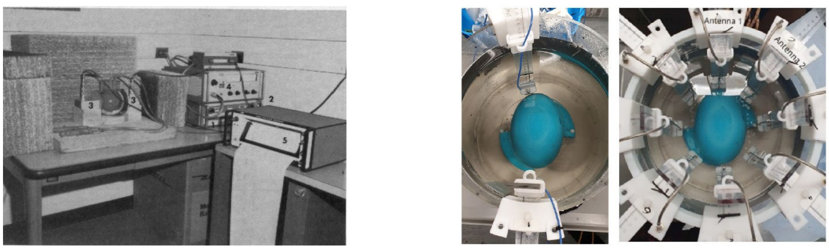

(a) (b)

Figure 1.3 Brain detection experimental setup (a) An early experimental setup of cerebral edema by James and Martin. [56] (b) Recent radar and tomographic brain detection scanner by N.Ghavami *et al.* [57].

Another important microwave imaging application is brain imaging, which is used to detect haemorrhagic or ischemic strokes based on blocked or burst blood vessels [56]. The first experimental work on brain tissue microwave imaging dates back to 1982, by James and Martin. They demonstrated the microwave imaging technique on detection and monitoring of cerebral oedema. Other studies followed, but most were conducted on simplified models or phantoms. Further and deeper studies on brain stroke imaging are currently being conducted around the world [4], [11], [57]–[61]. Many other biomedical body imaging applications are being studied based on the dielectric properties of various body tissues, showing the great potential of microwave imaging.

This emerging modality is still in its early days and much research needs to be carried out before clinical systems become widespread. A few critical challenges are being faced in the development of microwave imaging systems. Some of the key challenges are: 1) Complex layers of brain structure; 2) Requirement of matching medium; 3) Emergence of surface waves and multipath signals; 4) Need for a compact, robust and efficient antenna; and 5) Image resolution issues. We will thoroughly discuss the challenges in Chapter 2.

We proposed the final goal of designing a compact, novel and efficient microwave tomography system. Our prototype comprises of a compact printed monopole that exhibits a wideband response when immersed in an appropriate medium, thereby allowing us to work with multiple frequencies which is particularly useful in image reconstruction to address the ill-posed inverse problem. Our antenna operates in the 0.5 – 1.5 GHz frequency range, which can address image resolution (high frequency) and penetration depth (low frequency) issues. We have also studied the performance of our antenna in an array form with various coupling media to address the key challenges posed by the excitation of surface waves and multipath signal propagation.

1.2.2 Brain Stroke and Brain Phantom Preparation

Stroke is a leading cause of death and disability in developed countries, affecting approximately 16 million people worldwide each year, with 6 million deaths and another 6 million people becoming disabled [62]–[64]. Stroke is characterised by a sudden neurological disability caused by a disruption of blood flow to the brain and is mainly classified into two categories: ischemic and haemorrhagic. Eight percent of strokes are ischemic and 20% of them are haemorrhagic[28], [60], [62].

In developed countries, only 2–5% of ischemic stroke patients can be diagnosed and treated in time [63], [65]. Currently, MRI and CT are the available imaging modalities for diagnosing stroke, but they are not easily accessible or affordable for patients in rural hospitals and can only be performed once the patient is admitted to the hospital. According to European yearly statistics, the cost for around 0.8 million stroke patients have reached 60 billion euro [66]. The World Stroke Organisation (WSO) reports that reliable and affordable medical imaging systems are inaccessible to about 75% of the world's population [62]. Furthermore, existing imaging systems are often very bulky. Time is critical when it comes to beginning reperfusion to limit or reverse neurological disability. However, CT scans can be problematic due to radiation exposure and the risk of cancer [22]. MRI is a more expensive and less widely available option, while ultrasound imaging requires expertise and is time-consuming [21]. Although PET imaging has been used to assess the ischemic penumbra, it is not widely utilised [20]. Therefore, there is an urgent need for a portable, non-ionising, low-cost and highly accurate imaging system for the detection of stroke [1].

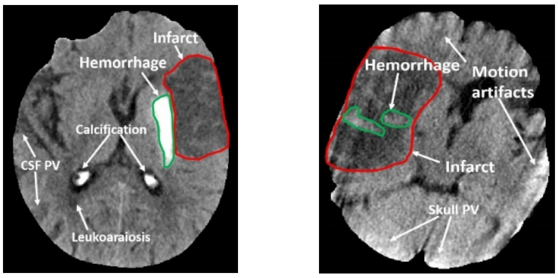

(a) (b)

Figure 1.4 Post-treatment NCCT scans of two AIS patients with manual segmentations of haemorrhage and ischemic infarct super-imposed. Red: ischemic infarct, green: haemorrhage [28].

Phantoms, which mimic the dielectric and structural characteristics of the human skull and brain, offer effective, simple-to-make, and inexpensive testbeds for experimental validation before clinical trials. In the paper by Hakala *et al.* [59], two phantom models were used for simulation and experimental study. The first phantom, called Phantom I, was a planar layer model resembling the brain. The second phantom, called Phantom II, was a hemisphere layer model resembling the head. The dimensions and dielectric properties of the layers were equal to those of the measurement phantom. In both models, the thickness of the cerebrospinal fluid (CSF) layer was gradually increased from 2.0 mm to 3.8 mm, with a step of 0.25 mm. The simulation results were evaluated based on antenna reflection coefficients S11 and time domain impedance results, as well as 2D power flow representations to illustrate propagation in the vicinity and inside the tissues within the selected dB range. Proper phantom preparation is crucial for accurate microwave sensing of brain water and the detection of brain abnormalities.

In a previous study by David *et al.*[9], an anthropomorphic phantom was used for the head. The phantom was a single-cavity container obtained through 3D printing in clear resin. It was filled with an alcohol–water mixture with a small percentage of sodium chloride to increase conductivity and mimic the dielectric properties of brain tissues. To simulate a stroke, a capsule-shaped balloon was employed, and a support was used to affix the capsule in the desired position. Different types of strokes exhibit distinct dielectric properties in the microwave frequency spectrum, and the target was filled or emptied with water–alcohol–sodium chloride mixtures, achieving the properties of haemorrhagic or ischemic stroke. The paper included a table with the corresponding dielectric parameters at 1.0 GHz (relative permittivity and conductivity) for the different liquid mixtures. The properties of the liquids were measured using the Keysight dielectric probe 85070D and the Keysight N1500A materials measurement software suite.

In a recent study by A. T. Mubasher [67], a 3-D voxel model of the human head was derived from 2-D MRI images at a 1 mm interval, and the layers of fat, skin, muscular parts, and skull were united to construct the exterior of the phantom. The brain part was subdivided into dura, CSF, grey matter, white matter, cerebellum and spinal cord portions, with separate volumetric binary models created for each subdivision. Tissue-mimicking materials were then developed using a combination of gelatine, water, agar, corn flour, propylene glycol, sodium azide and sodium chloride to fabricate low-cost tissue-equivalent materials such as grey matter, white matter, blood, dura, CSF, cerebellum, spinal cord, and eyes. Electrical properties were measured using a dielectric probe HP85070 with the help of a network analyser over a frequency band of 0.5 – 4.0 GHz. Comparisons between the actual electrical properties and the developed tissue-mimicking materials showed reasonable similarities. The whole phantom development procedure was exhibited in a series of photographs taken during different fabrication steps. The developed phantom demonstrated stability in terms of electrical properties, with only a 10 – 15% decrease observed after several months; it tended to reach stable values. Overall, the developed brain phantom offers a valuable tool for testing and optimising medical imaging and neurophysiological techniques.

In conclusion, the development of realistic phantoms for brain stroke detection is a crucial step in advancing research in this area. The use of 3D printing technology and tissue-mimicking materials enables the creation of phantoms with realistic electrical properties and anatomy. By following careful fabrication procedures and selecting appropriate materials, researchers can create phantoms that closely mimic the properties of human tissue. These phantoms can be used for a range of applications, including the testing of medical devices and imaging techniques. The advancements in phantom fabrication techniques and materials discussed in this literature review offer a promising avenue for continued research in the field of brain stroke detection.

1.2.3 Experimental Setup

As one of the most important applications of medical microwave imaging, the diagnosis of the brain area has attracted people's attention widely due to the large contrast in dielectric property between brain tissues and water from early studies. Existing imaging systems can be categorised into two types according to their algorithm type: classification and image reconstruction.

The objective of classification systems is to diagnose the type of abnormality in a patients' brain (either ischemic or haemorrhagic, either brain stroke or traumatic injury) and indicate of a rough location of the abnormalities. For example, Medfield Diagnostics developed a portable classification imaging system called Stroke Finder [67]. The system comprises 8 slot antennas working at 0.4 GHz to 2.0 GHz, which can be adjusted to the individual head accordingly. They are designed to fit this system into an ambulance to diagnose the occurrence or non-occurrence of brain bleeding. Preclinical tests began in 2008, and the system has undergone trials on over 100 volunteers.

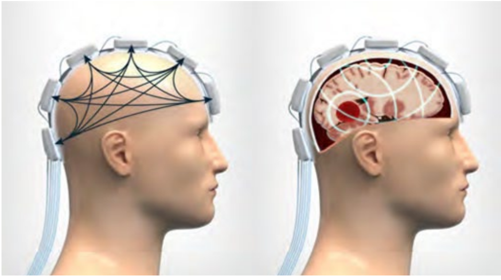

Figure 1.5 A microwave imaging system prototype proposed by Persson *et al.* [67].

Recently, several microwave imaging system prototypes have been designed and described in the literature. A promising MWI system was developed at Chalmers University [3]. This prototype system consists of 10 triangular patch antennas mounted inside a bicycle helmet. A brain phantom with the same properties as a realistic brain was created by mixing sugar, salt, water and agar. Plastic bags filled with coupling liquid were put between antenna and brain phantom. The MWI system operates between and 0.8 GHz and 1.5 GHz, and stroke detection was performed by measuring the scattering matrix and inputting the matrix into a machine-learning algorithm based on training. This paper pointed out that distance and conductivity together determine at which frequency the maximum transmission was obtained.

Another MWI system was developed at the University of Queensland to detect intracranial hematomas [6]. This detection system comprises 16 corrugated and tapered slot antennas in a ring and operates between 1.0 GHz and 2.0 GHz (low microwave frequencies can penetrate the human head due to their longer wavelengths as described by the author). The antennas were in the air and no matching medium was employed. The distance of neighbouring antennas was chosen to have a mutual coupling lower than 20 dB over the band 1.0 – 4.0 GHz, and the stroke imaging relies only on monostatic data.

More recently, another system prototype has been developed, the “BRIM G2” at EM Tensor [5]; it was meant for imaging purposes as well. This system comprised 177 ceramic-loaded rectangular waveguide antennas mounted on a semi-spherical stainless-steel chamber. The antennas were evenly spaced on eight rings, at different heights. The working frequency was 1.0 GHz. The matching medium was a mixture of glycerine and water. The large number of antennas employed in this system ensured the likelihood that it would acquire all the available information content for imaging purposes. However, this had some obvious drawbacks, at least in terms of cost and portability.

Another type of imaging system deployed an inverse scattering algorithm to reconstruct a detailed image of the whole brain area. The EM Tensor company constructed an imaging chamber comprising five rings of 32 waveguide antennas, resulting from research conducted since the mid-1990s. They applied an iterative nonlinear algorithm to estimate the dielectric properties of patients' brain tissues. After finishing their initial assessment, they are now conducting preclinical trails.

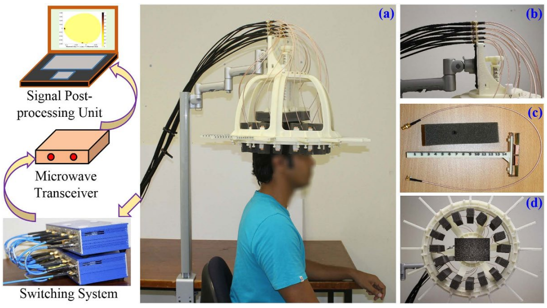

(a)

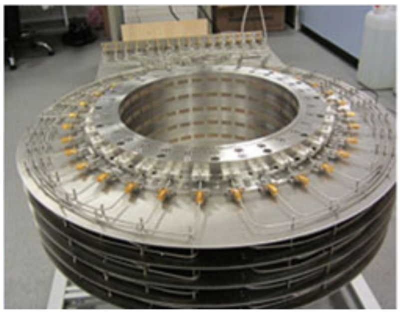

(b)

Figure 1.6 Experimental setup illustration: (a)Multi-slice microwave-based head imaging system [6]; (b) EM Tensor imaging chamber [5].

On the other hand, there are many other classification methods. For example, current imaging systems can be classified by their usage, whether they are intended for monitoring purposes, quick diagnosis or accurate detection. Imaging systems for monitoring purposes need comparatively fast, low spatial resolution. An imaging system for quick diagnosis needs a result that is highly accurate, but that has low spatial resolution and features good classification. Imaging system focusing on accurate detection demand more precise and robust imaging results for the brain area.

Previous studies have demonstrated the potential of microwave imaging. Some of their prototypes were even tested by hundreds of volunteers. However, there is much room for improvement including increasing spatial resolution, reducing processing time, etc. There is long way to go before a robust microwave imaging system is developed. Our preliminary study mainly focused on constructing a portable imaging system with 8, 12 or 16 antennas immersed in a glycerine–water mixture to reconstruct brain images using our previously developed algorithms.

1.3 Challenges of Optimising Microwave Imaging System

1.3.1 Frequency-dependent Dielectric Property

Accurately distinguishing between healthy and abnormal tissues in the brain can be challenging due to the subtle differences in these tissues and the presence of multiple tissue types, which create a complex scattering environment [25]. The frequency-dependent nature of tissues can also hinder accurate imaging. Researchers have devised several strategies to address this issue, such as using broadband microwave frequencies and advanced signal processing algorithms [68]. To achieve accurate reconstruction through algorithm, it is essential to model the frequency-dependent dielectric properties of the tissues, which requires the use of advanced mathematical models to account for complex scattering and absorption phenomena.

Kramers–Kronig relations [69] dictate that permittivity or conductivity vary independently with frequency. Modelling a material with a constant relative permittivity can lead to errors, which can result in an inaccurate model response for our finite-difference time-domain simulations [70]–[72]. The relations for dielectrics provide necessary connections among permittivity, conductivity and frequency; they are given as:

$$\varepsilon'(f) - \varepsilon_\infty = \frac{2}{\pi}\int_0^\infty \frac{x\varepsilon''(x)}{x^2 - f^2}dx$$

$$\varepsilon''(f) - \sigma_s/\omega\varepsilon_\infty = \frac{-2f}{\pi}\int_0^\infty \frac{\varepsilon'(x) - \varepsilon_\infty}{x^2 - f^2}dx$$

, where $\varepsilon'(f)$ is related to the refractive index, $\varepsilon''(f)$ is associated with the absorption or gain coefficient and x is the angular optical frequency variable, running through the whole integration range.

In recent studies, the Debye model and Cole–Cole model have commonly been used to model the frequency-dependent nature of brain tissues [72], [73]. The N-pole Debye model is described as follows:

$$\varepsilon_{\mathrm{D}} = \varepsilon_{\infty} + \sum_{i}^{N} \frac{\Delta\varepsilon_{\mathrm{i}}}{1 + \mathrm{j}\omega\tau_{i}} + \frac{\sigma}{j\omega\varepsilon_{o}}$$

, where ε_o is the free-space permittivity, ω is the angular frequency, ε_s is the static relative permittivity, ε_∞ is the high frequency permittivity, $\Delta\varepsilon_{\mathrm{i}} = \varepsilon_s - \varepsilon_\infty$ is the change in relative permittivity due to the Debye pole and τ_i is the i-th relaxation time constant and σ the static ionic conductivity. The N-term Cole–Cole model is defined by:

$$\varepsilon_{\mathrm{C}} = \varepsilon_{\infty} + \sum_{i}^{N} \frac{\Delta\varepsilon_{\mathrm{i}}}{1 + \mathrm{j}\omega{\tau_{i}}^{1-\alpha_{i}}} + \frac{\sigma}{j\omega\varepsilon_{o}}$$

, which has the same parameter definitions as the Debye model, but with an additional exponent parameter that allows for broadening the i-th dispersion. Although this exponent term provides more accurate model to the material permittivity, the Cole-Cole model is difficult to implement due to the challenge of applying Fourier transform to it.

For this study, the approximations of the Debye model of various brain tissues were obtained from the Gabriel & Gabriel database over a broad range of frequencies [25]. This database contains anatomically accurate MRI-derived numerical phantoms that are commonly used for brain detection and treatment applications. The brain tissues in these phantoms have realistic and ultra-wideband dielectric properties.

1.3.2 Spurious Radiation Issue of Printed Monopole Antenna

Spurious radiation in edge-fed printed monopole antennas can be a critical issue in microwave imaging systems designed for brain stroke detection [74]–[77]. In microwave imaging systems, it is crucial to achieve high accuracy and resolution to ensure effective diagnosis and treatment. Spurious radiation can lead to imaging artifacts and lower the signal-to-noise ratio, which can impair the accuracy of the system. Edge-fed patch antennas are more prone to spurious radiation due to the presence of discontinuities in the feed network. This can result in unwanted radiation from the feed network, leading to higher sidelobe levels and reduced imaging quality.

Aperture-coupled feeding methods provide an effective solution to this problem, as they minimise spurious radiation in patch antennas [78]–[81]. The use of a symmetric aperture that is centred under the patch ensures that the electric field coupling from the feed line to the radiating patch is purely perpendicular to the patch surface. This reduces cross-polarisation and leads to lower sidelobe levels. Additionally, the ground plane that separates the patch and the feed line helps to minimise spurious radiation by reducing the coupling between the patch and the feed network.

For a microwave imaging system designed for brain stroke detection, the elimination of spurious radiation is crucial to achieving high accuracy and resolution. The use of aperture-coupled feeding methods can provide better isolation between the feed line and the radiating patch, reducing the impact of spurious radiation. This, in turn, can improve imaging quality and enhance the diagnostic accuracy of the system. Furthermore, the higher directivity and lower cross-polarisation achieved by aperture-coupled antennas make them well-suited for precise beam steering, which can be useful in detecting the location and extent of a brain stroke.

1.3.3 Substrate of Antenna

The selection of the substrate is a crucial step in the design of antennas. The substrate is an essential part of the antenna structure and contributes significantly to the radiative properties of the antenna. The substrate material affects the antenna’s radiation efficiency, impedance bandwidth, and directivity [77], [81]–[83]. Hence, it is important to choose the substrate material wisely based on the application requirements.

One of the key factors in selecting the substrate is the dielectric constant. A lower dielectric constant is desirable, as it promotes fringing fields and hence radiation. A substrate with a low dielectric constant reduces the capacitance between the patch and the ground plane, which in turn increases the antenna’s radiation efficiency. Generally, a lower dielectric constant is preferred, because it can promote fringing fields and lead to better radiation. However, if the dielectric constant is too low, this can result in increased surface wave losses and reduced bandwidth, which can adversely affect the antenna's performance. Hence, selecting a substrate with an optimal dielectric constant requires finding a balance between promoting fringing fields and minimising losses to ensure that the antenna operates with high efficiency across a broad range of frequencies.

The thickness of the substrate is also a critical factor in antenna design. A thicker substrate increases the antenna’s impedance bandwidth, which is beneficial for broadband applications. However, using a thick substrate can cause impedance mismatch issues, which can lead to reduced radiation efficiency. In addition, a thick substrate can also lead to reduced accuracy in reconstruction, as antennas are approximated infinitely thin in the reconstruction algorithm.

Another critical factor in substrate selection is loss tangent. A high loss tangent leads to increased losses and reduced efficiency, particularly at higher frequencies. Therefore, it is crucial to select a substrate with a low loss tangent to achieve better performance.

The selection of the substrate is a crucial step in antenna design. The choice of substrate material depends on the specific application requirements, and a careful evaluation of the different factors discussed above can help in selecting the most appropriate substrate for the antenna design.

1.3.4 Optimal Frequency for Microwave Imaging

In microwave imaging for brain tissue property reconstruction, the selection of an optimal frequency range is a critical aspect of the design process.

Although higher frequencies can offer enhanced resolution, several factors limit their ability to reconstruct brain tissue properties accurately. One such limitation is attenuation, which increases with frequency. Specifically, the tissues absorb higher-frequency signals more readily, leading to weaker signals received by the antennas [23], [24], [43]. This increased attenuation negatively impacts penetration depth, making it challenging to image deeper brain structures using high-frequency signals. Another challenge associated with higher frequency signals is scattering caused by smaller tissue inhomogeneities. Such scattering can distort the signal, complicating the accurate reconstruction of tissue properties. This is particularly true in complex structures such as the brain, which exhibits considerable heterogeneity. Moreover, higher-frequency signals are generally more susceptible to noise, both from the imaging system and from external sources [84]. A low signal-to-noise ratio can lead to artifacts in the reconstructed images, making it difficult to accurately discern tissue properties.

Lower frequency signals inherently possess longer wavelengths, which restrict the achievable spatial resolution [77], [85]. Consequently, accurately identifying and characterising small or closely spaced tissue structures in the brain may prove difficult. Additionally, the dielectric properties of biological tissues might not exhibit significant contrast at lower frequencies. This lack of contrast makes differentiating between various tissue types based on their electromagnetic properties challenging, potentially impacting the effectiveness of microwave imaging techniques in distinguishing between healthy and pathological tissues. Furthermore, lower frequencies can lead to challenges in effectively coupling the microwave energy to the tissue due to the relatively large near-field region of the antennas compared with the dimensions of the imaging target, such as the brain. This factor can result in increased sensitivity to the positioning and design of the antennas. Lastly, lower frequency systems typically necessitate larger antennas and components, which can increase the overall size and complexity of the imaging system. This could limit the practicality of the system, especially for portable or wearable applications. Despite these limitations, lower-frequency microwave signals (in the range of hundreds of MHz to a few GHz) are often favoured for imaging brain tissue properties. They offer better penetration depth and lower attenuation compared to higher-frequency signals. Ongoing research continues to explore different frequency bands and imaging techniques to improve microwave imaging performance for brain tissue reconstruction while addressing these limitations.

In light of these challenges, selecting an appropriate frequency range for microwave brain imaging is crucial to achieving a balance between resolution, penetration depth, and signal quality. Frequencies higher than 1.5 GHz cannot be used due to low transmission levels in the inspected area, as high-frequency waves with shorter wavelengths can be easily absorbed or scattered by complex brain tissue. However, frequencies below 500 MHz do not provide sufficient image resolution for the imaging system. The frequency range of 0.5 GHz – 1.5 GHz is particularly promising, as it provides both good imaging resolution and sufficient penetration depth in brain tissue. Frequencies within this range are the primary focus of investigation in this study.

1.3.5 Coupling Liquid

The use of a coupling liquid in microwave imaging systems has many important functions. It can improve coupling efficiency, reduce mutual coupling, provide a stable interface between the antennas and the object being imaged, minimise the effects of reflections and scattering, and prevent antennas from overheating [39], [86]–[88]. In microwave imaging of biological tissues such as the brain, where there can be significant variations in tissue properties and geometry, the coupling liquid can play a crucial role in achieving accurate imaging results. However, the lossy nature of the coupling liquid can also attenuate microwave signals and affect the accuracy of the imaging process. Thus, selecting the appropriate coupling liquid is critical to achieving optimal imaging performance. Additionally, optimising the antennas to work in the coupling liquid used in the imaging system is essential for achieving accurate microwave imaging of the brain area.

1.4 Current Stage of Study in a Typical Evolutionary Timeline

The evolution scheme of imaging modalities (ultrasound [12, 13], MRI [14], or PET [15]) follows the same timeline if we take a careful look at their history. Microwave imaging modality is no exception.

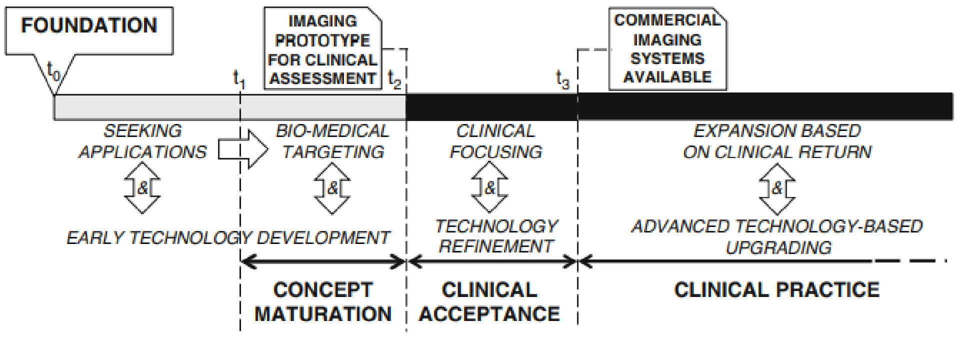

Figure 1.7 Evolutionary timeline.

At the start of the evolution scheme of imaging, there is usually great progress in fundamental theories; these theories are considered the foundation of the imaging modality. During this very early stage of evolution, researchers start seeking applications based on the foundational technology. Following the foundation discovery, several related applications emerge into one application, which is targeted at specific bio-medical issues and enters the concept maturation stage at time t_1. The targeting process is achieved by preliminary investigation and a feasibility assessment of body tissues or animals. Successful validation of concept applications may result in early prototypes, which can be used as a clinical method on volunteers. At time t_2, application evolution enters the clinical acceptance stage, which focuses on the practical feasibility and optimisation of the technology. In this period, long-term, large-scale and multicentre diagnoses are tested on representative patients. Third, commercial devices are manufactured and introduced in clinics at time t_3. Diagnosis machines are upgraded thanks to clinical return.

In 1887, the existence of electromagnetic waves was demonstrated by Heinrich Hertz through experiments at submeter wavelengths. These wavelengths correspond to the lower-frequency part of the microwave spectrum, spanning from 300 MHz to 300 GHz. From the discovery of microwaves, which is treated as t_0 in a typical evolutional timeline, a series of applications was developed based on the microwave spectrum, including long-distance signalling, wireless powering, long-distance localising and short-distance sensing. With the short-distance microwave sensing application, investigators found a significant dielectric property contrast between healthy and cancerous body tissues.

Exploiting this dielectric contrast, researchers proposed the application of medical microwave imaging, which is considered time t_1. Evolution now moves to the second stage, the concept maturation stage. At this stage, dielectric contrasts of different parts of the body were measured, although there were inconsistencies across the various studies. Based on reported dielectric properties, researchers began to apply medical imaging to a specific part of the body, e.g., breast, lung and brain area, etc.

Detecting the brain area is one of the most challenging tasks, as the head structure consists of many layers, including hair, skin, skull, grey matter, white matter, etc. The dielectric properties of the frontal lobe, parietal lobe, occipital lobe and temporal lobe vary from each other, and even the dielectric properties of tissues in one brain lobe are different. Due to the high complexity of the brain structure, a more accurate and sensitive microwave imaging system needs to be designed to detect the abnormalities inside brain area, i.e., we need to design a more effective antenna, model a more stable imaging setup and develop a more precise algorithm to perform accurate imaging of the brain area. Until now, researchers, including our team, have been engaged in detecting brain areas with microwave imaging. Hopefully, this evolution of microwave imaging applications will move to next stage soon.

1.5 Contributions and Relevant Publications

The primary contribution of this research lies in the antenna design, which substantially impacts the overall performance of the microwave imaging system. Throughout the study, several antenna types were examined, such as antipodal Vivaldi, dielectric resonator, microstrip antenna, and coplanar waveguide antenna, *etc*. However, these antennas exhibited suboptimal performance, as they were either too large or operated outside the desired frequency range. As a result, this thesis does not delve into the design and optimisation details for these antennas.

Instead, the focus of this thesis is on two antenna types that demonstrated superior performance in terms of their characteristics and imaging quality. These antennas were specifically designed and optimised to meet the requirements of the microwave tomography system, ensuring efficient operation within the desired frequency range and the delivery of high-quality imaging results. This research significantly contributes to the field of microwave imaging technology by concentrating on the development and optimisation of these two antenna types, ultimately enabling the creation of more efficient and effective imaging systems for a variety of applications.

In addition to the primary contribution, a notable secondary contribution of this research is the collaboration and interaction with other team members. This collaboration involved conducting experimental setup discussions, algorithm application, imaging scanner design, phantom preparation, and laboratory measurements. This interdisciplinary teamwork provided valuable insights that informed the optimisation of the antenna design, further enhancing the performance of the microwave imaging system.

The thesis' contributions are listed below:

• A comprehensive research review on antenna design has been presented, covering various potential antenna types and designs for our microwave imaging systems. Antenna optimisation methods have been proposed to develop and validate the performance of antennas (Chapter 2).

• Printed Monopole Antennas for microwave tomography in the operating frequency range of 0.5 - 1.5GHz have been designed and analysed, specifically for our microwave imaging system (Chapter 3).

• A novel aperture-coupled feeding method is proposed, resulting in enhanced performance and versatility for microwave imaging (Chapter 4).

• Simulations and results for 8, 12, and 16 element antenna arrays in immersed configuration are presented. Investigations into the optimal number of antennas in the array and transmission coefficient magnitude differences between scenarios with and without targets are conducted to validate the feasibility of the antenna array (Chapter 5).

• Dielectric properties of brain areas are reconstructed using the existing DBIM imaging algorithm to validate the imaging capability of the antenna arrays and demonstrate their potential for practical applications in microwave imaging (Chapter 6).

Publications:

1. W. Guo, S. Ahsan and P. Kosmas, “Portable Microwave Imaging Head Scanners for Intracranial Haemorrhagic Detection,” *2019 IEEE Asia-Pacific Microwave Conference (APMC)*, 2019, pp. 670-672, doi: 10.1109/APMC46564.2019.9038721.

2. W. Guo, S. Ahsan, M. He, M. Koutsoupidou and P. Kosmas, “Printed Monopole Antenna Designs for a Microwave Head Scanner,” 2018 18th Mediterranean Microwave Symposium (MMS), 2018, pp. 384-386, doi: 10.1109/MMS.2018.8611962.

3. S. Ahsan, W. Guo, O. Karadima and P. Kosmas, “Experimental Comparison of Two Printed Monopole Antenna Designs for Microwave Tomography,” 2019 IEEE Asia-Pacific Microwave Conference (APMC), 2019, pp. 500-502, doi: 10.1109/APMC46564.2019.9038734.

4. Razzicchia, Eleonora, Pan Lu, Wei Guo, Olympia Karadima, Ioannis Sotiriou, Navid Ghavami, Efthymios Kallos, George Palikaras, and Panagiotis Kosmas. 2021. “Metasurface-Enhanced Antennas for Microwave Brain Imaging”, *Diagnostics* 11, no. 3: 424. https://doi.org/10.3390/diagnostics11030424

5. N. Ghavami *et al.*., “The Use of Metasurfaces to Enhance Microwave Imaging: Experimental Validation for Tomographic and Radar-Based Algorithms,” in IEEE Open Journal of Antennas and Propagation, vol. 3, pp. 89-100, 2022, doi: 10.1109/OJAP.2021.3135146.

1.6 Thesis Structure

The thesis is structured as follows: Chapter 1 provides an introduction, overview, and motivation for the study. It discusses the challenges of optimizing microwave imaging systems, such as frequency-dependent dielectric properties, spurious radiation issues, and substrate selection, and it reviews the current stage of research in the field. Chapter 2 delves into the background and methodology, exploring various current biomedical antennas for microwave imaging. The chapter also discusses antenna design techniques and optimisation methodologies, such as equivalent circuit models, impedance matching, and numerical analysis of scattering parameters. Chapter 3 focuses on the design of a printed monopole patch antenna. This chapter evaluates the antenna's performance by analysing its reflection coefficient, radiation resistance, and radiation efficiency. It also compares the printed monopole antenna to microstrip antennas in terms of complex impedance and electric field distribution. In Chapter 4, the aperture-coupled fed antenna design is discussed and optimized. The chapter presents the initial prototype, equivalent circuit, and input impedance of the antenna. Various optimisation techniques are explored, and the performance of the aperture-coupled antenna is compared to that of an edge-coupled antenna in terms of reflection coefficient, VSWR, and transmission coefficient. Chapter 5 studies the antenna array, analysing different microwave imaging scanners such as headband and helmet scanners. The chapter also covers the modelling of the head and blood target and compares the transmission levels between the headband and helmet scanners. Additionally, the chapter examines the performance of ECA and ACA arrays in imaging reconstruction using the DBIM-TwIST method. Chapter 6 investigates the experimental microwave imaging system, covering phantom preparation, calibration, and the use of a vector network analyser. The chapter presents experimental validation of the system and explores imaging reconstruction using experimental data to assess the system's effectiveness. Finally, Chapter 7 summarizes the key findings of the thesis and discusses potential avenues for further development in the field of microwave imaging systems, aiming to improve performance and broaden the range of applications.

Chapter 2 Background and Methodology

With the increasing prevalence of brain disorders and the limitations of conventional techniques in detecting these conditions at early stages, microwave brain imaging has become an active area of research in recent years. This growth is primarily due to the advantages and improved detection rates offered by microwave brain imaging. To achieve these outcomes, specifically designed antennas are needed to satisfy the requirements of such systems, where an antenna array is typically used. These antennas need to comply with several criteria, including bandwidth, size, design complexity, and manufacturing cost, to make them suitable for these applications.

Many studies in the literature have proposed antennas designed to meet these criteria, but no works have systematically classified and evaluated these antennas for use in microwave brain imaging [70]-[193]. This section presents a comprehensive study of the different antenna designs proposed for microwave brain imaging, with a thorough investigation of the antenna elements suggested for use in these systems. Antennas are classified by type and by improvements concerning operational bandwidth, size, radiation characteristics, and techniques used to achieve these enhancements.

The goal is to identify the most suitable antennas that can effectively address the unique challenges associated with microwave brain imaging applications. To achieve this, we first present a comprehensive study of the different antenna types, such as Vivaldi, coplanar waveguide (CPW), probe-fed patch, aperture-coupled patch, printed Yagi, dielectric resonator (DR), and wearable textile antennas. We then investigate the design and optimisation methods used to improve their performance in terms of operational bandwidth, size, radiation characteristics, and manufacturing cost. These methods include impedance matching techniques, advanced numerical analysis for scattering parameter evaluation, power transfer efficiency analysis, and regular-shaped formula estimation. Additionally, we explore various simulation software tools used to validate the antenna designs and optimisation processes.

By examining these design and optimisation methods, we aim to provide a qualitative evaluation of the antenna designs and compare their suitability for use in antenna arrays for microwave brain imaging. This evaluation will enable researchers and practitioners to make informed decisions when selecting the most appropriate antennas for their microwave brain imaging systems, based on each antenna's performance, design complexity, and manufacturing cost.

2.1 Biomedical Antennas for Microwave Imaging

2.1.1 Vivaldi Antenna

The Vivaldi antenna was first introduced by Gibson *et al.* over four decades ago in a coplanar configuration [89]. This designed Vivaldi antenna achieved a 10 dBi gain and a sidelobe level of -20 dB over a frequency range of 2.0 to 40.0 GHz. The Vivaldi antenna is also known as a tapered slot antenna due to its unique structure. In 1988, Vivaldi antenna is refined into an antipodal design to reduce beamwidth, sidelobes, back lobes, and return loss by Gazit [90]. Two flares are located on opposite sides of the substrate. This ultra-wideband antenna has garnered significant interest from researchers and has been explored for implementation in various microwave systems, including tomographic medical imaging, radar microwave imaging systems, astronomy and vehicular communication systems.

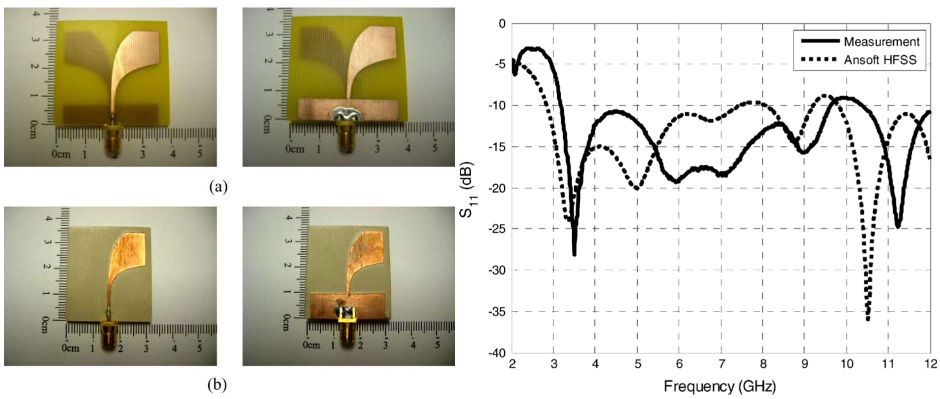

Figure 2.1 A compact Vivaldi antenna by Hood *et al.* [91].

The Compact Antipodal-Vivaldi Antennas exhibit a remarkable ability to generate highly directional radiation patterns, characterized by substantial gain and minimal reflection loss. Nevertheless, their operational frequency range is generally constrained to frequencies above 3.0 GHz. In [92], Mahdi *et al.* present an innovative antenna design featuring dimensions of 40.0 mm × 60.0 mm × 0.508 mm, rendering it suitably compact for integration into imaging systems. However, this antenna design remains most effective for frequencies exceeding 3.4 GHz. In another study[91], an antenna presented by Hoods *et al.*, features a physical size of 39.4 mm by 36.9 mm as shown in Fig. 2.1. However, it exhibits an operational frequency that is notably higher than the 3.1GHz.

Some Antipodal-Vivaldi antennas are improved to work in our desired frequency ranges, but the dimensions of them get quite large. [93] reports an Antipodal-Vivaldi antenna with operation frequency between 0.73 GHz and over 20.0 GHz, but its dimension is 151.0 mm by 140.0 mm, which is far above our desired dimension.

A Recent study by Biswas *et al.*. [94] presented a compact wideband antipodal Vivaldi antenna design inspired by the fern fractal leaf for microwave imaging applications. The proposed antenna was realized on a 0.8 mm FR4 substrate with a dimension of 50.8 mm × 62.0 mm and fed by an edge-fed microstrip line. The antenna showed excellent performance in terms of gain with a wide frequency range of 1.3 GHz to 20.0 GHz, making it suitable for microwave imaging systems. The use of the fern fractal leaf inspired design of the antenna provides a wider bandwidth than the previously reported antennas. Nonetheless, the end-fire radiation pattern contributes to the imaging system's lack of compactness, posing a challenge in terms of its miniaturisation potential.

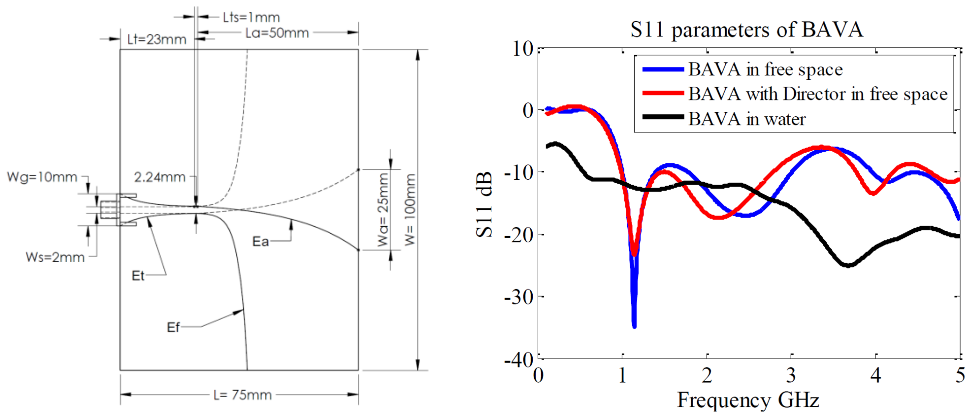

Figure 2.2 A large Vivaldi Antenna by Syed *et al*. [95].

Researchers investigated the antenna performance in coupling liquid. In the paper [95] by Syed *et al*., an Antipodal-Vivaldi antenna was utilised for microwave imaging applications. The antenna covers a frequency range of 0.5 GHz to 4.0 GHz and has dimensions of 100.0 mm by 75.0 mm, as illustrated in Fig. 2.2. This antenna design demonstrates potential for use in various microwave imaging scenarios due to its wide frequency coverage and operation within our desired frequency band.

In another study, Wang *et al*. proposed and experimentally validated a compact slot-loaded antipodal Vivaldi antenna for monitoring liver microwave thermal ablation using microwave imaging [96]. This antenna design aimed to optimize electromagnetic power transfer to the human abdomen by operating in a coupling medium, achieving a working bandwidth ranging from 600 MHz to 3.0 GHz. Notably, the final design's dimensions (40.0 mm × 65.0 mm) were the most compact among antennas designed for similar biomedical applications within the same bandwidth. The researchers developed a coupling medium using a low-cost and easily accessible mixture of water, oil, dishwashing detergent, and guar gum. This material exhibited dielectric properties close to the target values, maintained stability over a week, and displayed reproducibility across different realizations. The measured S-parameters of the antenna demonstrated good agreement with simulation results, and the antenna exhibited favourable performance regarding mutual coupling when two antennas were positioned in close proximity, as in the MWI array configuration. While the slot-loaded antipodal Vivaldi antenna design presented by Wang *et al.* offers promising features such as compact size and a wide operational bandwidth, the end-fire radiation pattern may pose a challenge for the overall size of the scanner. The end-fire pattern, which directs the main radiation lobe along the antenna's longitudinal axis, may require additional spacing between elements in the array configuration, potentially increasing the scanner's size. This factor must be considered when evaluating the suitability of the antipodal Vivaldi antenna for specific microwave imaging applications, as the size constraints may outweigh the benefits of the compact aperture dimensions and broad bandwidth.

Vivaldi antennas are known for their high gain, wideband, high front-to-back ratio, and high efficiency. However, they typically have a relatively large physical size, with dimensions often larger than 60.0 mm by 40.0 mm to operate within the frequency range of 0.5 GHz to 2.5 GHz. Additionally, the end-fire radiation pattern of the antenna often requires it to be positioned perpendicularly to the brain phantom, further increasing the overall size of the setup. The size limitations of Vivaldi antennas are main considerations for designing compact microwave imaging systems, particularly for portable and wearable medical diagnosis applications.

2.1.2 Microstrip Patch Antenna

Microstrip antennas, first conceived in the 1950s, have gained significant attention since the 1970s due to their low-profile, lightweight, low-cost, and easy integrability into arrays or microwave integrated circuits[97], [98]. These antennas consist of a metallic patch printed on a thin, grounded dielectric substrate, and can be fabricated using printed circuit techniques. They radiate a relatively broad beam broadside to the plane of the substrate, making them conformable and easily fabricated into linear or planar arrays. As a result, microstrip antennas have found a wide range of applications.

Despite their numerous advantages, microstrip antennas also exhibit some inherent limitations, including narrow bandwidth, spurious feed radiation, poor polarisation purity, limited power capacity, and tolerance problems[77], [81], [85]. As a result, much research and development have been focused on overcoming these drawbacks, leading to the development of dozens of variations in patch shape, feeding techniques, substrate configurations, and array geometries, as reviewed in [74], [74], [85], [99]–[101]. This extensive variety of designs highlights the versatility of microstrip antennas, which likely surpasses that of any other type of antenna element. Furthermore, the development of accurate and versatile analytical models has facilitated a better understanding of the inherent limitations of microstrip antennas and has contributed to their design and optimisation.

The most widely studied conventional microstrip antennas exhibit variations primarily in their feeding techniques. These distinctions significantly impact the performance and characteristics of microstrip antennas. In this section, we will explore two traditional microstrip antenna types used in microwave imaging, focusing on the probe-fed antenna and aperture-coupled antenna, as these are the most extensively studied and documented in the field. Although edge-fed microstrip antennas are the most straightforward and simple to implement, they are rarely utilized due to their narrowband nature. To overcome this limitation, the ground plane of edge-coupled antennas is often modified, transforming them into monopole antennas. As such, we will discuss them in the printed monopole antenna section. By examining the unique features and characteristics of these two types, we aim to provide a better understanding of their suitability and performance in microwave imaging applications.

A. Coaxial Probe Fed Patch Antenna

Probe-fed patch antennas have been extensively studied in recent years due to their low profile, ease of integration into arrays, and good radiation characteristics [102]–[110].

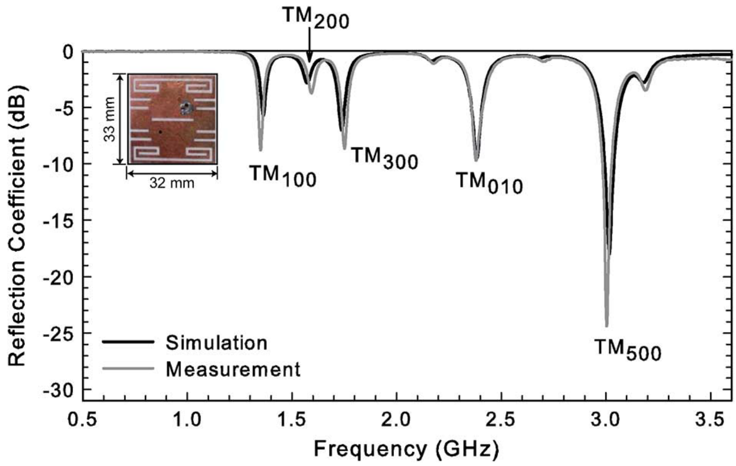

Figure 2.3 Dimension and return loss of a probe-fed patch antenna proposed by Aguilar *et al.* [105].

The miniaturisation of these antennas has been a focus of research. A study Aguilar *et al.* investigates the design, simulation, and testing of slot-loaded, multiband, miniaturised probe-fed patch antennas for microwave breast imaging applications [105]. They present a method that exploits the dominant longitudinal mode and one or more higher-order modes of the patch to achieve multiband responses, while using a combination of slots to achieve miniaturisation without compromising the structure's symmetry. The study demonstrates the successful fabrication and experimental verification of dual-, tri-, and quad-band miniaturised patch antennas in a biocompatible immersion medium, exhibiting excellent agreement between measured and simulated resonant frequencies. The simulation and measurement return loss of the proposed quad-band antenna with compact dimensions of 33.0 mm by 32.0 mm, is illustrated in Fig. 2.3. Furthermore, the investigation explores the trade-off between miniaturisation via slot-loading and gain, as well as the effect of substrate dielectric constant and thickness on the gain of miniaturised patch antennas. Additionally, they present a computational study that highlights the feasibility of utilising an enclosed array with two miniaturised patch antenna designs for 3D microwave breast imaging systems, suggesting their suitability as array elements in applications requiring unidirectional radiation, environmental shielding, and dense spatial sampling of scattered fields. The study's findings contribute valuable insights into the potential of miniaturised probe-fed patch antennas in the field of microwave breast imaging.

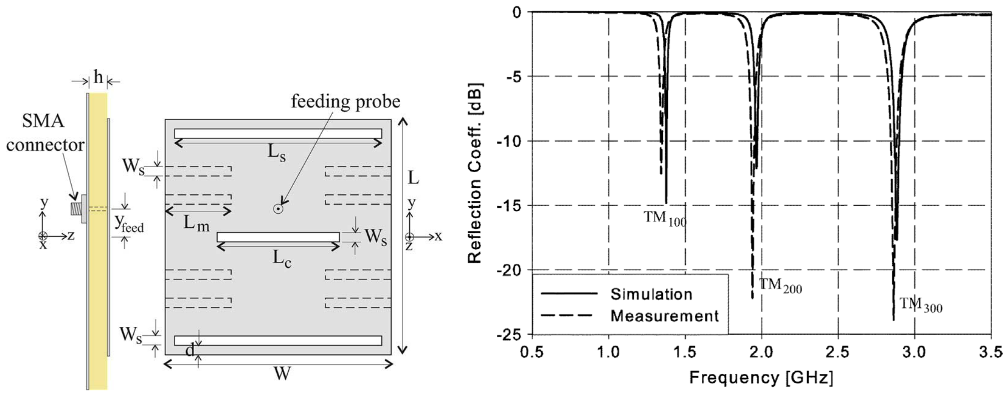

(a) (b)

Figure 2.4 Dual-band probe-fed antenna: (a) antenna dimension, L = 29.0 mm and W = 28.0 mm; (b) simulated and measured return loss [106].

In another recent study conducted by Al-Joumayly *et al.* [106], the design and characterization of a probe-fed patch antenna for biocompatible applications were investigated. The antenna features a dimension of 29.0 mm by 28.0 mm as shown in Fig. 2.4 (a), was specifically designed to operate in an immersion medium consisting of safflower oil, which is known for its biocompatibility. To ensure optimal performance, the dielectric properties of the safflower oil were carefully characterized within the frequency range of 0.5 to 3.0 GHz, which is of interest for the application. The researchers utilized an Agilent 85070D dielectric probe kit and an E8364 vector network analyser (VNA) to measure the frequency-dependent complex permittivity of the safflower oil.

Subsequently, they employed a single-pole Debye model to fit the obtained data, which allowed them to determine the Debye parameters essential for the preliminary antenna simulations. The dual-band response was obtained by exploiting the dominant mode and one higher-order mode of the patch antenna. Miniaturisation was achieved using a series of strategically placed slots, ensuring the structure's symmetry was maintained, resulting in similar and symmetric radiation patterns at both operational bands. They successfully fabricated and experimentally verified two prototypes in a biocompatible immersion medium, demonstrating the structure's suitability as an array element for multifrequency microwave breast imaging applications requiring high signal-to-noise ratios. This study contributes valuable insights into the design and development of probe-fed, dual-band, miniaturised patch antennas for biocompatible applications like microwave breast imaging. By thoroughly characterizing the dielectric properties of the immersion medium and employing a single-pole Debye model, the researchers achieved a strong correlation between simulation and measurement data for the antenna as suggested in Fig. 2.4 (b). The proposed miniaturisation technique, using strategically placed slots, maintained the structure's symmetry while achieving a dual-band response. The successful fabrication and experimental verification of the prototypes in a biocompatible medium highlight the antenna's potential as an array element for multifrequency microwave breast imaging applications that demand high signal-to-noise ratios.

Some studies have been conducted specifically for microwave brain imaging. Rokunuzzaman *et al.* presented a 3-D edge-fed antenna for human head-imaging applications[107]. The antenna utilized a stacked patch with a folding technique for miniaturisation and achieved a resonance frequency of 2.65-2.91 GHz with an average gain of 6.6 dBi at 2.7 GHz. The antenna had a compact size of 25.0 mm by 25.0 mm by 10.5 mm and high directivity throughout the operating frequency range. A shorting wall was used to lower the resonance frequency while maintaining high gain. The proposed unidirectional antenna had a peak front-to-back ratio of 19 dB, making it suitable for highly directive applications. The antenna was constructed using air substrate and a 0.2-mm-thick copper sheet, and successfully detected a tumour in a human brain phantom through raster scanning imaging method of a 2-D plane. While the antenna had a compact size and high directivity throughout the operating frequency range, its frequency is considered too high for brain stroke microwave imaging applications.

Miniaturising antenna often results in higher operation frequency. To minimise the antenna dimensions while maintaining the operational range within our desired frequency, researchers proposed antennas that are designated to operate in coupling liquid. Syed *et al.* presented a coaxial probe-fed slotted triangular patch antenna specifically designed for microwave tomography applications[108]. They introduced two antenna designs with dimensions of 51.0 mm × 40.0 mm and 29.0 mm × 28.0 mm, which incorporated slots to enhance impedance matching and minimize reflection coefficients. The study investigated the antenna's performance in free space and in the presence of a matching medium and imaging tank. The study also discussed the impact of substrate on antenna performance. The study showed that utilizing FR-4 as a substrate significantly expanded the antenna's -5 dB bandwidth, while dielectric loading contributed to lowering the resonant frequency within the desired range. Furthermore, optimising the slot angle and distance from the triangular patch's bottom edge resulted in improved antenna matching across the 1.0 – 3.5 GHz bandwidth. Notably, a second resonance around 3.0 GHz was achieved by selecting appropriate values for these two parameters. The fabricated prototype exhibited good agreement between simulation and measurement, with discrepancies attributed to fabrication tolerances. The compact version of the antenna demonstrated the deepest resonance with FR-4 substrate, whereas RT6002 provided the most broadband operations.

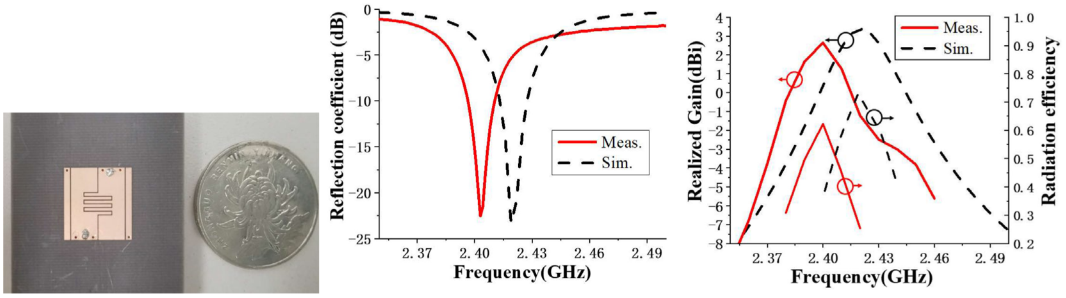

(a) (b) (c)

Figure 2.5 A differentially probe fed patch antenna: (a) Size of fabricated antenna; (b) return loss for simulation and measurement; (c) realised gain and radiation efficiency for both simulation and experiment [109].

Researchers also investigated differential feeding method for minimising the antenna dimension. In a recent work by Wang *et al.,* a novel miniaturised differentially fed patch antenna operating in half-mode using shorting pins on the patch edges is proposed [109]. The design features two shorted patches separated by a slot with an interdigital structure and is differentially fed by two probes close to the short-circuit edge. By applying the odd-even mode theory to investigate the capacitive slot's miniaturisation mechanism, the slow-wave effect of the interdigital structure further contributes to the antenna's size reduction. The resulting design showcases an electrical size of 43.5 mm by 30.0 mm, operating at 2.42 GHz, and achieves an impressive 90.6% size reduction compared to conventional square patch antennas. This fabricated S-band antenna is suitable for narrowband applications, demonstrating symmetrical radiation beams, low cross-polarisation levels, and narrowband characteristics. The simulated and measured 10 dB impedance bandwidths are 14.2 MHz (centred at 2.420 GHz) and

15.0 MHz (cantered at 2.402 GHz), respectively as illustrated in Fig. 2.5 (b). The simulated and measured peak gain values are 3.4 dBi and 2.7 dBi with an efficiency of 73.6% and 62.7%, respectively as shown in Fig. 2.5 (c). The good agreement between the simulated and measured results indicates the effectiveness of the design, with discrepancies primarily due to processing and experimental errors.

The probe fed patch antenna, featuring a small size, low profile, high radiation efficiency and narrow band, is well-suited for narrowband applications. However, these characteristics of presented antennas pose limitations for microwave imaging due to either a narrowband operation or functioning at frequencies beyond our desired range. Besides, the cross-polarisation issue of probe-fed antenna is proved more pronounced than edge-coupled and aperture-coupled antenna [111]. These limitations present a big challenge for microwave imaging applications, where a broader frequency band or a more suitable frequency range is required.

B. Aperture-coupled Fed Patch Antenna

The development of microstrip antenna technology witnessed rapid progress in the late 1970s, and by the early 1980s, fundamental microstrip antenna elements and arrays were well-established in terms of design and modelling [98], [112], [113]. Researchers began focusing on enhancing performance features like bandwidth and increasing the technology's applications, including its integration into phased array systems. The use of single-layer substrates presented several limitations, including insufficient space for antenna elements, active circuitry, bias lines, and RF feed lines, as well as reduced bandwidth due to high permittivity. Researchers explored multi-layered substrates, and in 1984, the idea of combining geometries using a slot or aperture to couple a microstrip feed line to a resonant microstrip patch antenna emerged [79]. This led to the development of the first aperture-coupled microstrip antenna, which showed promising results in terms of impedance matching and radiation patterns, with minimal back radiation from the coupling aperture.

Aperture-coupled microstrip antennas have since exhibited numerous advantageous features and developments, including demonstrated impedance bandwidths ranging from 5% to 50%, independent selection of antenna and feed substrate materials, and a two-layer construction that shields the radiating aperture from the feed network. This feeding method offers increased substrate space for antenna elements and feed lines, convenient integration for active arrays, theoretically zero cross-polarisation in principle planes, and a multitude of possible variations in patch shape, aperture shape, feed line type, and more. Furthermore, the technology has been extended to aperture-coupled microstrip line couplers, waveguide transitions, dielectric resonators, and other applications [78]–[80], [80], [112], [114]–[119].

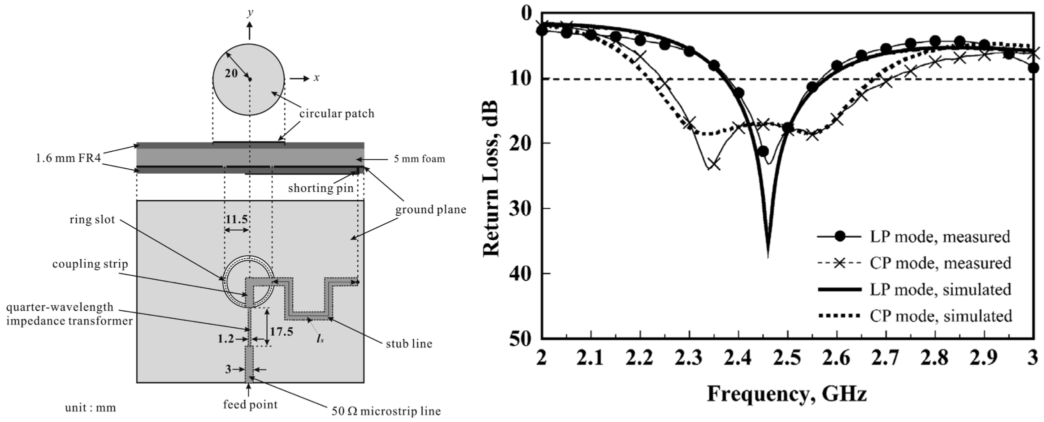

(a) (b)

Figure 2.6 An aperture coupled antenna with switchable polarisation: (a) Schematic structure; (b) return loss of both linear- and circular-polarised mode in simulation and experiment [120].

In a recent study by Row *et al,* ring-slot-coupled designs with switchable polarisation are presented and investigated [120]. The overall size of the proposed aperture-coupled antenna is 100.0 mm by 100.0 mm. By adjusting the stub length, the minimum axial ratio of the antenna can vary between 0.4 and 23.0 dB, enabling it to radiate either linear polarisation with high cross-polarisation levels or circular polarisation with a low axial ratio. The variation of the axial ratio against the stub length exhibits a periodic pattern. Moreover, good impedance matching is achievable for both linear and circular polarisation radiation. Two designs with polarisation switching between linear and circular are introduced, each requiring only one diode and a relatively simple DC-bias network compared to previously reported designs.

The proposed switchable polarisation microstrip antenna offers an operating bandwidth exceeding 4%, as determined by the CP 3 dB-axial-ratio bandwidth. Fig. 2.6(b) shows the linear mode operates within the frequency range of 2.4 GHz to 2.6 GHz, while the circular-polarized mode functions between 2.25 GHz and 2.65 GHz. This design demonstrates the versatility and adaptability of the antenna for various applications by providing both linear and circular-polarised operation modes within different frequency bands.

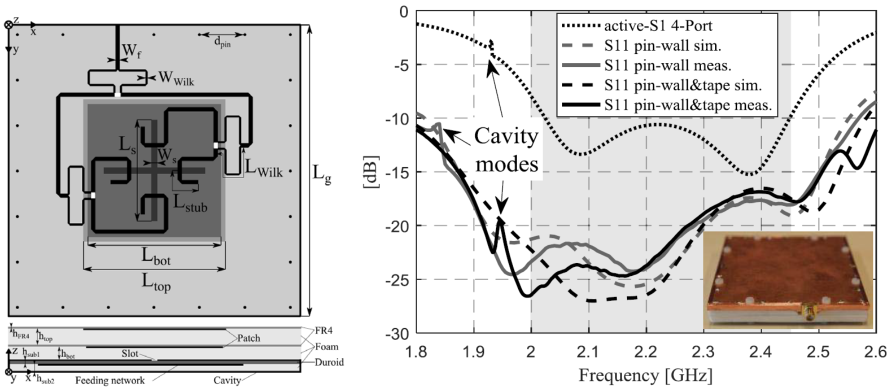

(a) (b)

Figure 2.7 A wideband aperture coupled fed antenna: (a) Antenna structure (b) return loss in simulation and experiment [114].

Another study presents an innovative design and measurement results for aperture-coupled fed wideband patch antennas, specifically tailored for nanosatellite applications [114]. These applications demand low-profile antennas, which often result in significant back radiation from the coupling aperture. The proposed design takes advantage of the resulting electric field distribution in the feeding strip line, boosting the electromagnetic coupling to the radiating element. This is achieved by enclosing the strip line feeding structure with vertical conductive walls, effectively creating a cavity. The proposed antenna dimension is 100.0 mm by 100.0 mm. The resulting antenna features a low profile of 0.08 λ_0 at 2.0 GHz and demonstrates 3 dB gain and axial ratio bandwidths of 27% and 32%, respectively. The proposed antenna operates within a wide frequency range, from below 1.8 GHz to 2.5 GHz as shown in Fig. 2.7 (b).

This study also offers an in-depth analysis of the cavity resonances and demonstrates how they can be used to reduce interference in adjacent frequency bands. Furthermore, it proposes an elegant method of integrating this type of antenna into the satellite chassis, minimising the antenna extrusion on the satellite surface. This literature review emphasises the significance of aperture-coupled fed wideband patch antennas in nanosatellite applications. Since these systems operate within similar frequency bands with microwave imaging, the antenna's wide operating range and favourable properties such as low profile, high gain, and broad axial ratio bandwidths make it a promising candidate for integration into microwave imaging applications.

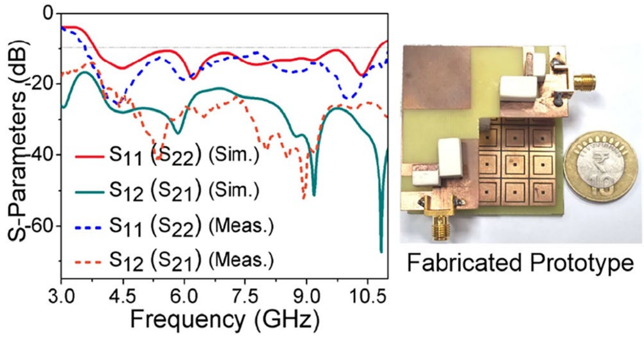

Figure 2.8 A compact aperture coupled fed resonator wideband antenna [121].

Another study combines the aperture coupled feeding method and dielectric resonator antenna. They presented an innovative aperture-coupled stepped dielectric resonator (DR) ultrawideband (UWB) multiple-input–multiple-output (MIMO) antenna (UMA) design, which features a compact size of 30.0 mm by 25.0 mm and operates within a wide frequency range of 3.8 GHz to 10.5 GHz [121]. This antenna design demonstrates a unique approach by employing a stepped DR that resonates with quasi $TE^{x}_{\delta 11}$ mode at 5.4 GHz and quasi $TE^{y}_{1\delta 1}$ TE mode at 6.4 GHz, merging with aperture resonating bands to achieve UWB performance. The proposed orthogonal MIMO configuration allows the stepped DR to improve isolation in the higher frequency region, while a modified neutralisation line via a quarter-wavelength square patch enhances isolation in the desired lower frequency region.

Furthermore, the broadside radiating modes of the stepped DR and the dual artificial magnetic conductor (AMC), and PEC bands of the AMC reflector contribute to improved gain and radiation characteristics. An enhancement of 37.84% in gain stability within 2.3 dB variation (i.e., 4.2 – 6.5 dB) is achieved, demonstrating the antenna's superior performance. The group delay of the UMA is more stable than that of the UWB antenna (UA), effectively addressing the issue of phase linearity associated with multipath effects. This literature review emphasizes the significance of aperture-coupled antennas in advancing UWB MIMO antenna designs, offering promising potential for various applications requiring compact, high-performance antennas with wide frequency coverage.

Numerous aperture-coupled antennas have been proposed and demonstrated to operate effectively within the frequency range commonly used for microwave imaging applications. However, the compact aperture-coupled antenna operates around 4.0 GHz, which is far beyond our desired frequency band. Others operating around 2.0 GHz are relatively large, typically around 100.0 mm by 100.0 mm, making them challenging to adapt for use in multi-antenna arrays for improved image reconstruction. Despite these challenges, aperture-coupled antennas exhibit desirable features such as low spurious radiation, directive radiation, and potential to operate within our desired frequency range. In this paper, we will demonstrate the design of this type of antenna in coupling liquid and explore its potential for application in multi-antenna arrays for microwave imaging systems.

2.1.3 Printed Monopole Antenna

The edge-fed printed monopole antennas, which offer a very large impedance bandwidth along with reasonably good radiation patterns in the azimuthal plane, have been extensively explored[70], [83], [122]–[129]. On the one hand, a printed monopole antenna can be viewed as a special case of a microstrip antenna configuration. In this case, a patch is fabricated on a dielectric substrate, commonly FR4, while the ground plane is shortened or modified. The area of the substrate without a ground plane backing can be considered as having air dielectric substrate $\varepsilon_r = 1$ with its thickness extremely thick, which increases the effective length L_{eff} of patch due to the fringing effect. An approximation for the effective length L_{eff} of a rectangular patch antenna can be expressed as follows[85]:

$$L_{eff} = L + \Delta L$$

$$\Delta L \approx 0.412 \frac{h(\varepsilon_{reff}+0.3)}{(\varepsilon_{reff}-0.258)} \frac{(\frac{w}{h}+0.264)}{(\frac{w}{h}+0.8)}$$

, where L is the actual length of patch, h is the substrate thickness, ε_{reff} is the effective dielectric constant, w the width of patch. As a result of the increased effective dielectric substrate, the effective length L_{eff} of the printed monopole antenna is increased. This leads to the printed monopole antenna exhibiting a broader bandwidth compared to a conventional microstrip antenna with an infinite ground plane.

Alternatively, printed monopole antennas can be seen as a vertical monopole antenna. A monopole antenna usually consists of a vertical cylindrical wire mounted over the ground plane, whose bandwidth increases with increase in its diameter. A printed monopole antenna can be equated to a cylindrical monopole antenna with large effective diameter. This second analogy has been used to determine the lower band-edge frequency of all regular shapes of printed monopole antennas for various feed configurations[124].

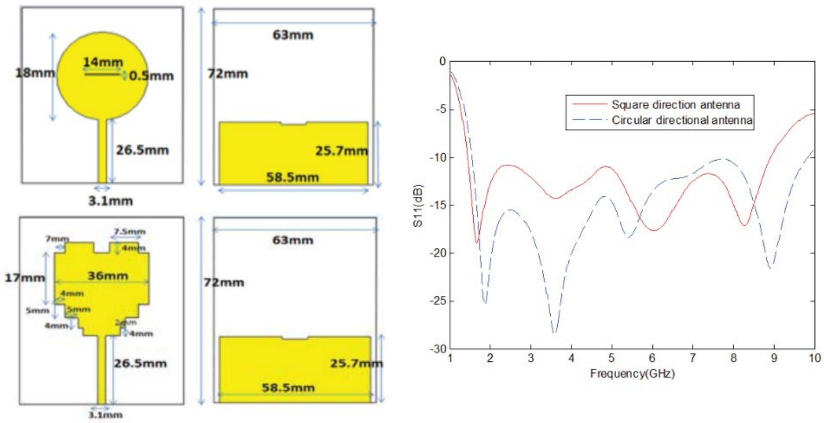

Figure 2.9 A printed monopole antenna designed by Sheela *et al.* [130].

Printed monopole antennas are widely investigated in microwave imaging area. In the study by Sheela *et al*. [130], the authors designed and fabricated directional printed monopole antennas as shown in Fig. 2.9 for microwave breast imaging applications. The antennas have a compact size of 73.0 mm by 62.0 mm and operate within the frequency range of 1.4 GHz to 10.0 GHz. Despite the compact size of the printed monopole antennas, there is still room for improvement in their performance. Sheela *et al.* suggest that by modifying the ground using DGS, the performance of printed monopole antennas can be further improved, which could result in better antenna efficiency, gain, and directivity. Additionally, the lower band edge frequency of printed monopole antennas could be lowered to extend their operating frequency range and make them more versatile.

Ojaroudi *et al.* proposed a novel compact edge-fed printed monopole antenna with multi resonance characteristics for use in circular cylindrical microwave imaging system applications [123]. The proposed antenna was designed with a rectangular slot and two horizontal T-shaped strips protruding inside the slot in the ground plane to enhance bandwidth. Additionally, two E-shaped slots with variable dimensions were used to excite additional resonances and achieve much wider impedance bandwidth, especially at the higher band. The fabricated antenna satisfied the 10-dB return loss requirement from 2.92 to 12.83 GHz and had a simple configuration with an ordinary square radiating patch and a small size of 12.0 mm by 18.0 mm. Although this proposed printed monopole antenna has a compact size, its working frequency range is optimal for microwave imaging scanning in brain stroke detection.

Syed presented an edge-fed printed monopole antenna design in [131] for microwave tomography applications. The antenna was fed by an edge-fed microstrip line with a length of 30.0 mm and a width of 24.0 mm. Its operation frequency ranges between 0.5 GHz and 2.5 GHz. The antenna exhibited good performance in terms of return loss and radiation patterns, and its compact size made it suitable for microwave tomography applications.

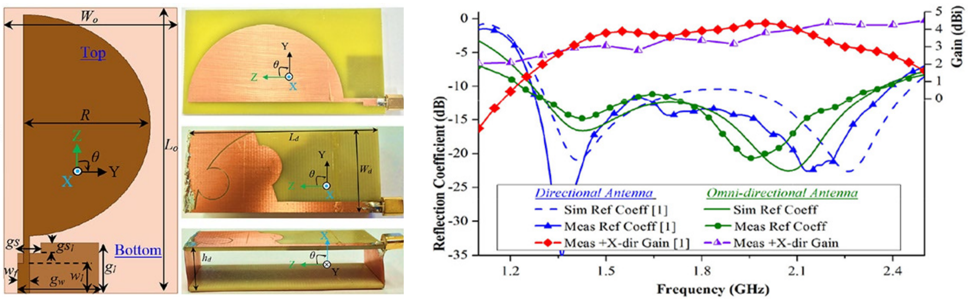

(a) (b)

Figure 2.10 A Wideband monopole antenna: (a) Schematic diagram of omnidirectional (semi-circular shaped patch) and directional antenna; (b) simulated and measured return loss[125].

In a recent study, Mobashsher *et al.* proposed both directional and omnidirectional wideband monopole antennas in [125]. They also investigated the influence of directionality on the image quality of microwave-based head imaging systems by designing and prototyping both directional and omnidirectional wideband antennas, with dimensions of 80.0 mm by 45.0 mm by 15.0 mm shown in Fig. 2.10 (a). Both antennas operate at a wide bandwidth from 1.25 to 2.4 GHz as illustrated in Fig. 2.10 (b), which is typically used in microwave head imaging, and achieve a boresight average gain of 3.5 dBi. Additionally, the near-field radiation patterns and transient pulse performance in the near-field region along the boresight direction are measured and analysed.

An experimental verification is conducted by imaging a realistic artificial head phantom with an emulated brain injury. The reconstructed images suggest that in the absence of multipath effects inside the head, the directional antenna offers 20% higher impulse fidelity and 4 dB more peak transient response compared to the omnidirectional antenna. The quantitative analysis of the reconstructed images demonstrates that the directional antenna produces more focused images with fewer artifacts than the omnidirectional antenna.

Several designs of printed monopole antennas have been proposed for use in medical imaging systems, each with its own advantages and limitations. While some proposed antennas operate at higher frequency bands, some have larger dimensions, others have lower gain and/or radiation efficiency. The wide working frequency band between 0.5 GHz – 2.5 GHz and compact size are major impairments that limit the dynamic range of the imaging system, which aims to detect weak backscatter from the target. Further research is required to address these limitations and optimise the design of printed monopole antennas for medical imaging applications, particularly for achieving high-performance characteristics such as wide bandwidth, high gain, and high radiation efficiency.

2.1.4 Coplanar Waveguide (CPW) Antenna

In the last few decades, significant progress has been made in the development of coplanar waveguide (CPW) antennas, which were first introduced by C. P. Wen in 1969 [132]. CPW antennas have gained prominence in microwave integrated circuits (MICs) and monolithic microwave integrated circuits (MMICs) due to their distinct advantages over conventional microstrip patch antennas. CPW antennas offer wider bandwidth, lower dispersion, and lower radiation loss, making them suitable for a range of microwave applications. Additionally, CPW antennas enable easy integration with active and passive components for impedance matching and gain improvement, as well as seamless incorporation with MMICs. The coplanar waveguide design, which positions all conducting elements on the same side of the dielectric substrate, overcomes the limitations of microstrip antennas by providing better accessibility to the ground planes and simplifying the connection process to other components. This unique configuration allows for improved performance, more compact designs, and greater flexibility in various microwave systems [132]–[144].

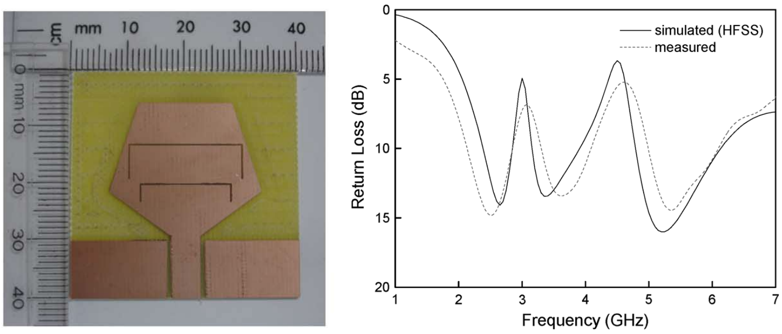

(a) (b)

Figure 2.11 A compact CPW antenna: (a) Fabricated antenna; (b) return loss in both simulation and measurement [135].

A compact CPW-fed planar monopole antenna with triple-band operation for WiMAX/WLAN applications has been developed, featuring a size of 40.0 mm by 40.0 mm by 0.8 mm [135]. The antenna consists of a pentagonal radiating patch with two bent slots printed on a 0.8 mm-thick FR4 substrate and is fed by a 50-ohm coplanar waveguide (CPW) transmission line. This design, compared to conventional CPW antennas, uses two bent slots to create dual stopbands. This tapered structure helps achieve a wider impedance bandwidth and good impedance matching across the operating bands. Figure 2.11 (b) illustrates the simulated and experimental return loss for the antenna as a function of frequency, showing a good agreement between the two. The antenna exhibits three distinct operating bands with 10 dB return loss at approximately 2.14 - 2.85 GHz, 3.29 - 4.08 GHz, and 5.02 - 6.09 GHz, corresponding to bandwidths of 28%, 21%, and 10%, respectively. For the lower operating band of 2.4 – 2.7 GHz, the antenna gains ranges from 1.77 to 2.15 dBi. In the medium operating band of 3.3-3.8 GHz, the antenna gain varies between 1.72 and 2.47 dBi. The gain of highest operating band, which spans from 5.15 to 5.85 GHz, ranges from 2.52 to 4.13 dBi. The antenna exhibits three distinct operating bands and stable gains, making it a versatile and efficient solution for WiMAX/WLAN applications.

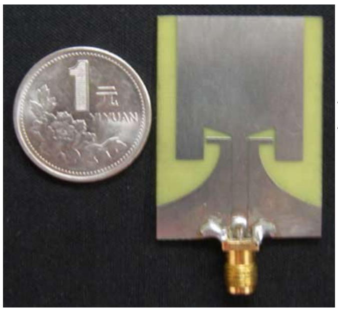

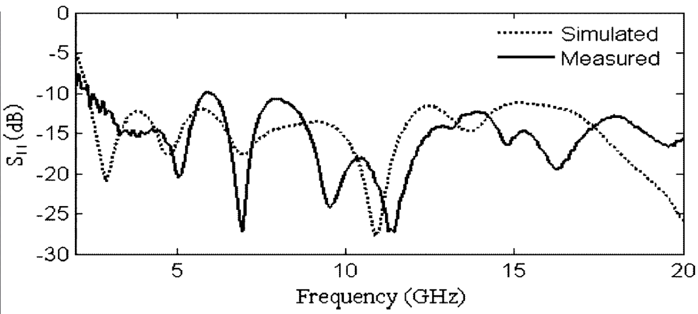

(a) (b)

Figure 2.12 A wideband CPW: (a) Structure of fabricated antenna; (b) return loss in both simulation and experiment [136].

Numerous studies have focused on exploring methods to expand the operational bandwidth of CPW. A wideband CPW-fed rectangular monopole antenna, with a compact size of 41.0 mm by 23.0 mm by 0.5 mm has been proposed and designed by Deng *et al.* [136]. The enhancement of the bandwidth is achieved through an M-shaped notch at the patch bottom, a tapered CPW ground outside the notch, and a T-shaped CPW ground inside the notch. This wideband antenna operates in the frequency range of 2.5 – 20.0 GHz, providing a versatile solution for various applications. Within its operation frequency band, the radiation efficiency of proposed antenna varies from 0.75 to 0.97 and the gain ranges from 0.7 to 4.4 dBi across the frequency band. Compared to conventional CPW antennas, this design offers a compact size and an exceptionally wide operational bandwidth, making it a standout example in the CPW antenna landscape.

To modify resonant frequency and operation band of a miniaturised dual-band CPW-fed annular slot antenna, Chiang *et al.* proposed an arc-shaped tuning stub[137]. By modifying the angle of the arc-shaped tuning stub, the first-higher order resonant mode can be shifted to the lower frequency band, combining with the fundamental mode of the annular slot to achieve a broadband operation with a bandwidth of 3048 MHz (78.4%). The miniaturised design features an embedded strip protruding from the ground plane into a slit, which reduces the centre frequencies of the two resonant bands by 60% and 44%, respectively. The prototype exhibits broadside radiation patterns with maximum peak antenna gains of 3.8 dBi and 5.1 dBi for the two resonant bands. The proposed CPW antennas showcase the potential for achieving broader bandwidth, shifted resonant frequency, and miniaturisation, making them a promising option for microwave imaging applications.

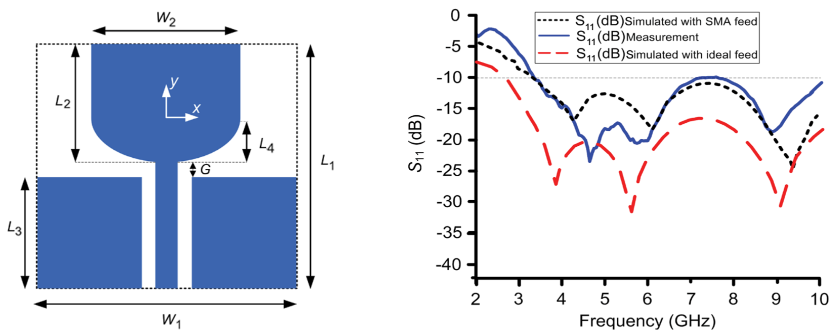

(a) (b)

Figure 2.13 A compact CPW operating in lossy coupling liquid: (a) Antenna structure; (b) return loss in simulation and experiment [145].

In another study, Jafari *et al.* proposed a compact ultrawideband (UWB) antenna for near-field imaging operating in coupling liquid for microwave imaging [145]. The overall dimension of the antenna is 30.0 mm by 26.0 mm. The characteristics of the antenna operating in this medium and in the proximity of the human are through simulations and through measurements. They verified experimentally that the proposed printed tapered-square antenna achieves good impedance match from 3.4 to 9.9 GHz while operating in the coupling medium. They also proved that antenna near-field pattern in a multilayer body model is stable over the operating frequency band.

Researchers have been extensively exploring the potential of CPW antennas, demonstrating their diverse capabilities and applications. Some CPW antennas feature a compact size, making them suitable for space-constrained applications, while others boast wideband performance, enabling them to cover a broader range of frequencies. Certain designs can operate effectively in coupling liquids, and some provide methods for manipulating the operation frequency, allowing for greater flexibility. However, it is worth noting that the typical operation frequency of CPW antennas is usually beyond 2 GHz, which may limit their applicability in microwave imaging applications. Nonetheless, the versatility of CPW-fed antennas continues to drive research and innovation in the field.

2.1.5 Printed Yagi Antenna

Conventional Yagi antennas typically offer narrow bandwidth (<10%). In addition, in the process of Yagi-Uda antenna miniaturisation, the gain would decrease, and the resonant frequency would deviate as well. To improve its performance, researchers have developed the quasi-Yagi antenna structure, which offers improved performance compared to traditional Yagi antennas, and proposed a compact printed Yagi antenna, which are known for their simple structure, ease of integration with microwave circuits, and high gain, making them ideal for wireless applications. The printed Yagi antennas typically consist of a dipole antenna acting as feed, which is called driven element. The directive elements are printed toward the end-fire direction to enhance the gain by directing electromagnetic energy in a specific direction.

Printed Yagi antennas offer several advantages in microwave imaging applications, such as their simple structure, lightweight design, high gain, and directionality, making them suitable for various wireless applications. They can be easily scaled to operate at different frequencies and provide focused electromagnetic energy in a specific direction, which enhances image clarity. However, they also have limitations including narrow bandwidth, lower gain for compact designs, complex optimisation processes, sensitivity to manufacturing tolerances, and limited polarisation diversity [146]. Although printed Yagi antennas have demonstrated their benefits in numerous wireless applications, overcoming these limitations and balancing the necessary trade-offs remains a challenge for optimal performance in microwave imaging.

Recent advancements in printed Yagi antennas include compact designs featuring modified bowtie driven dipoles, broad-band planar Quasi-Yagi antennas, dielectric resonator-based Yagi antennas, hybrid Moxon-Yagi composite antennas, etc. [147] – [151]. These designs present various trade-offs between bandwidth, gain, and size, with some offering exceptional fractional bandwidth but limited gain due to the utilisation of fewer directive elements.

Muhammad *et al.* presented a bandwidth enhancement approach for a printed Yagi bi-layer antenna operating at the S-band [146]. The antenna comprises ground planes, microstrip feedlines, driven elements, and directive elements on both top and bottom metalized layers. The bottom plane directive elements are offset towards the direction of propagation, aiming to maximize gain and bandwidth simultaneously. Elliptically shaped directive elements are introduced near the active dipole elements to achieve a broad bandwidth matched to 50 Ω input impedance. The proposed antenna design is analysed through full-wave electromagnetic simulations using CST Microwave Studio, and its performance is compared to a traditional Yagi antenna without the wide directive element. Operating in the frequency range of 2.6 - 4.3 GHz, the proposed antenna with dimension of 140.0 mm by 60.0 mm, has a fractional bandwidth of 49.3%. Additionally, it has an average gain of over 7 dBi and maximum side-lobe levels of less than -10 dB, making it suitable for broadband RF applications.

A recent study presents a compact and wideband planar Yagi antenna designed for improved performance without increasing the antenna's physical size [152]. The reflector is capacitively coupled to the driven bowtie to create a lower resonance at its patch mode, thus enabling a compact design. Moreover, the antenna employs series capacitive loading to the bowtie, and the reflector is folded at both ends toward the bowtie, further contributing to its miniaturisation. The antenna measures 120.0 mm by 100.0 mm and demonstrates a wide measured fractional bandwidth of 48% (0.69–1.12 GHz), with peak gain and front-to-back ratio (FBR) values of 5.5 dBi and 10 dB, respectively. This compact planar Yagi antenna showcases a successful approach to achieving wide bandwidth and desirable performance characteristics.

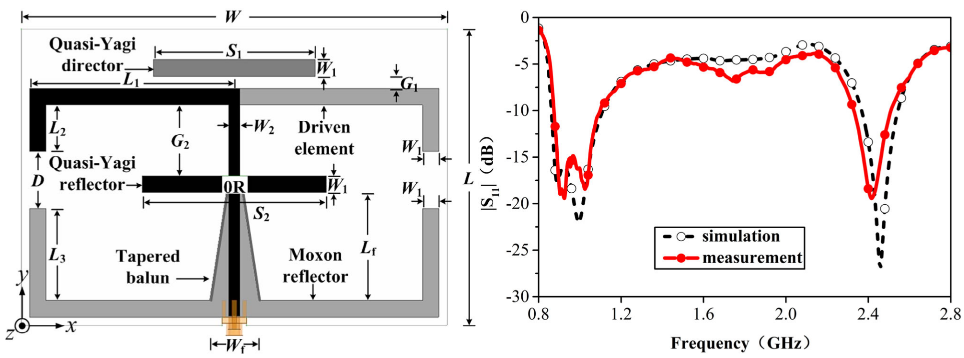

(a) (b)

Figure 2.14 A compact printed Yagi antenna (a) Antenna structure; (b) return loss in experiment and simulation [150].

Fu *et al.* proposed a compact printed Yagi antenna with dimension of 104.0 mm by 72.5 mm [150]. The innovative aspect of the proposed antenna lies in its combination of planar Moxon and quasi-Yagi interleaved structures. The Moxon structure's compact size enables it to operate in the lower band, while the quasi-Yagi structure, sharing the same area, is designed for the higher band. This design allows for independent adjustment of the lower and higher frequency bands. Simulation and experiment results in Fig. 2.14 demonstrate that the fabricated antenna has a moderate gain of over 5 dB and a large front-to-back ratio of more than 15 dB in both the frequency band between 902 and 928 MHz and 2.4-2.4835 GHz frequency band, with low cross-polarisation levels.

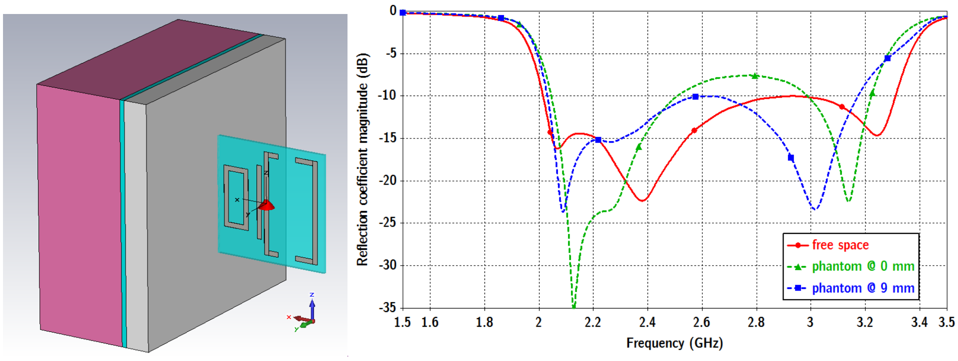

(a) (b)

Figure 2.15 A compact Yagi Antenna for microwave breast imaging: (a) The printed quasi-Yagi antenna radiating against a three-layer breast; (b) return loss [151].

More recently, Kakoyiannis *et al.* presents a compact printed quasi-Yagi antenna with dimension of 42.0 mm by 42.0 mm, specifically intended for microwave breast imaging applications[151]. Operating in the 2.0 – 3.3 GHz range, the antenna offers a 55% fractional bandwidth and a maximum gain of 5 dBi, demonstrating high efficiency. This antenna features a unidirectional driver-reflector pair and two closely spaced directors, which significantly enhance the operational bandwidth while maintaining a broadband front-to-back ratio (FBR) above 10 dB.

Yagi antennas provide several benefits for microwave imaging applications, including high gain, directionality, lightweight design, and scalability to different frequencies. These advantages allow for improved signal-to-noise ratio and image quality. However, they also face challenges such as narrow bandwidth, lower gain for compact designs, end-fire radiation pattern, and sensitivity to manufacturing tolerances.

2.1.6 Dielectric Resonator (DR) Antenna

Dielectric resonators (DRs) have been employed as high-Q elements in microwave filter and oscillator designs since the 1960s. Recently, DRs have gained significant attention for their potential in microwave applications[111], [147], [153]–[157]. DRAs offer more degrees of freedom to designers compared to 2-D-type antennas like microstrip antennas or 1-D-type antennas such as monopole antennas. They possess several advantages, such as a small size, lightweight, low cost, ease of excitation, and relatively wide bandwidth compared to microstrip antennas. DRAs can be excited using various feeding schemes, including coaxial probe, coupling slot, microstrip line, coplanar waveguide, conformal strip, dielectric image guide, or metallic waveguide.

Typically, DRAs are operated in either fundamental broadside or end fire mode, with the former achieved by exciting the DRA with a displaced probe or a slot and the latter by axially feeding the DRA with a coaxial probe. Resonance frequencies of cylindrical DRAs are generally determined using approximate models or numerical methods, which is given as:

$$f_0 = \frac{6.324}{\sqrt{\varepsilon_r + 2}}\left[0.27 + 0.36\left(\frac{D_c}{4h}\right) + 0.02\left(\frac{D_c}{4h}\right)^2\right], 0.4 \le \frac{D_c}{4h} \le 6$$

, where D_c and h are the diameter and height of cylindrical DRA. Wideband and dual-band antennas are extensively employed in modern wireless systems, and various techniques have been developed to design dual-mode and high-gain DRAs, often utilising higher-order modes, featuring simple structures that require a small area.

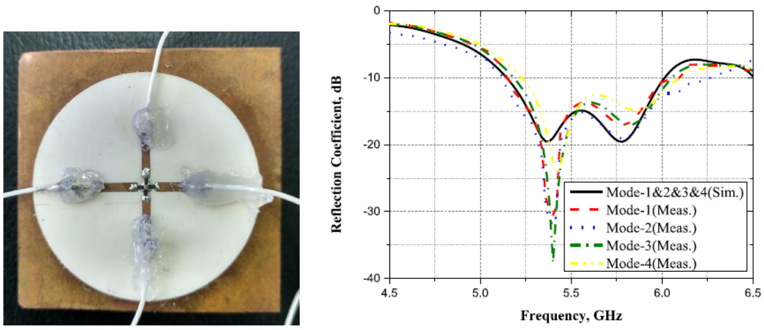

(a) (b)

Figure 2.16 A resonator antenna with parasitic elements (a) Fabricated DRA; (b) return loss in simulation and experiments [153].

Liu *et al.* proposed parasitic elements to modify antenna characteristics [153]. The proposed pattern-reconfigurable cylindrical dielectric resonator antenna comprises five elements: a probe excitation, a ground plane, a cylindrical DR, four ortho-symmetric parasitic elements, and four corresponding p - i - n diodes. Measuring 60.0 mm by 60.0 mm by 4.25 mm, this antenna design integrates four p - i - n diode switches and four parasitic elements, which enable the mode of the dielectric resonator to change when excited by the probe. As a result, the antenna's radiation patterns can focus energy in four specific directions, while minimising gain in other unwanted directions, without affecting the impedance bandwidth. The modified DRA cover a bandwidth of 870 MHz and achieve a high maximum gain of 9.74 dBi. A fully functional prototype has been designed, fabricated, and tested. The measured results for reflection coefficient, radiation patterns, and realized gain confirm the effectiveness of the proposed pattern-switching concept for cylindrical dielectric resonator antennas. Both simulations and experiments show that the antenna operates within the frequency range of 5.2 - 6.0 GHz as shown in Fig. 2.16(b).

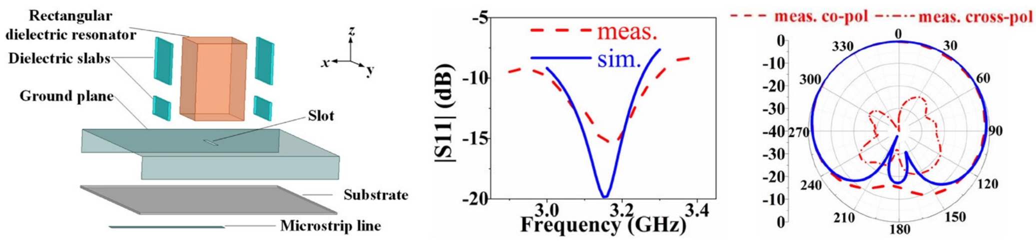

(a) (b) (c)

Figure 2.17 A rectangular DRA (a) Antenna structure; (b) return loss; (c)E-plane and H-plane radiation pattern [154].

Sun *et al.* applied two pairs of slabs symmetrically on the two opposite surfaces of rectangular DRA to obtain a wide-beam DRA [154]. The proposed rectangular dielectric resonator antenna (DRA) design has overall dimension of 80.0 mm by 80.0 mm by 30.0 mm. It incorporates two pairs of higher-permittivity dielectric slabs symmetrically attached to two opposite surfaces of the DRA in a direction parallel to the feeding slot. This configuration reduces radiation from these surfaces and achieves wide E-plane beamwidths. By adjusting the sizes or permittivity of the slabs, the beamwidths are tuned. They also fold down two sides of the metal ground plane in a direction perpendicular to the feeding slot to broaden the H-plane beamwidths. Measured results show that the maximum E-plane and H-plane half-power beamwidths (HPBWs) are 210° and 137°, respectively, with gains over 2.2 dBi throughout the usable bandwidth from 3.02 to 3.26 GHz (7.6%). Both measured and simulated reflection coefficients indicate a good level of agreement, with the lowest points at 3.15 GHz. The simulated impedance bandwidth is 7.6% (from 3.02 to 3.26 GHz), while the measured impedance bandwidth is 8.9% (from 3.01 to 3.29 GHz). The E-plane HPBWs of the proposed DRA range from 177° to 212° and H-plane HPBWs range from 120° to 146°.

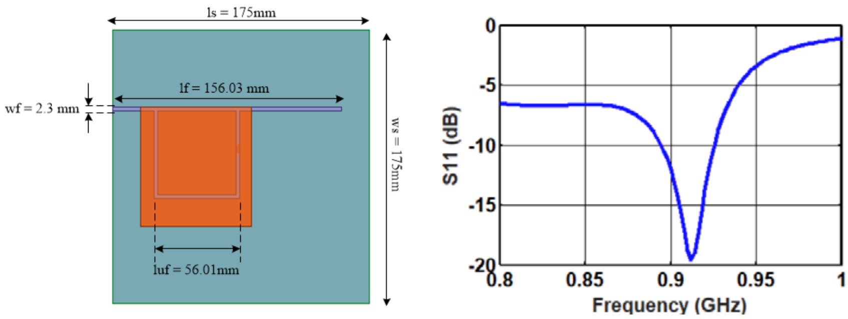

(a) (b)

Figure 2.18 A rectangular DRA operating at 0.93 GHz: (a) Antenna structure; (b) return loss in simulation [155].

Some researchers have been exploring and designing dielectric resonator antennas that operate around the 1 GHz frequency range, which is optimal for our microwave imaging application. One such example is a rectangular resonator with dimension of 76.007 mm width, 76.007 mm length, and 84.452 mm height [155]. This antenna is built on an RT 5880 Duroid substrate, featuring a dielectric constant of 2.2 and dimensions of 175.0 mm by 175.0 mm by 1.6 mm. Supported by a 0.035 mm thick copper ground plane, the antenna employs a microstrip feed complemented by an additional U-shaped structure for feeding. The antenna's performance, as demonstrated in Fig. (b), exhibits a reflection coefficient of less than -10 dB within a frequency range of 890 MHz to 930 MHz, translating to an impedance bandwidth of 40 MHz. Despite the larger dimensions, the dielectric resonator antenna demonstrates potential for use in the desired frequency range around 1 GHz.

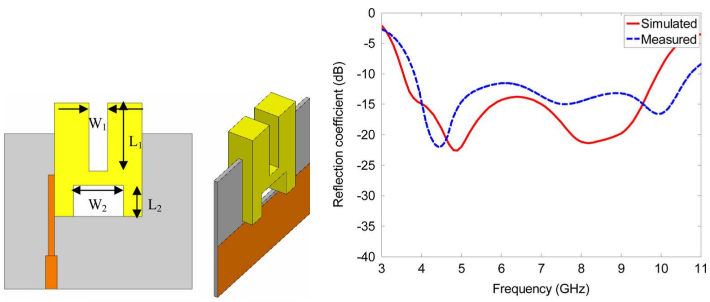

(a) (b)

Figure 2.19 A compact DRA for breast tumour detection: (a) Antenna structure; (b) return loss in simulation and experiment [156].

In a recent study, a DRA specially designated for near-field breast tumour detection has been reported in [156]. The proposed H-shaped ultrawideband (UWB) dielectric resonator is mounted on a vertical ground plane edge and features broadside radiation patterns. The DRA measures 14.0 mm in width, 18.3 mm in length, and 5.08 mm in thickness, with a dielectric constant of 10.2. It is supported by a 30 by 25 mm RT6002 substrate with a dielectric constant of 2.94 and a thickness of 0.762 mm. A partially printed ground plane, measuring 11.0 mm by 30.0 mm, is located under the DRA. With an operational bandwidth ranging from 4.0 GHz to 10.0 GHz, the DR sensor is designed to attach directly to the skin without the need for a matching medium, scanning the entire breast. The wide half-power beamwidth reduces path loss, while the DR sensor's pulse-preserving performance ensures low distortion, constant gain characteristics, and high efficiency. The sensor's small footprint allows for additional sensors to be placed nearby or in contact with the breast skin. The compact DR sensor's suitability for breast tumour detection is demonstrated through frequency domain analyses and time domain analyses, which show accurate tumour response due to its compact size and excellent sensor characteristics.

2.1.7 Wearable Textile Patch Antenna

In recent years, wearable textile patch antennas have attracted considerable attention due to their distinctive attributes [158]–[168]. Diverging from other antenna types, wearable textile patch antennas utilize textile materials as substrates. The lightweight and compact nature of these materials is essential for wearable applications, offering unique advantages over traditional antenna designs. Moreover, their low-cost and adaptable nature allow for seamless integration into various applications, such as wireless communication systems, environmental sensing, and health monitoring.

The development of wearable textile patch antennas presents unique challenges, including the need for conformal designs and low-profile arrangements, as well as addressing the impact of body-worn deployment on performance. Researchers have explored a range of materials and fabrication techniques, including Silicone-rubber [159], Fleece [163], Felt [160], Jeans [161] etc., to overcome these challenges while maintaining minimal degradation in near-body operation. Additionally, studies have examined the effects of Specific Absorption Rate (SAR) and bending schemes on wearable antenna performance [161], [164], [166], [167]. This critical area of research is instrumental in unlocking the full potential of wearable antennas for a diverse array of applications, further highlighting the significance of these investigations in academic and practical contexts.

In a recent study [158], Lin *et al.* present the design of a novel low-profile ultrawideband textile antenna specifically tailored for wearable microwave medical imaging systems with dimension of 80.0 mm by 40.0 mm. The proposed antenna utilizes a monopole structure with two triangles and multiple parallel slots cut into the radiation patch, achieving an optimized ultrawide bandwidth and reduced antenna size. Polyester fabrics and conductive copper taffeta, readily available on the market, were chosen as materials to construct the antenna, ensuring its suitability for wearable applications that require flexible components conforming to human body curves. The measured results demonstrated that the fabricated antenna prototype could achieve a bandwidth of 109% from 1.198 to 4.055 GHz, with a realized gain of 2.9 dBi. Additionally, on-phantom measurements revealed that the antenna's operating bandwidth and realized gain remained relatively unaffected when in close proximity to human bodies. The antenna's applicability for microwave medical imaging was demonstrated by monitoring the recovery process of a bone fracture emulated by a body-mimicking phantom with a size-varying blood strip, showing significant variation in the time-domain reflection coefficient depending on the fracture size.

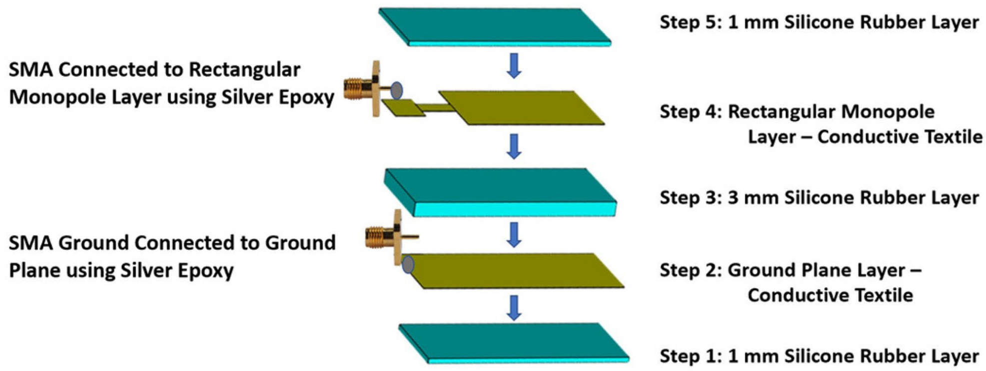

Figure 2.20 Structure of hybrid silicone textile wearable antenna [159].

Saied *et al.* present antenna design based on a rectangular planar monopole antenna structure [159], as shown in Fig. 2.6. The sensor's conducting material is made from a 0.1-mm-thick flexible conductive textile, Shieldex Zell, with a surface resistance of less than 0.02 Ω. The sensor's substrate comprises Shore A8 silicone rubber, chosen for its flexibility and stretchability without compromising structural integrity. The silicone rubber has a relative permittivity (ε_r) of 2.99, a loss tangent (tan δ) of 0.032, a tensile strength of 218 psi, and a tear resistance of up to 20 ppi. The fabrication process involved creating a silicone rubber mould and layering the ground plane, rectangular monopole patch, and additional silicone rubber layers. The final dimension of fabricated antenna is 78.88 mm by 43.26 mm. The designed antenna achieved a dual resonant frequency, with one band ranging from 600 to 800 MHz and the other from 1.8 to 2.09 GHz. Experimental results demonstrated the antenna's capability to successfully capture and differentiate between brain atrophy and lateral ventricle enlargement, both of which are pathological effects commonly associated with neurodegenerative diseases.

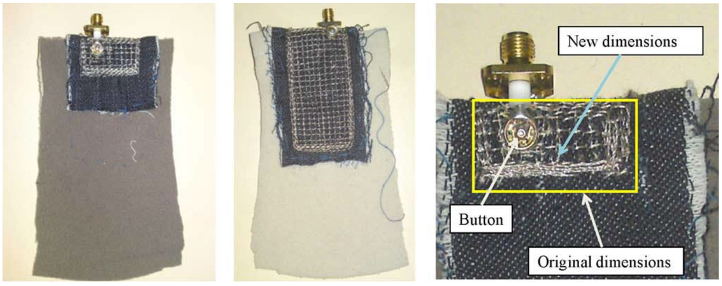

Figure 2.21 Full-textile PIFA: Top view of the original patch (left), bottom view of the ground (middle), and top view of the modified patch (right) [163].

Ivsic *et al.* investigate Planar Inverted-F Antennas (PIFAs) made of woven conductive textiles and of patterns embroidered with conductive threads for body-centric communication systems [163]. The antenna features a rectangular copper patch, copper ground and a fleece substrate as shown in Fig. 2.7. Dimension of modified antenna is 70.0 mm by 32.0 mm. The study focuses on the influence of conductive thread density and the effect of lockstitch on the antenna's resonant frequency. They also propose a metallic button as a transition between textile antennas and classical circuits, ultimately leading to the design of a wearable textile antenna. The measured return loss for the proposed full-textile antenna on the phantom demonstrates that the operation band ranges from 2.1 GHz to 2.6 GHz, with the antenna resonating at 2.25 GHz.

Scarpello *et al.* present a washable wearable inset-fed microstrip patch antenna [168]. Developed on a CO/PES nonconductive textile substrate, the study compares the performance of two different conductive materials: Flectron, a copper-plated nylon fabric, and Electrodag, a conductive ink printed via a screen-printing technique. The antenna's performance, including reflection coefficient and radiation efficiency, was assessed before and after applying a protective thermoplastic polyurethane (TPU) coating and after undergoing one, three, and six washing cycles. Results indicate that using conductive ink as the conductive layer provides a more stable resonance frequency, better matching, and more consistent radiation efficiency as the number of washing cycles increases compared to electro textile-based antennas. The proposed antenna has dimensions of 48.5 mm by 42.5 mm, designed for applications within the 2.3 GHz to 2.5 GHz operational band and resonating at 2.4 GHz. This study demonstrates the feasibility of designing wearable and washable antennas with conductive ink on a textile substrate for various applications, maintaining stable performance despite moderate moisture regain and multiple washing cycles.

Wearable textile antennas offer several advantages in terms of flexibility, comfort, and cost-effectiveness. These antennas are designed using flexible textiles, allowing seamless integration into clothing while conforming to the wearer's body shape, resulting in a more comfortable and unobtrusive user experience. In addition, they are lightweight, compact, and robust, making them ideal for wearers who require minimal interference with their daily activities, while also being cost-effective due to their use of conductive fabric materials. Despite their low gain and efficiency, these antennas are advantageous because they can function effectively in close proximity to the human body.

Nonetheless, incorporating textile antennas into wearable applications poses significant challenges. Firstly, printing RF circuits directly onto textiles presents difficulties due to the roughness of fabrics, making it costly to print multiple layers of conductive ink, and limiting the use of screen-printable interface layers to relatively homogeneous fabrics. Secondly, the miniaturisation of mm-scale sensors requires extensive power reduction techniques and faces challenges in energy storage and data communication due to the limited energy storage density of charge accumulation components and reduced system size. Thirdly, the integration of off-the-shelf components onto soft, flexible, and breathable fabric substrates presents challenges in reliably attaching components directly to the textile, with flexible filament circuits being a practical solution. Fourthly, the unpredictable outcomes of field and power distributions over a wide variety of body and tissue types call for comprehensive multi-physics models of tissues, organs, and bodies that match anatomic and molecular details to address RF issues such as power attention, interference, noises, and body artifacts. Finally, while efforts to tackle integration, manufacturing, and sustainability challenges continue, the long-term reliability of RF and microwave components in wearable applications remains uncertain, with dynamic mechanical and environmental stresses imposing a time-dependent decay on component reliability.

Different types of antennas have their advantages and disadvantages, and their performance can be compared based on specific requirements. In this case, we need a compact antenna measuring around 30mm by 30mm and operating between 0.5GHz-1.5GHz for microwave imaging applications. We reviewed literature on various antenna types and created a table to showcase their potential for this application.

Table 2.1 Comparative analysis of potential antennas for microwave imaging system

Antenna Type	Ref No.	Dimension in mm	Frequency in GHz	Background	Pros	Cons
Vivaldi	[91]	36.9 × 39.4	3.1 – 10.6	Free space	1. Wideband 2. Directional radiation 3. Low sidelobe levels 4. Adaptability for array 5. Good gain performance	1. Relatively large size 2. Complex structure 3. End-fire radiation
	[96]	65.0 × 40.0	0.6 - 3.0	Sunflower oil, distilled water, guar gum, dishwashing detergent		
	[94]	62.0 × 50.8	1.3 – 20.0	Free space		
	[95]	100.0 × 75.0	0.5 - 4.0	Water		
Probe fed Microstrip	[109]	43.5 × 30.0	2.42	Free space	1. Small size and low profile 2. High radiation efficiency 3. Well-suited for narrowband applications 4. Simple and easy fabrication 5. Good mechanical stability	1. Limited bandwidth (narrowband operation) 2. Operates beyond desired frequency range 3. Pronounced cross-polarisation 4. Not ideal for broader frequency band operation
	[105]	33.0 × 32.0	2.4; 3.0	Free space		
	[106]	29.0 × 28.0	1.3; 1.9; 2.8	Safflower oil		
	[107]	25.0 × 25.0	2.65 - 2.91	Direct coupling between antenna and tissue		
	[108]	29.0 × 28.0	2.5	Glycerine with water		
		51.0 × 40.0	1.3			
Aperture-coupled fed Microstrip	[120]	100.0 × 100.0	Linear polarised 2.4 – 2.6	Free space	1. Low spurious radiation 2. Directive radiation	1. Relatively large size 2. Design complexity
			Circular polarised 2.25 – 2.65			

	[114]	100.0 × 100.0	1.8 - 2.5	Free space	3. Increased substrate space for antenna elements and feed lines 4. Theoretically zero cross-polarisation	3. Hard fabrication process
	[121]	30.0 × 25.0	3.8 – 10.5	Free space		
Printed Monopole	[130]	72.0 × 63.0	1.4 – 10.0	Free space	1. Light weight and compact 2. Low cost and easy fabrication 3. Wideband 4. Easy integration with another circuitry	1. Limited gain and efficiency 2. Omni-directional 3. Spurious radiation
	[123]	18.0 × 12.0	2.92 – 18.30	Free space		
	[131]	30.0 × 24.0	0.5 – 2.5	Glycerine with water		
Coplanar waveguide	[135]	40.0 × 40.0	2.14 – 2.85 3.29 – 4.08 5.02 – 6.09	Free space	1. Compact size 2. Wideband performance 3. Versatility in various applications 4. Frequency manipulation 5. Low radiation loss	1. Increased dispersion 2. Sensitivity to manufacturing 3. Typical operation frequency beyond 2 GHz
	[136]	41.0 × 23.0	2.5 – 20.0	Free space		
	[137]	70.0 × 70.0	2.5 – 5.2	Free space		
	[145]	30.0 × 26.0	3.4 – 9.9	Free space		
Printed Yagi	[146]	140.0 × 60.0	2.6 – 4.3	Free space	1. High gain 2. Directional pattern 3. Light weight 4. Scalability for various frequencies	1. Large dimension 2. lower gain for compact design 3. End-fire radiation
	[152]	120.0 × 100.0	0.69 – 1.12	Free space		
	[150]	104.0 × 72.5	0.90 - 0.93 2.40 - 2.48	Free space		
	[151]	42.0 × 42.0	2.0 – 3.3	Free space/ Direct coupling		
Dielectric Resonator	[153]	60.0 × 60.0 × 4.25	5.2 – 6.0	Free space	1. Enhancement technology for antenna 2. Simple structure 3. 3D design	1. Hard to fabricate in lab
	[154]	80.0 × 80.0 × 30.0	3.0 – 3.3	Free space		
	[155]	175.0 × 175.0 × 84.5	0.89 – 0.93	Free space		
	[156]	30.0 × 25.0 × 5.0	4.0 – 10.0	Free space		
Wearable textile	[158]	80.0 × 40.0	1.2 - 4.1	Direct coupling	1. Flexibility 2. Capable of direct coupling in wearable application	1. Unstable performance 2. Miniaturisation challenges 3. Long-term reliability
	[159]	78.9 × 43.3	0.6 – 0.8 1.8 – 2.1	Direct coupling		
	[163]	70.0 × 32.0	2.1 – 2.6	Direct coupling		
	[168]	48.5 × 42.5	2.3 – 2.5	Direct coupling		

2.2 Antenna Design Techniques and Optimisation Methodology

2.2.1 Equivalent Circuit Models of Monopole Antennas

Since the earliest work in the 1950s, there have been a variety of analytical methods on the research of microstrip antennas (MSA). The analytical methods for MSA used in general can be divided into two categories: the rigorous full-wave technology and the approximation method [85], [126], [169]–[171]. The full-wave solution is an effective and accurate technology for solving the complex modular form of MSA. However, the computation of this method is complex and will acquire more time. Additionally, it does not consider the inner relationship between frequency response and physical structure. On the other hand, the equivalent circuit method is one of the approximation methods, and it is relatively simple and fast. Adopting this technique, the MSA can be modelled to the equivalent capacitances and inductances in series or parallel connections. The frequency characteristics can be predicted according to the concept of the LC resonant circuit. In a lossy antenna system where the inductance, capacitance, radiation resistance and loss resistance are distributed along the antenna structure, an equivalent circuit effectively captures the characteristics of the system. Designing a precise equivalent circuit for the antennas and figuring out the value of each distributed element are difficult tasks because there are just a few measurable factors (scattering matrix and antenna efficiency). We approximated the antenna loss in the original antenna array using a lumped resistor at each antenna port (connected in series or parallel).

As shown in Figure 2.6, the patch element can be seen as a parallel connection of a capacitor and an inductor, and the array of aperture elements is represented by a series LC circuit, where the conducting element provides the inductance and the inter-element spacing represents the capacitance. From this simple analysis, it is easy to show that the resonant frequency is given by $f = \frac{1}{2\pi\sqrt{LC}}$. The fractional bandwidth is defined as the difference between the lower and upper frequencies at -10 dB, which is proportional to $BW \propto \sqrt{\frac{L}{C}}$.

Thus, increasing the length of the conducting element can reduce the resonant frequency and improve the bandwidth. A lower resonant frequency can also be achieved by increasing the capacitance; however, this results in narrower bandwidth.

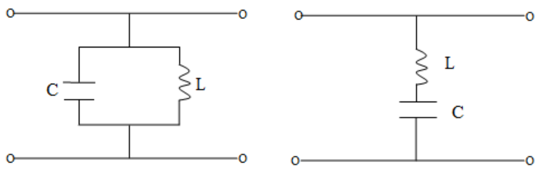

Patch element MSA Aperture element MSA

Figure 2.22 Equivalent circuit models of typical MSAs

2.2.2 Impedance Matching Method

The signal generator presents a generator impedance, which is $Z_g = R_g + jX_g$, where Z_g is the antenna impedance, R_g is the antenna resistance and X_g is the antenna reactance. The power delivered to the antenna for radiation P_r is:

$$P_r = \frac{1}{2}|I_g|^2 R_r = \frac{{V_g}^2}{2}\left[\frac{R_r}{\left(R_r + R_L + R_g\right)^2 + \left(X_A + X_g\right)^2}\right]$$

, where I_g is the current developed in the loop, R_r is the resistance of radiation, V_g is the peak generator voltage, R_L is the loss resistance of the antenna and X_A is the antenna reactance. The maximum power delivered to the antenna when the conjugate impedance of the generator matches the conjugate antenna impedance, i.e., $R_r + R_L = R_g$ and $X_g = -X_A$. For our imaging system, the conjugate impedance of the generator is 50 + 0j. Therefore, the antenna efficiency is maximised when the real part of antenna impedance is 50 Ohms and imaginary part of antenna impedance is 0.

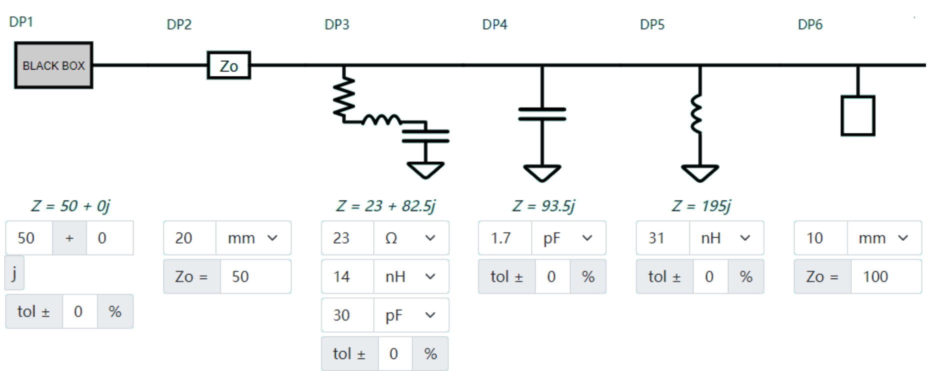

(a)

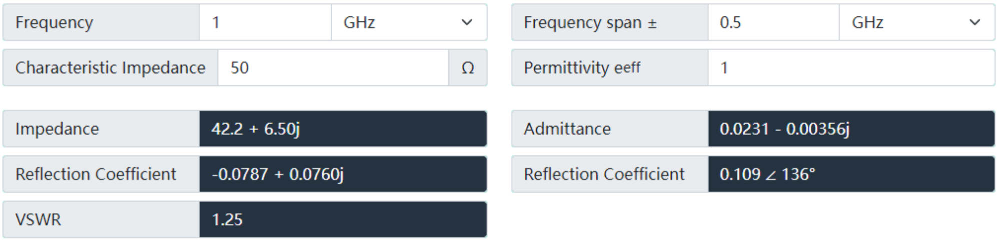

(b)

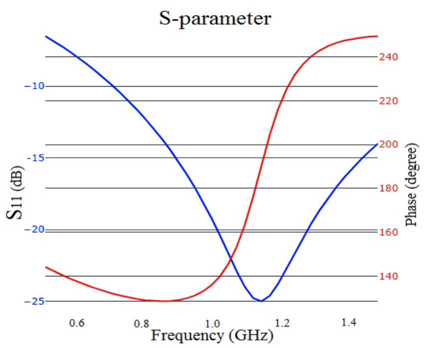

(c)

Figure 2.23 Equivalent circuit model of typical patch antennas: (a) Circuit illustration; (b) parameters in the circuit; (c) S_{11} of the circuit.

The resistance, which is the real part of input impedance on the Smith chart, comprises loss resistance $\mathrm{R_L}$ and radiation resistance $\mathrm{R_r}$. The power consumed by loss resistance is converted to heat, representing a waste of transmitter power. These heat-producing loss resistances comprise feedline loss resistance $\mathrm{R_{Lf}}$, patch loss resistance $\mathrm{R_{Lp}}$, ground strip loss resistance $\mathrm{R_{Lgs}}$, ground plane loss resistance $\mathrm{R_{Lgp}}$ and is given as

$$\mathrm{R_L} = \mathrm{R_{Lf}} + \mathrm{R_{Lp}} + \mathrm{R_{Lgs}} + \mathrm{R_{Lgp}}.$$

The power consumed by radiation resistance is converted to radio waves, the desired function of the antenna. The radiation resistance $\mathrm{R_r}$ is a joint effort of all radiating components. Similar to loss resistance, radiation resistance can be expressed as:

$$\mathrm{R_r} = \mathrm{R_{rf}} + \mathrm{R_{rp}} + \mathrm{R_{rgs}} + \mathrm{R_{rgp}} = \mathrm{R} - \mathrm{R_L}.$$

One of the main methods we applied to assess and thus optimise the antenna full-wave electromagnetic simulation software. We used Keysight Advanced Design System (ADS) to calculate the impedance and the equivalent circuit. For example, the equivalent circuit of a typical monopole antenna is illustrated with the ADS in Fig. 2.7 (a). The generator impedance was initialised as 50 + 0j. With the tool, the impedance of equivalent circuit at 1Ghz was calculated as 42.2 + 6.5j and the impedance at resonant frequency was calculated as 44.8 – 0.95, as shown in Fig. 2.7 (b). The magnitude and phase of s_{11} in the frequency band between 0.5 GHz and 1.5 GHz are plotted in Fig. 2.7 (c).

Previous research has investigated formulas for calculating the input impedance (Z_{in}) of microstrip patch antennas, providing a numerical method to determine the impedance based on the antenna's dimensions [99], [100], [127], [172]. The input impedance of the microstrip patch antenna is given by:

$$Z_{in} = \frac{Z_0}{2\pi\sqrt{\varepsilon_{eff}}} \tan^{-1}\left(\frac{h}{\varepsilon_{eff} W}\right)$$

,where the effective dielectric constant is $\varepsilon_{eff} = \frac{\varepsilon_r+1}{2} + \frac{\varepsilon_r-1}{2\sqrt{1+\frac{12\ h}{W}}}$, effective length is $L_{eff} = \frac{c}{2\ f_{resonant}\sqrt{\varepsilon_{eff}}}$, width of the patch is $W = \frac{c}{2\ f_{resonant}\sqrt{\varepsilon_{eff}+1}}$ and the actual length of the patch is $L = L_{eff} - 2\Delta L$. The ΔL, which occurs at the edges of the patch due to the electric field, is typically calculated using the formula: $\Delta L \approx \frac{(0.3h)(\varepsilon_r+0.3)}{(\varepsilon_r-0.258)(\frac{W}{h}+0.263)}$. Given the dimensions of the antenna and the resonant frequency, we calculated the impedance at the resonant frequency. By applying these formulas, we determined the characteristics of the microstrip patch antenna at the desired resonant frequency. This allowed us to design and optimise the antenna for specific applications and performance requirements, ensuring efficient and effective operation within the desired frequency range.

An important aspect of antenna design is achieving impedance matching, which is the process of adjusting the antenna's input impedance to match the characteristic impedance of the transmission line (typically 50 ohms). By realising conjugate matching, the total antenna efficiency is maximised, thereby improving antenna performance at a specific frequency. Conjugate matching minimises the reflection of power back to the source, thereby maximising the power transfer between the transmission line and the antenna.

2.2.3 Numerical Analysis of Scattering Parameter

We introduced the two-port network model and scattering parameter formulas as a guidance to design our antenna[85]. For a two-port network, the relation $b_1 = s_{11}a_1 + s_{12}a_2$ can be derived as: $\mathrm{s}_{11} + \mathrm{s}_{12} = \frac{\mathrm{V}_1 - \mathrm{Z}_1^* \mathrm{I}_1}{\mathrm{z}_1 \mathrm{I}_1 + \mathrm{V}_1}$. The sum of s_{11} and s_{12} realises a maximum value of 1 when z_1 is infinitesimal or V_1 is infinitely high.

The derived equation revealed the relation among input impedance, generator voltage and scattering parameters; thus, we modified the parameters of the equation to control the performance of the antenna. Since our purpose was to achieve a high s_{12} value, at least higher than -90 dB while keeping s_{11} below -10 dB in our desired frequency range, we increased the overall magnitude of both the s_{11} and s_{12} scattering parameters. Then we increased s_{12} and decreased s_{11} to achieve higher transmission efficiency.

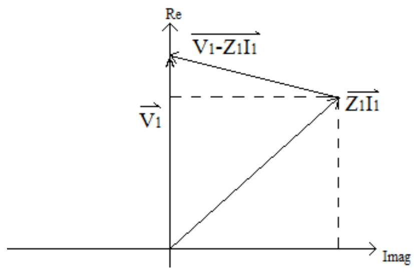

Figure 2.24 Numerator vector $(\mathrm{V}_1 - \mathrm{Z}_1^* \mathrm{I}_1)$ illustration.

We could increase the sum of $s_{11} + s_{12}$. We first maximised the sum of s_{11} and s_{12} to upgrade the magnitude scale of the sum to a higher level. First, increasing the value of V_1 to much greater than $z_1 I_1$ could maximise the sum. The safety of human tissue restricted us from increasing V_1 because high voltage is practically unsafe. According to IEEE, the SAR exposure limit has been set at 1.6 W/kg for any 1 g of tissue. In addition, the output level of VNA is fixed at 5 V, so V_1 cannot be modified. Therefore, increasing V_1 was not practically feasible. Second, we could modify the sum by changing the antenna impedance. The higher imaginary part of the conjugate antenna impedance was to be better to increase the numerator $(V_1 - Z_1^* I_1)$. With reference to Fig 2.24, the higher value of $(V_1 - Z_1^* I_1)$ was obtained while the real part retained at 50 ohms and the imaginary part was increased.

On the other hand, we could increase s_{12} and reduce s_{11}. As discussed in the conjugate matching method, the s_{11} reaches its minimum when the generator impedance matches the antenna impedance, i.e., the real part equals to 50 ohms and the imaginary part equals 0. However, we noticed that the sum of s_{11} and s_{12} decreases with the increase in the imaginary part of $Z_1^* I_1$; thus, reducing the imaginary part to 0 leads to the minimum value of the numerator $(V_1 - Z_1^* I_1)$. As a result, the overall magnitude scale drops dramatically. Therefore, the imaginary part could not be set as completely 0. Instead, we needed to make a trade-off between matching the imaginary part of impedance and obtaining a higher magnitude scale of $s_{11} + s_{12}$.

2.2.4 Power Transfer Efficiency Analysis

Power transfer (PT) analysis is studied to acquiring higher magnitude for s_{12}/s_{21}. As we know, s_{21} is defined as voltage gain, i.e., $s_{21} = \frac{V_{receiver}}{V_{transmitter}}$, while the power transfer efficiency (PTE) is defined as the power gain:

$$\eta = \frac{P_{receiver}}{P_{transmitter}} = \frac{\frac{{V_{receiver}}^2}{Z_{receiver}}}{\frac{{V_{transmitter}}^2}{Z_{transmitter}}}.$$

As we used the same antenna for transmitter port and receiver port, η was proportional to $(\frac{V_{receiver}}{V_{transmitter}})^2$, thus η was proportional to ${s_{21}}^2$. Therefore, we could modify the power transfer efficiency to optimise the magnitude of s_{21}.

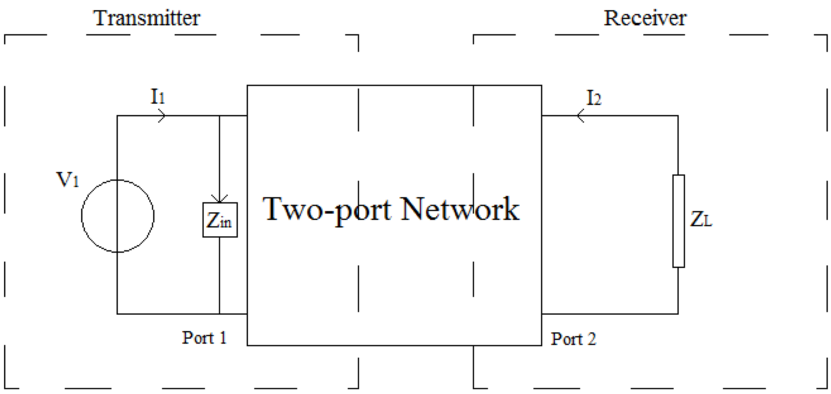

Figure 2.25 Generalised equivalent circuit of a two-port network.

With reference to Fig. 2.10, we referred to a reciprocal two-port network (i.e., $z_{12} = z_{21}$), represented by its impedance matrix, with elements $z_{ij} = z_{ij} + j\,x_{ij}$, with $i, j = 1, 2$ given as $V_1 = z_{11}I_1 + z_{12}I_2$, $V_2 = z_{12}I_1 + z_{22}I_2$ realising a power transfer module. The active input power P_{in} was delivered from the generator to the two-port network and received at z_L. We denoted the P_L as the active power on the antenna. The power transfer efficiency was denoted by $\eta = P_L / P_{in}$. This is the definition of efficiency commonly used in power systems. PT technology has been widely developed due to its advantages in many emerging applications. Many researchers have published their derived equation of maximum PTE [173]–[177]. Sampath et al. proposed that the maximum PTE η can be derived as follows:

$$\eta = 1 - \frac{2}{1 + \sqrt{1 + \left(\frac{x_{12}^2 + r_{12}^2}{r_{11}r_{22} - r_{12}^2}\right)}}$$

It can be concluded that the real part of transmitter r_{11} and real part of receiver r_{22} should be as small as possible for getting a high η. As a result, conjugate matching between generator impendence and antenna impedance can be difficult to achieve with minimal r_{11} and r_{22}. Therefore, we decreased the value of r_{11} and r_{22} on a small scale.

2.2.5 Regular-shaped Formula Estimation Formulas

Previous research conducted by Ray in [122] proved that the lower band edge frequency (f_L) could be calculated for a regular-shaped patch printed monopole antenna. In Ray's study, a standard formula in the following could be utilised for lower band-edge frequency estimation (1):

$$f_L = \frac{c}{\lambda} = \frac{7.2}{\{(L+r+p)\times k\}} \text{GHz}$$

$$r = \frac{S}{2\pi}$$

where p denotes the length of feedline in cm, L is the vertical length of patch, k is an empirical factor, decided by the permittivity of substrate and coupling liquid in which the antenna is immersed, and r is the effective radius of the patch, which is related to the area of printed patch S and can be calculated through the above formula.

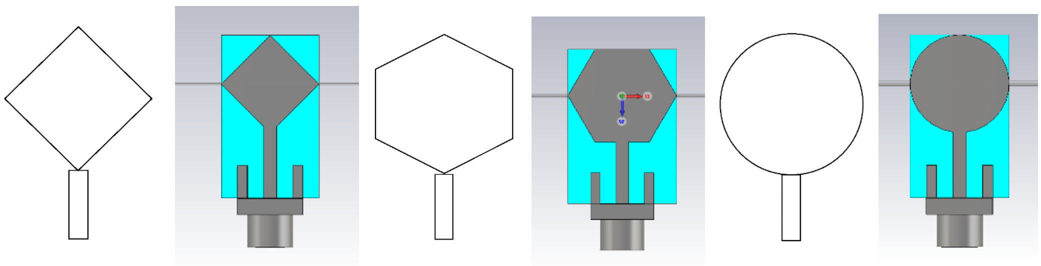

(a) (b) (c)

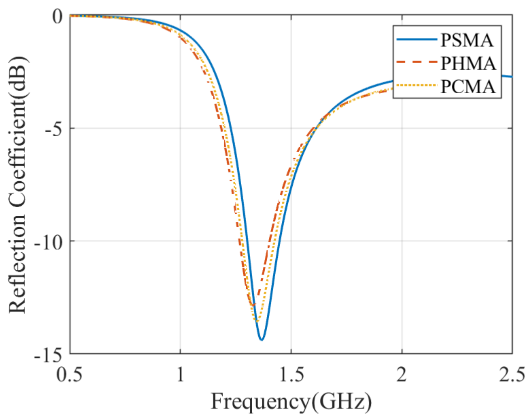

(d)

Figure 2.26 Geometry of regular shaped monopole antennas: (a) A printed square monopole antenna (PSMA), (b) a printed hexagonal monopole antenna (PHMA), (c) a printed circular monopole antenna (PCMA), (d) reflection coefficients for three kinds of monopole antenna.

The square, hexagonal and circular patches are three representative shapes among various kinds of regular-shaped patches. In this paper, we presented these shapes to validate Ray's standard formula so that we could apply this method to our design. We compared f_L in simulation with f_L in calculation for these three regular shaped printed monopole antennas. Fig.2.26 (a) (b) and (c) show the geometry and image in the simulation for the printed square monopole antenna (PSMA), the printed hexagonal monopole antenna (PHMA) and the printed circular monopole antenna (PCMA), respectively. A regular shaped patch made of perfect electrical conductor (PEC) with a thickness of 0.035 mm and a feedline made of PEC with width of 4 mm, and a thickness of 0.035mm were printed on a 50.0 mm × 30.0 mm × 2.0 mm FR4 substrate with a relative permittivity of 4.3 and tan δ of 0.025. A 50 Ω coaxial transmission line was used to feed the antenna. The antenna was placed in free space and the empirical factor was 1.0498.

For PSMA with a side length of a, L =$\sqrt{2}a$ = 30 mm, r = a/$(2\sqrt{2}\pi)$, the estimated lower band-edge frequency is 1.309GHz. The simulation result in CST shows that the lower band-edge frequency is 1.302GHz, which is consistent with the estimation result. For PCMA with radius of R, L = 2R = 30 mm, r = R/4 and the calculated lower band-edge frequency is 1.276 GHz. Its simulation result shows that the lower band-edge frequency is 1.280 GHz. For PHMA with a side length H, L =$\sqrt{3}$H = 30 mm, r = 3H/(4π) and its estimated lower band-edge frequency is 1.267 GHz. The simulation result in Fig. 2.26 (d) shows that the lower band-edge frequency equals 1.267 GHz. Through comparison between the calculation and simulation results, the error rate of the estimation equation was controlled within 1%.

The performance of the antenna could be adjusted by changing the dimensions of different elements in the antenna according to this formula. This formula was taken as an important criterion for antenna optimisation.

2.2.6 Simulation Software Validation

The Computer Simulation Technology (CST) Microwave Studio Suite is a widely used full wave electromagnetic simulation program in the field of antenna design and simulation. CST utilises the finite integration technique (FIT), which is the integral form of the Maxwell equations, as its primary technique. To solve the equations, the structure must be divided into small frequency or time domain cells. CST offers two fundamental solver modules, the time domain solver and the frequency domain solver.

The time domain solver is generally used for non-resonant structures, while the frequency domain solver is suitable for highly resonant structures. Additionally, a tetrahedral mesh can be used with the frequency domain solver; the frequency domain solver can better discretise 3D surfaces in comparison to the time domain solver, which cannot use a tetrahedral mesh. Moreover, frequency domain solvers can be employed for off-normal occurrences, while time domain solvers are appropriate only for normal incidence. Thus, in this project, a frequency domain solver was used for both the single antenna and the 8-antenna array.

The number of cells required for simulation depends on the complexity of the structure and the simulation. For example, for an antenna in a homogeneous glycerine-water mixture background, 200k tetrahedral cells are meshed with the frequency domain solver, while 3000k hexahedral cells are meshed with the time domain solver. For the 8-antenna array in a cylindrical glycerine-water mixture tank, 800k tetrahedral cells are meshed with the frequency domain solver, while 8000k hexahedral cells are meshed with the time domain solver. The number of cells required for simulation affects the simulation’s processing time and memory requirements.

During the simulations, the computation time of both solvers was recorded. For the single antenna case, it took 15 minutes to simulate with the frequency domain solver, while it only took 5 minutes to obtain the simulation results with the time-domain solver. For the 8-antenna array case, it took 8 hours to complete the simulation with the frequency solver, while the time domain solver took 2 hours to solve the simulation results. The processing speed of the simulation software is dependent on the CPU and GPU used. The better the CPU and GPU, the quicker the simulation will run. Additionally, the memory requirements for the simulation software depend on the size and complexity of the simulation. Generally, the more cells are required, the more memory is needed.

After obtaining the simulation results, we adjusted the antenna design in accordance with the CST results and the comparable circuit theory. The amplitude and phase angle of the input impedance at the required frequency range were displayed on the Smith chart of the input impedance in CST. By analysing the Smith chart, we determined the size of resistance and reactance, which are the actual and fictitious components of impedance. Impedance matching occurs when the input impedance and generator impedance are matched at the proposed frequency. This occurs when the input impedance resistance is equal to the generator resistance of 50 ohms and the input impedance reactance is 0, indicating that the magnitude of inductive reactance and capacitive reactance are equal. Maximum power is provided from the power generator to the antenna when the impedances are matched. Therefore, we could change the resistance to 50 ohms while also lowering the amplitude of reactance to 0 to optimise the antenna at a given frequency. Properly optimised antennas can result in improved performance and better signal reception.

Chapter 3 Printed Monopole Patch Antenna Design

In previous study, the prototype antenna featured a ground plane that extended across the entire substrate, a characteristic typical of microstrip patch antennas. Through optimisation efforts, it was discovered that reducing the ground plane to cover only a portion of the substrate yielded several benefits. These included minimising the antenna's dimensions, broadening the frequency bandwidth, and lowering the resonant frequency to below 1.5 GHz, a most desirable frequency range for brain stroke detection applications. However, this modification also altered the radiation pattern to an omnidirectional profile, rendering the antenna more akin to a printed monopole antenna than a traditional microstrip patch antenna. Due to its design and omnidirectional characteristics, the optimised antenna is commonly referred to as a printed monopole antenna, as itits has similar performance is more similar to that of a monopole antenna than that of a traditional microstrip patch antenna [83], [124], [127], [128]. Throughout this paper, we design and study the printed monopole antenna (PMA) with a partial ground plane, which operates in a coupling liquid comprising 90% glycerine and 10% water at our desirable frequency band between 0.5 GHz and 1.5 GHz.

3.1 Edge-coupled Antenna Design

Among the antennas developed for microwave imaging, printed monopole is the mostly discussed due to ease of fabrication, low profile and excellent performance, especially in microwave brain imaging. In addition, motivated by Ray's regular shaped monopole antenna and inspired by Bright Yeboah-Akowuah *et al.*.'s printed antenna in [83], [108], [124], we designed the spear-shaped patch edge-coupled antenna(ECA) shown in Fig.3.1 (a). The dimension of main body was 16.00 mm × 25.00 mm × 1.67mm, consisting of three parts: rectangulr ground plane covering the partial substrate behind the substrate, printed patch in front of substrate and substrate in the middle. A PEC spear-shaped patch with a thickness of 0.035 mm was printed on the front side of the FR4 substrate with a relative permittivity of 4.3 and tan δ of 0.025 with a thickness of 1.6mm. Its spear shape was formed by the exponential equation y=1.7×$e^{(x/1.7)}$+t and its transformation. X ranged from -4 to 2.4 to obtain curve A and another 3 curves were obtained through the mirroring and transforming of curve A. A 16.00 mm × 8.90 mm × 0.035 mm retanguar ground was designed on the back the substrate.

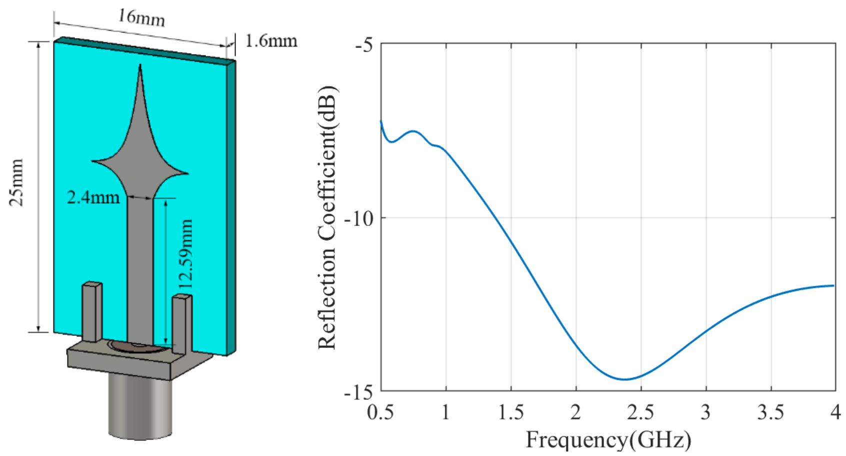

(a) (b)

Figure 3.1 Initial prototype of proposed antenna: (a) Antenna geometry; (b) reflection coefficient.

The S_{11} parameter for this spear-shaped patch antenna in the frequency range from 0.5 GHz to 2.5 GHz is plotted as shown in Fig. 3.1 (b) for assessing the performance of the antenna. The antenna was immersed in a mixture of 90% glycerine and 10% water. The lower band-edge frequency was 1.3394 GHz and the bandwidth of operation was 1.0853 GHz. The reflection coefficient resonated at 1.85GHz, with a value of -16.5dB.

3.2 Impact of Patch Shape on Antenna Performance

3.2.1 Reflection Coefficient

Ray's formula predicts that the lower band-edge frequency of a printend monopole antenna is negatively correlated to patch size; the area of a spear-shaped patch is comparatively smaller than other patch shapes. To decrease the dimension of the patch, we optimised the spear shape. The optimised antenna dimensions are shown in Fig. 3.2 (a).

To validate Ray's formula, we plotted the reflection coefficient of the optimised spear-shaped patch shown in Fig. 3.2 (b). The lower band-edge frequency decreased to

1.22 GHz, which agreed with Ray's monopole antenna formula. The operation frequency bandwidth was greatly widened.

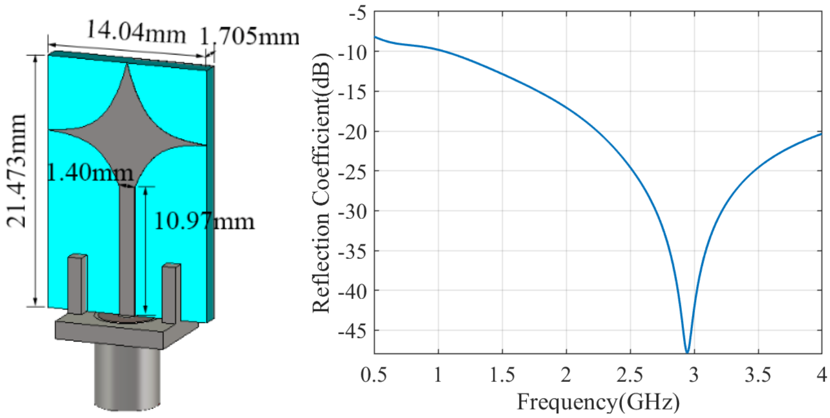

(a) (b)

Figure 3.2 Prototype of proposed antenna with optimised patch shape: (a) Antenna geometry with optimised patch shape; (b) reflection coefficient in the frequency range between 0.5 GHz and 4.0 GHz.

The reflection coefficients of some regular-shaped patch antennas between 0.5 GHz and 4.0 GHz are depicted in Fig. 3.3. Compared with the circular, square and rectangular-shaped antenna, the spear-shaped antenna shows deeper resonance and lower starting frequency, indicating a better impedance match and improved antenna efficiency.

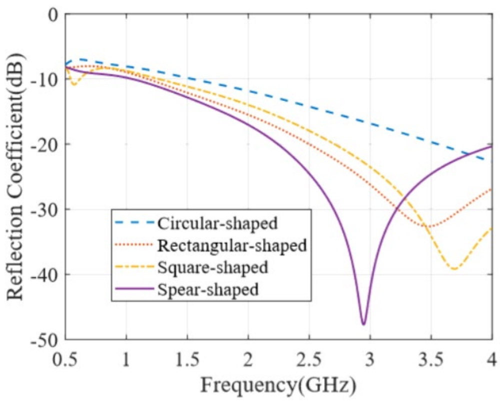

Figure 3.3 Reflection Coefficients of Regular-shaped Patch Antennas.

3.2.2 Radiation Resistance and Radiation Efficiency

In our study, we chose a spear-shaped patch for the microstrip antenna design, as opposed to utilising antennas with more conventional patch shapes. The rationale behind this spear-shaped patch is the improved radiation efficiency it offers, which is evidenced by its increased radiation resistance R_r. In this section, we compare the radiation resistance and radiation efficiency between spear-shaped patch and other-shaped patches by plotting surface the current distribution of antennas with different patch shapes.

As detailed in Section 2.2.2, radiation resistance R_r can be expressed as $R_r = R_{rf} + R_{rp} + R_{rgs} + R_{rgp} = R - R_L$. Consider that the radiated power P_r is given by the following equation:

$$P_r = \frac{1}{2}|I_g|^2 R_r = \frac{{V_g}^2}{2}\left[\frac{R_r}{\left(R_r + R_L + R_g\right)^2 + \left(X_A + X_g\right)^2}\right]$$

To find the value of R_r that maximises P_r, we first calculate the critical point by taking the partial derivative of P_r with respect to R_r:

$$\frac{dP_r}{dR_r} = \frac{{V_g}^2}{2[\left(R_r + R_L + R_g\right)^2 + \left(X_A + X_g\right)^2]} - \frac{{V_g}^2(R_r + R_L + R_g)}{[\left(R_r + R_L + R_g\right)^2 + \left(X_A + X_g\right)^2]^2}$$

Next, we can set the partial derivative equal to 0 and solve for R_r to obtain the critical point; we get:

$$0 = \frac{{V_g}^2}{2[\left(R_r + R_L + R_g\right)^2 + \left(X_A + X_g\right)^2]} - \frac{{V_g}^2(R_r + R_L + R_g)}{[\left(R_r + R_L + R_g\right)^2 + \left(X_A + X_g\right)^2]^2}$$

In the ideal case, where the impedance is perfectly matched, both the generator resistance (R_g) and the load resistance (R_L) should be equal to the characteristic impedance of the system. For a 50-ohm input impedance, R_g and R_L should ideally be 50 ohms each, and X_A and X_g should be close to 0 ohms. Under this assumption, we get the following:

$$0 = (R_r + 100)^2 - 2R_r(R_r + 100)$$

We find that the critical point occurs at R_r = 100ohms. To verify that this critical point corresponds to a maximum, we can consider the second derivative of the equation with respect to R_r. The second derivative is $\frac{d^2P_r}{d{R_r}^2} = -4$. Since the second derivative is negative, it indicates that the critical point R_r = 100 is the maximum point.

Compared to the load resistance R_L and generator resistance R_g, the radiation resistance R_r is relatively small. Consequently, a higher R_r is generally more desirable to achieve better radiation resistance.

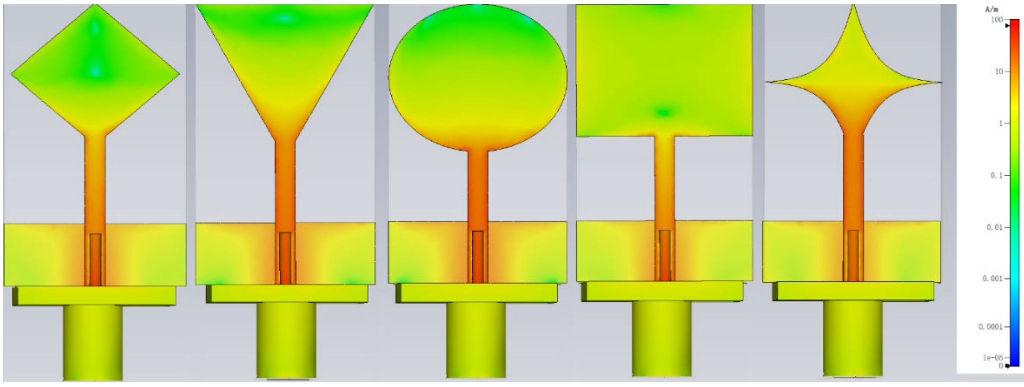

Figure 3.4 Average surface current of square-shaped patch, triangular-shaped patch, circular-shaped patch, rectangular-shaped patch and spear-shaped patch (from left to right).

While it is challenging to provide a specific analytical method for determining the radiation resistance of specific shaped patch antennas, examining the average surface current distribution can offer some insight into the radiation resistance. Figure X shows the surface current distribution of various patch shapes at 1.0 GHz. Among the figures, the spear-shaped patch exhibits a distinct current distribution that may contribute to its higher radiation resistance.

A spear-shaped patch with higher radiation ressistance is capable of radiating a higher amount of power than other regular-shaped patches. Moreover, radiation efficiency, $\eta = P_r/P_{in}$, is also enhanced when utilising a spear-shaped patch.

The benefits of increased radiation efficiency and higher power radiated, as observed in the spear-shaped patch design, have significant implications for various aspects of antenna performance and system operation. One such advantage is the improved signal strength, which enables the antenna to generate stronger electromagnetic signals, facilitating reliable transmission in environments where signal propagation is hindered by obstacles or interference (i.e. brain tissues). Furthermore, the increased radiation efficiency implies that the antenna is more effective at converting input power into radiated power, leading to better overall system performance. This improvement is particularly beneficial in applications where weak signals need to be detected or resolved. Additionally, the enhanced radiation efficiency and higher power radiated contribute to a more robust and reliable transmission, reducing signal loss or degradation. Lastly, the improved radiation characteristics of the spear-shaped patch offer greater flexibility in addressing diverse communication requirements and accommodating different operating conditions. This can simplify antenna design and enable the more effective utilisation of available resources, thereby contributing to the overall performance of the system.

The adoption of a spear-shaped patch in the microstrip antenna design led to improved impedance match, increased radiation resistance, higher power radiated and improved radiation efficiency. These benefits resulted in improved signal strength, enhanced system sensitivity and increased transmission reliability, ultimately contributing to better overall antenna performance and optimised signal propagation. Therefore, the spear-shaped patch was preferred for our microwave imaging system.

3.3 Performance of Printed Monopole vs Microstrip Antenna

3.3.1 Complex Impedance Analysis

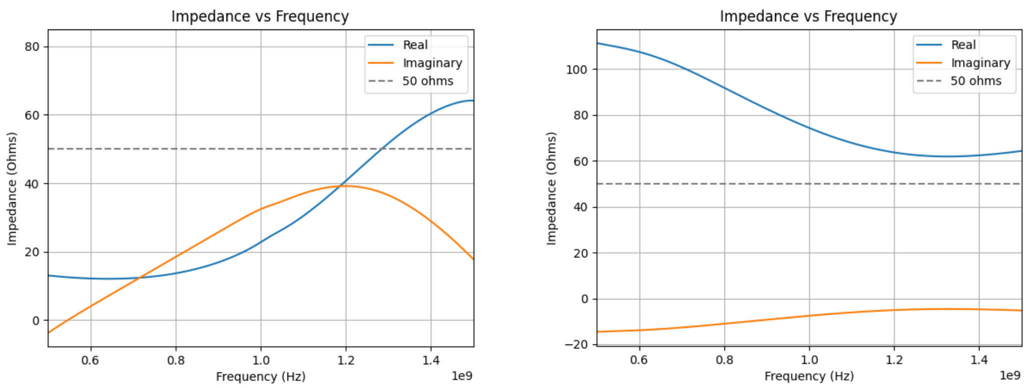

(a) (b)

Figure 3.5 Complex impedance of (a) microstrip antenna with ground plane covering the substrate and (b) printed monopole antenna with shortened ground plane.

To demonstrate the performance of proposed printed monopole, we compared its impedance with conventional microstrip patch antennas between 0.5 GHz and 1.5 GHz, as illustrated in Fig. 3.5 (a) (b). We calculated the impedance of both antennas using CST Microwave Studio.

For optimal performance, the real part of the impedance should be approximately 50 ohms, and the imaginary part should be close to 0 ohms. As demonstrated in Figure 3.5, the microstrip antenna with full ground plane exhibits a real part impedance closer to 50 ohms at 1.3 GHz. However, the imaginary part of the impedance at 1.3 GHz was around 40 ohms, which indicated an impedance mismatch at this frequency. For the Printed Monopole Antenna with Shortened Ground Plane (6.31mm), the real part of the impedance was nearest to 60 ohms at 1.3 GHz, with the corresponding imaginary part being approximately 7 ohms.

Considering the challenges associated with detecting signals above 1.5 GHz, as outlined in Section 1.3, the impedance of the printed monopole antenna with shortened ground plane at 1.3 GHz has been demonstrated to provide a better impedance match below the 1.5 ghz threshold. although the real part of the impedance was 60 ohms and the imaginary part was -7 ohms, the printed monopole antenna still offered a more advantageous impedance match compared to the microstrip antenna below 1.5 GHz, thus ensuring the optimal performance of the antenna within the desired frequency range.

3.3.2 E-field (0.5m) at 1.3GHz

A study of the E-field at 0.5 m from both the microstrip antenna with full ground plane and the printed monopole antenna with shortened ground plane (6.31mm) was performed at a frequency of 1.3 GHz. The results demonstrated distinct differences in the E-field distributions and peak values of the two antennas.

The printed monopole antenna exhibited a peak E-field value of 1.17 dB (V/m). The E-field distribution was isotropic in nature, surrounding the antenna uniformly. The main beam is oriented along the y' axis as shown in Fig. 3.6 (b), which was perpendicular to the patch. In contrast, the Microstrip Patch Antenna had a lower peak E-field value of -4.11 dB(V/m). The E-field distribution in this case was concentrated around the ground plane of the antenna, with the main beam directed along the z' axis as shown in Fig. 3.6 (a), pointing towards the rear of the antenna.

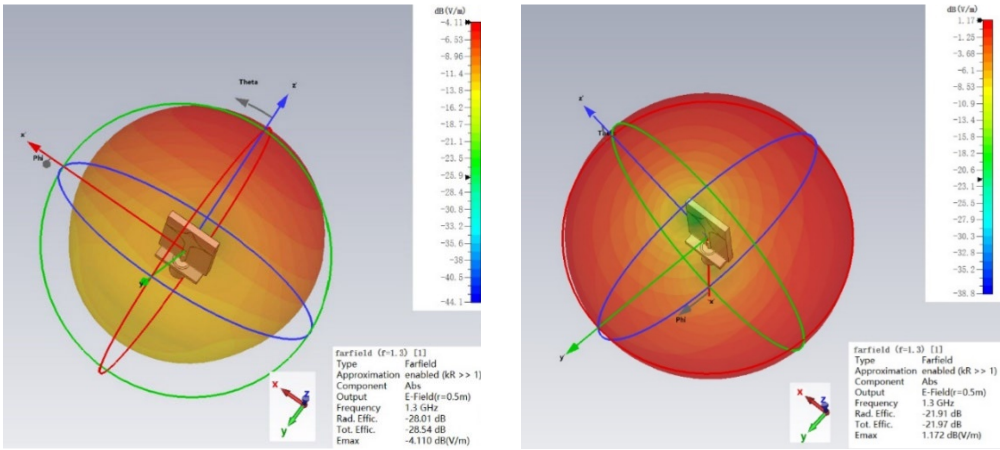

(a) (b)

Figure 3.6 E-field (0.5 m) at 1.3 GHz: (a) microstrip antenna with full ground plane and (b) printed monopole antenna with shortened ground plane.

The higher E-field value associated with the printed monopole antenna suggested greater efficiency in transmitting and receiving electromagnetic signals, which might contribute to enhanced overall system performance within the desired frequency range. Moreover, the increased peak E-field value implied that the printed monopole antenna could generate stronger signals, an attribute that could be advantageous in applications requiring communication over extended distances or in environments characterised by significant signal attenuation (i.e. microwave imaging for brain stroke detection). Additionally, the larger E-field value of the printed monopole antenna might indicate its heightened sensitivity to incoming signals, a feature that can be beneficial in applications where detecting weak signals is of vital importance.

3.3.3 Length of Ground Plane

The influence of the ground plane length on the operational bandwidth was investigated by varying the length parameter ‘d’, as depicted in Fig. 3.7 (a). The reflection coefficient plot in Fig. 3.7 (b) suggests that reducing the ground plane length effectively decreased the lower band-edge frequency of the proposed antenna. Given that the imaging system operates within the 0.5 GHz to 1.5 GHz range, a final ground plane length of 'd=4.9 mm' was selected, as it resulted in a lower band-edge frequency of 0.8 GHz and thus provided a broader bandwidth.

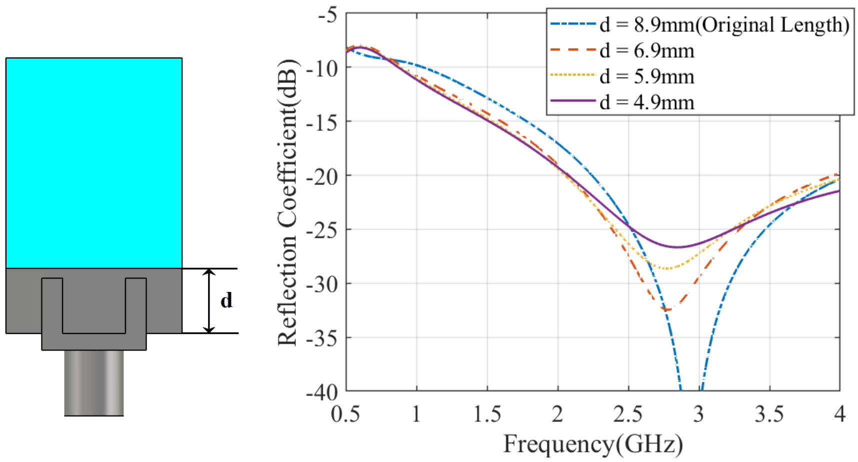

(a) (b)

Figure 3.7 Substrate optimisation (a) Geometry of rectangular ground in the back of proposed antenna; (b) reflection coefficient with different ‘d’ values.

3.3.4 Reflection Coefficient of Printed Monopole vs. Microstrip Antenna

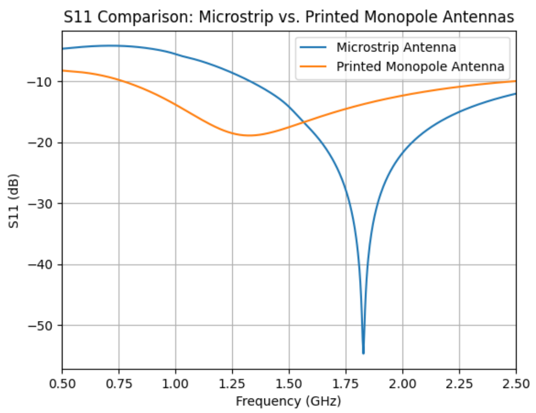

Figure 3.8 Reflection coefficient comparison of microstrip antenna with full ground plane and printed monopole antenna with shortened ground plane

Fig.3.8 shows the reflection coefficient of the printed monopole vs a microstrip antenna with the same dimension. The lower band-edge frequency of the printed monopole antenna is 0.75 GHz, with a resonant frequency of 1.3 GHz and a resonance level of -18 dB. Its operating bandwidth ranges from 0.75 GHz to 2.5 GHz. Conversely, the microstrip patch antenna has a lower band-edge frequency of 1.3 GHz, a resonant frequency of 1.8 GHz, and a significantly deeper resonance level of -55 dB. The operating bandwidth of the microstrip patch antenna begins at 1.3 GHz and extends beyond 2.5 GHz.

Within the desired frequency range of 0.5 GHz to 1.5 GHz, the printed monopole antenna offers a wider bandwidth. Although the resonance of the microstrip patch antenna at 1.8 GHz is much deeper, the printed monopole antenna's resonance of -18 dB at 1.3 GHz is more appropriate for the targeted frequency range. Furthermore, the lower band-edge frequency of the printed monopole antenna begins at 0.75 GHz, which indicates its potential for improved image reconstruction capabilities in the desired frequency range. As a result, the S_{11} of printed monopole antenna was deemed more advantageous for our microwave imaging brain stroke detection, considering the optimal frequency range and resonant frequency.

3.4 Exploring the Dimensions of ECA

3.4.1 Overall Dimension Analysis

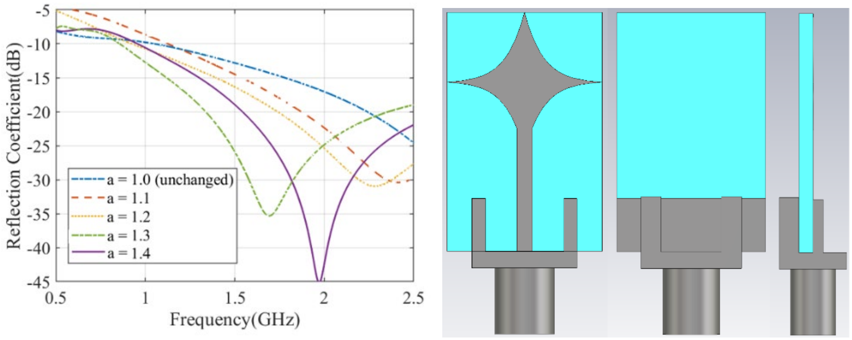

(a) (b)

Figure 3.9 Overall dimension analysis: (a) Reflection coefficient versus frequency for ‘a=1.0, 1.1, 1.2, 1.3, 1.4, 1.5’; (b) geometric structure of spear-shaped patch monopole.

We modified the overall dimensions of the antenna to optimise its working frequency. Considering that the lower band-edge frequency and resonant frequency were far beyond 1.5GHz, we multiplied the overall dimensions of the antenna by ‘a’; thus, to decrease the operation frequency, the dimensions of antenna were (21.475 × a) mm × (14.04 × a) mm× (1.7 × a) mm. The corresponding reflection coefficient for a = 1.0, 1.1, 1.2, 1.3, 1.4, 1.5 cases versus frequency are plotted in Fig. 3.9(a). Among the five cases, the dimension of antenna with mutiplier a = 1.3 showed wider bandwidth starting from around 0.8 GHz, lower resonanct frequency at 1.7 GHz and comparatively compact dimension, suggesting its promising charateristics at low frequency.

Therefore, we multiplied the original antenna dimensions by 1.3, after which the dimensions of antenna are modified to be 28.175 mm × 18.252 mm × 2.171 mm. Figure 3.7(b) shows the front, rear and side views of the modified antenna (from left to right). The substrate material was FR4 with a dielectric constant of 4.3, a loss tangent of 0.025 and a thickness of 2.171mm. The spear shape of patch was formed by exponential equation $y = 1.3 \times 1.7 \times e^{(1.3 \times x)/1.7+t}$, where the variable 'x' ranged from -6.18241 to 2.943564. The width and length of feedline were 1.82mm and 14.52mm, respectively. The length of the shortened rectangular ground on the back of the substrate was 7.31mm.

3.4.2 Dimension of Fabricated Antenna

We also fabricated this printed monopole antenna as illustrated in Fig. 3.10(a)(b), which had slightly different dimensions due to machining errors in the fabricating process. Specifically, the dimensions of fabricated antenna were 28.42 mm × 18.25 mm × 2.2855 mm. The width and length of feedline were 1.82 mm and 14.52 mm, respectively. Another difference was the connector between the antenna and coaxial cable, resulting in different resistance.

To keep the experiments consistent with the simulation, we remodelled the dimensions of the antenna in the simulation. The dimensions of remodelled antenna are shown in Fig. 3.10(c). The length, width and thickness of the antenna were 28.42 mm, 18.25 mm and 4.855 mm, respectively. The substrate material was FR4 with a dielectric constant of 4.3, a loss tangent of 0.025 and a thickness of 4.4 mm. The spear patch and rectangular ground were printed on the front and back of the substrate, respectively.

Reflection coefficients for the fabricated antenna in 8 experiments with 8 different feed cables were measured with the preliminary antenna, as shown in Fig. 3.10 (d). In the same figure, the simulation results of the mirror-copied antenna and the preliminary antenna are both plotted. The measured return loss of the fabricated antennas was consistent with the simulation results of the mirror-copied antenna, but differed significantly from the simulation results of the preliminary antenna in the frequency range between 1.4 and 3.0 GHz. Notably, the performance of all antennas was similar in the frequency range between 0.5 GHz and 1.4 GHz. It is worth noting that these frequencies are critical for microwave imaging systems due to their importance in achieving an optimal trade-off between reconstruction accuracy and penetration depth. Overall, the fabricated antenna met the requirements for the intended microwave imaging application.

Using Ray's equation, we estimated that the lower band-edge frequency of the modified antenna in 90% glycerine was 0.75 GHz. The simulation and experimental results as shown in Fig.3.10 (d) show that its lower band-edge frequency was around 0.75 GHz; this is identical to the estimation result. The proposed antenna had resonant frequency of around 1.3 GHz, with a magnitude of -19 dB. Its working frequency ranged from 0.75 GHz to 2.6 GHz, which covered a suitable frequency range for brain stroke detection.


(a)

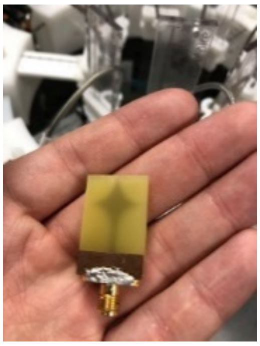
(b)

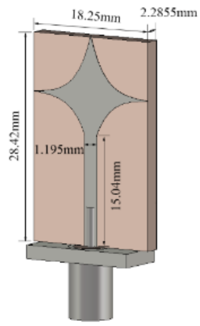

(c)

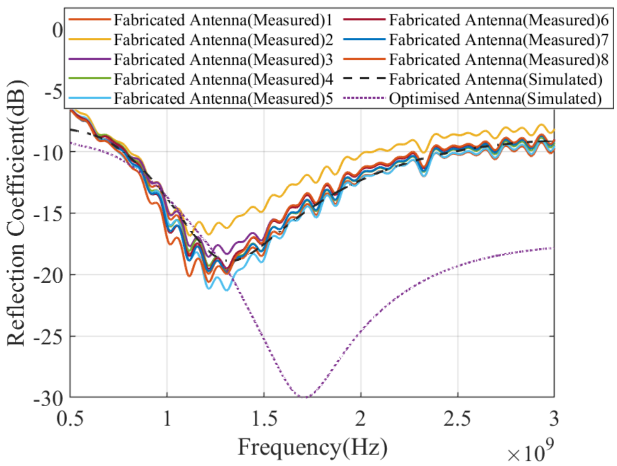

(d)

Figure 3.10 Illustration of fabricated antenna: (a) Front view; b) back view; (c) dimensions of fabricated antenna; (d) reflection coefficients curves for fabricated antenna in 8 experiments with 8 different feed cables, mirror-copied antenna and the preliminary antenna.

3.5 Simulation Performance of Fabricated ECA

3.5.1 Characteristics of ECA

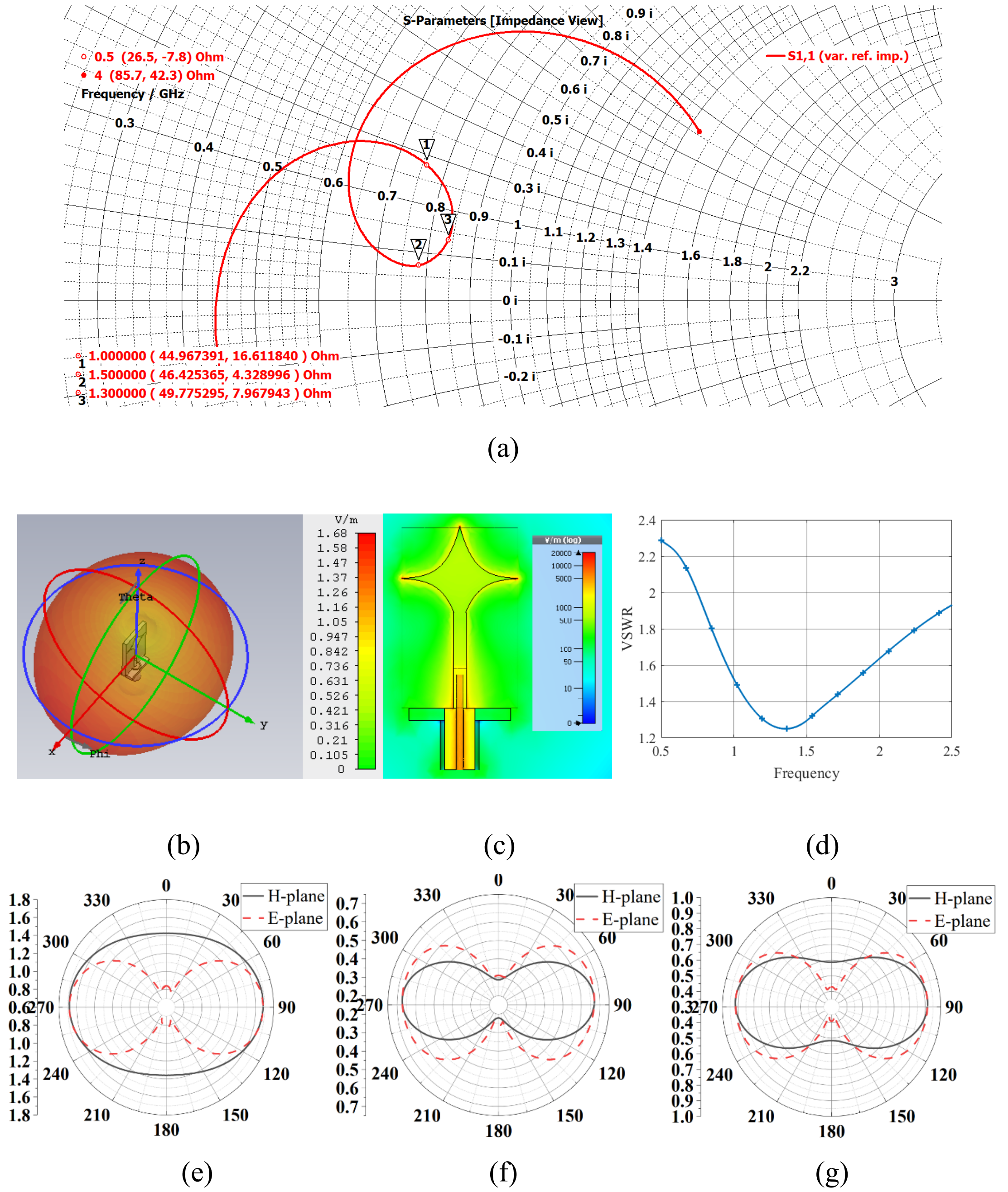

Figure 3.11 Characteristics of re-modelled antenna: (a) Smith chart of input impedance; (b) three dimension E-field (0.25 m) at 1GHz; (c) average surface E-field distribution at 1GHz; (d) VSWR; (e)-(h) E-field (0.25 m) at 1.0, 1.3 and 1.5 GHz.

We assessed the performance of the re-modelled antenna in 90% glycerine-water coupling liquid by plotting the impedance smith chart, 3D near-field (0.25 m) E-field pattern, surface current, Voltage Standing Wave Ratio (VSWR), and near-field (0.25 m) E-field pattern in Fig. 3.11. From smith chart, we obtained the input impedance of the remodelled antenna at 1.0 GHz, 1.3 GHz and 1.5 GHz. Fig. 3.11 (a) shows the characteristic input impedance values were 44.97, 46.43 and 49.775, respectively, at these frequencies. In addition, it shows that the real part of input impedance at each frequency are 38, 39 and 42, respectively. Furthermore, we can see from the result that the imaginary part of input impedance at each frequency was 13.5, 3.5 and 6.5, respectively. Fig. 3.11(b) shows the 3D perspective view of the E-field, which was almost isotropic. Fig.3.11 (e), (f) and (h) show the E-plane and H-plane of E-field pattern (0.25 m) at 1.0 GHz, 1.3 GHz and 1.5 GHz, respectively. The near-field radiation direction is almost isotropic at 1.0 GHz, while at 1.3 GHz and 1.5 GHz, it was almost parallel to the substrate plane of the antenna, which is normal to our desired radiation direction. Considering that antennas typically operate in a conformal array surrounding the brain, these undesired radiation directions could lead to significant mutual coupling between adjacent antennas. To eliminate the effect of mutual coupling, a safe distance between antennas had to be considered. Fig. 3.11 (c) shows that the surface current was mostly distributed near the fringes of the patch and feedline, suggesting that a significant portion of signals were generated from the feedline, leading to spurious radiation. From Fig.3.11 (d), the VSWR shows the input impedance was best matched with the transmission line at 1.4 GHz.

3.5.2 Transmission Coefficient Level between Antennas

In practice, the noise level, which is -100 dB, has to be considered as any microwave with transmission level lower than this floor will not be detected in experiments[9], [178], [179]. Thus, we conducted a transmission level study between two antennas.

We modelled two mirror-copied antennas in the CST simulation. The two antennas were arranged in a facing configuration, with their radiating surfaces directly opposite each other, at a distance of 130 mm, as shown in Fig. 3.12 (a). The transmission level is plotted in Fig.3.12 (b). The transmission coefficients between 0.5 GHz and 1.7 GHz were above the noise floor. Signals could be detected in our desired frequency range, which is 0.5 GHz – 1.5 GHz; this suggested the proposed antenna was experimentally efficient.

(a)

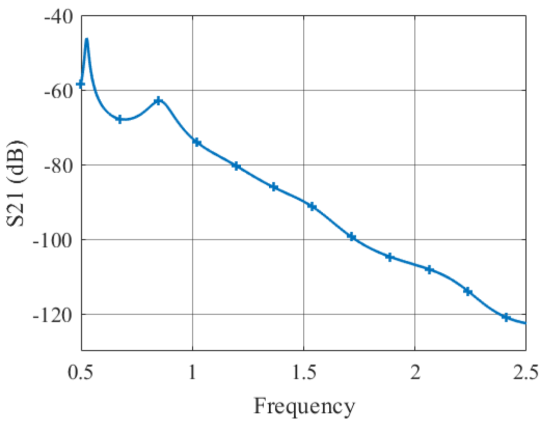

(b)

Figure 3.12 Antenna configuration and transmission analysis: (a) Illustration of two antennas arranged in a face-to-face configuration; (b) transmission coefficient S_{21} vs frequency.

Chapter 4 Aperture-Coupled Fed Antenna Design

Aperture-coupled antennas (ACA) offer several advantages over printed monopole antennas. One of the main advantages is improved radiation efficiency. The aperture-coupled feeding method is more efficient than the edge-fed monopole design, leading to higher radiation efficiency and better antenna performance. Additionally, ACAs provide better isolation between the feed line and the radiating patch, which reduces the impact of spurious radiation. This, in turn, results in improved antenna performance and reduced interference. Another advantage of ACAs is wider bandwidth. ACAs offer wider bandwidths than printed monopole antennas, making them more versatile and suitable for a wider range of applications. Moreover ACAs provide lower cross-polarisation compared to printed monopole antennas due to the symmetry of the configuration, which makes them well-suited for high-precision applications [79], [115], [117]–[119], [180]–[185]. In this chapter, we will compare ACAs with printed monopole antenna discussed in the previous chapter to explore the advantages and disadvantages of each type.

However, there are also some disadvantages to using ACAs. One of the main challenges is that the design of ACAs is more complex compared to that of a printed monopole antennas [99], [101], [183], [186]. The spacing between the patch and the feed line must be optimised to ensure efficient coupling and minimise spurious radiation, which can be a time-consuming and complex process [79], [80], [181]. Additionally, ACAs may still suffer from reduced bandwidth in certain designs, despite offering wider bandwidths than microstrip antenna or printed monopole antennas [183], [184]. Another challenge of ACAs is the more difficult fabrication process compared to printed monopole antennas [183]. The fabrication of ACAs requires precise alignment of the feed line with the patch element to ensure optimal performance, which can be difficult to achieve in practice [115]. Finally, in some cases, printed monopole antennas may provide a slightly higher gain compared to ACAs [116], [118]. However, the advantages of ACAs in terms of radiation efficiency, spurious radiation, wider bandwidth, and lower cross-polarisation make them a popular choice for high-performance applications.

Overall, the choice between ACAs and printed monopole antennas depends on the specific requirements of the application. For high-performance applications, where precise beam steering and reduced unwanted radiation are required, ACAs offer superior performance. However, for applications where simplicity and cost-effectiveness are the primary considerations, printed monopole antennas may be more suitable.

4.1 Initial Prototype of ACA

Our objective of changing the feeding method was to model an antenna with a wide operation bandwidth, deep resonance and directional radiation pattern based on equivalent circuit theory and the nature of the aperture-coupled feeding method. Starting from the dimension of ECA, we proposed the initial dimensions of ACA, with the caveat that ACA is thicker as there are double substrate layers for the aperture coupled feeding method. It is worth noting that, to achieve load impedance matched with input impedance, the total thickness of the substrate required further investigation, so we initialised the thickness of the front substrate layer as 2 mm and the back substrate layer as 3 mm as the first trial.

Based on the equivalent circuit analysis, radiation pattern and surface current analysis, we designed and modelled in CST Microwave Studio the ACA with the same spear-shaped of the forementioned edge coupled monopole antenna. To optimise the ACA, we analysed the ACA’s input impedance and we and modified it to matches with the generator impedance by changing each parameter value of the ACA, i.e., size of slot, length of feedline, thickness of substrate, substrate material, etc.

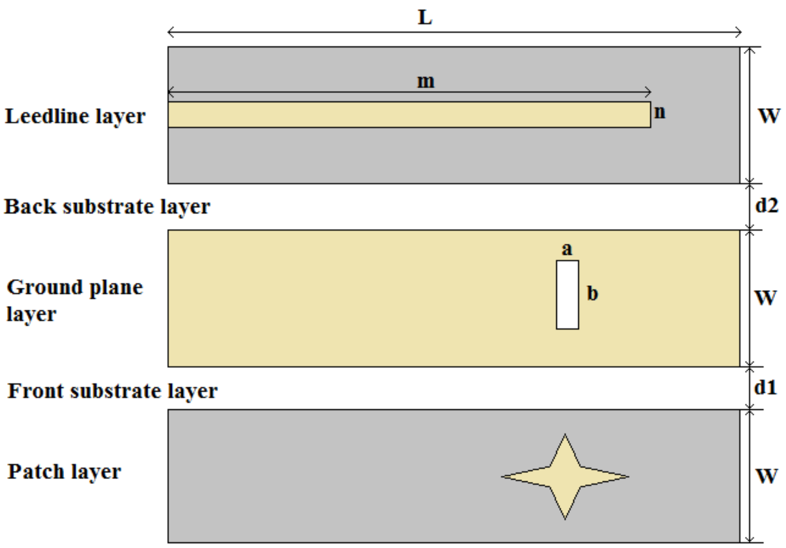

Figure 4.1 Layers of an aperture coupled antenna.

4.2 Equivalent Circuit and Input Impedance of ACA

Microstrip patch antennas and printed monopole antennas have simpler structures, making their performance easier to predict with analytical or numerical methods. Empirical design guidelines and computational electromagnetic simulation tools can be employed for optimisation, which reduces the necessity of equivalent circuit analysis in these cases. Nevertheless, equivalent circuit analysis can still offer valuable insights for better optimisation when needed.

In the case of aperture-coupled antennas, the equivalent circuit is particularly important because it helps designers identify optimisation directions amidst the complex interactions of various influencing factors. Without analysing the equivalent circuit, determining the necessary steps for optimisation becomes a challenging task. Thus, equivalent circuit analysis plays a more critical role in the design and optimisation process for aperture-coupled antennas.

A variety of antenna parameters, including shape, dimension, and material property, affect antenna characteristics, such as impedance, resonant frequency, transmission level, and radiation pattern. The opposite is also true: any optimisation on a single antenna parameter may affect multiple characteristics of the antenna. Thus, it is almost impossible to design an ACA with a trial-and-error method. Equivalent circuit theory illustrates that an antenna could be viewed as a circuit consisting of a series of resistors, inductors and capacitors depending on how current is distributed in the antenna and what role each component plays. Given that the impedance of each component can be adjusted by changing its dimensions, materials, shapes, etc., we can control the characteristics of the antenna.

Electrical current generated from the port source passes through three electric circuit branches. We analyse the power flow in the equivalent circuit to optimise the antenna.

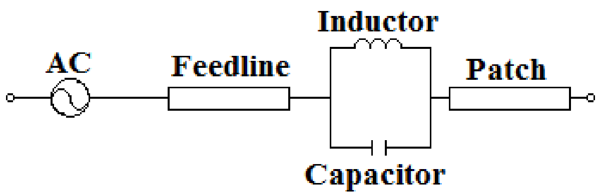

Figure 4.2 First branch of the equivalent circuit.

In the first circuit branch as shown in Fig. 4.2, the AC from the signal generator travels to the feedline. It is then coupled into the patch through the back substrate, the rectangular slot in the ground plane and the front substrate. In the equivalent circuit, the signal generator is assumed as alternating current (AC) power source with 50 Ω resistance and 0 reactance. On the patch and feedline, a part of power is dissipated as heat, another part is radiated as microwaves into outer space. In this circuit, the feedline and patch act as resistors. At the same time, the feedline and patch are viewed as the upper and lower conductive plates of both capacitor and inductor. Between the feedline and the patch, the back and front substrates are treated as the medium of both the capacitor and the inductor. Therefore, the antenna impedance of the first circuit is expressed as

$$\mathrm{Z_{circuit1}}=\mathrm{R_f}\angle 0^0+\mathrm{R_p}\angle 0^0+X_L\angle 90^0+X_C\angle{-90^0}$$

$$\text{or}\ \mathrm{Z_{circuit1}}=\mathrm{R_f}+\mathrm{R_p}+j(2\pi fL-\frac{1}{2\pi fC})$$

, where $\mathrm{R_f}$ is the resistance of the feedline, $\mathrm{R_p}$ is the resistance of the spear patch, L is the inductance of the parallel plates comprised of feedline, back substrate, front substrate and patch, C is the capacitance of the parallel plates, $\angle 0^0$ is the phase angle for both resistors, $\angle 90^0$ is the phase angle of inductance and $\angle -90^0$ is the phase angle of capacitance.

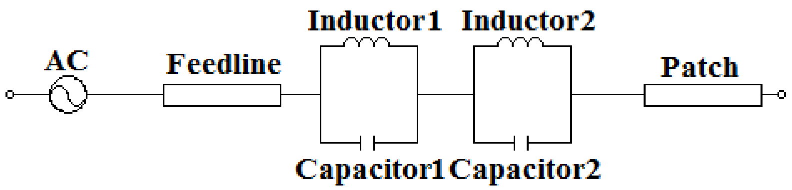

Figure 4.3 Second branch of equivalent circuit.

Similar to the first circuit branch, the AC generated from the signal generator distributes on the feedline. The equivalent circuit is plotted in Fig. 4.3. Travelling through the back substrate, the current is coupled to the ground plane. Then, the AC passes through the front substrate, and it is coupled to the patch. The feedline, ground plane and patch are treated as resistors. The feedline, back substrate and ground plane are viewed as a pair of capacitor and inductor. Ground plane, front substrate and patch comprising another capacitor and inductor set. The impedance of the second circuit is expressed as:

$$Z_{circuit2}=R_f\angle 0^0 + R_{gp}\angle 0^0 + R_p\angle 0^0 + X_{L1}\angle 90^0 + X_{C1}\angle -90^0 + X_{L2}\angle 90^0 + X_{C2}\angle -90^0$$

, where L_1 and C_1 are the equivalent components of the first parallel plates, L_2 and C_2 are the equivalent components of the second parallel plates and R_{gp} is the resistance of ground plane. Considering that inductors are in series and capacitors are in series, we can express the $Z_{circuit2}$ as:

$$Z_{circuit2}=R_f + R_{gp} + R_p + j[2\pi f(L_1+L_2) - \frac{1}{2\pi f}(\frac{C_1+C_2}{C_1C_2})]$$

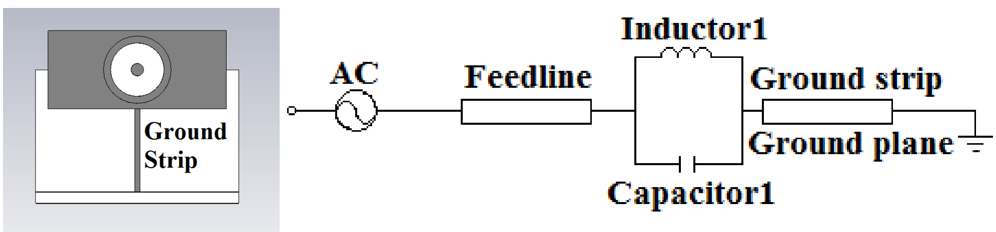

Figure 4.4 Third branch of equivalent circuit.

In the third circuit branch, the AC passes through the feedline, back substrate plane and ground plane. It then reaches the ground end of the coaxial cable through a ground strip as shown in Fig. 4.4 In this circuit branch, the feedline, ground plane and patch strip are treated as resistors. The feedline, back substrate, and ground plane together form an inductor and capacitor connected in series. We can express the impedance of the antenna in the third circuit as:

$$Z_{circuit3} = R_f \angle 0^0 + R_{gs} \angle 0^0 + R_{gp} \angle 0^0 + X_{L1} \angle 90^0 + X_{C1} \angle -90^0$$

$$\text{or } Z_{circuit3} = R_f + R_{gs} + R_{gp} + j(2\pi f L_1 - \frac{1}{2\pi f C_1})$$

, where the R_{gs} and R_{gp} refer to resistance of the ground strip and ground plane.

It is worth noting that besides the spear-shaped patch, signals also radiate out from the feedline, ground plane and ground strip. We refer these radiations as spurious radiations. However, most of the signals generated from the feedline and ground plane are shielded by the ground plane and patch, respectively. As a result, spurious radiation in ACA is largely reduced.

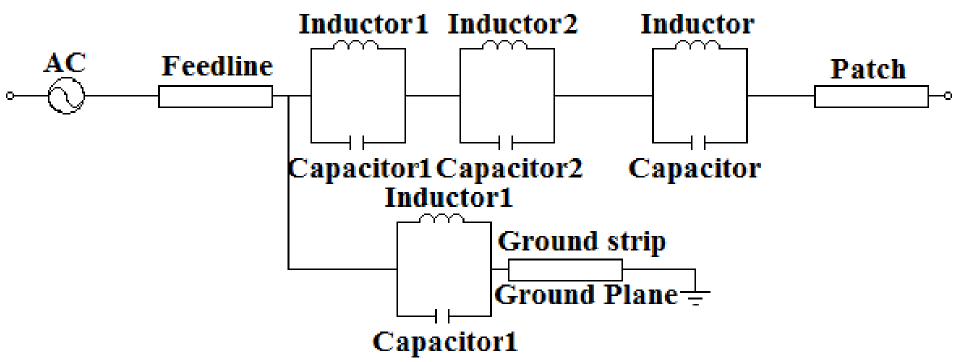

Figure 4.5 Equivalent Circuit of ACA.

Taking these three branches of the equivalent circuit into consideration, the overall circuit of the antenna is presented in Fig. 4.5 The total impedance of the ACA is expressed as:

$$Z_{total} = R_f + R_p + R_{gs} + R_{gp} + j[(X_L + X_{L1} + X_{L2})//X_{L1} - (X_C + X_{C1} + X_{C2})//X_{C1})]$$

$$\text{or } Z_{total} = R_f + R_p + R_{gs} + R_{gp} + j[\frac{2\pi f}{\frac{1}{(L+L_1+L_2)}+\frac{1}{L_1}} - \frac{1}{2\pi f(\frac{1}{\frac{1}{C}+\frac{1}{C_1}+\frac{1}{C_2}}+C_1)}]$$

The inductance and capacitance can be approximated using the formulas for a pair of paralleled plates. Generally, they are given by:

$$L = \frac{\mu_0 \mu_r dl}{w}$$

$$C = \frac{\varepsilon_0 \varepsilon_r wl}{d}$$

, where μ_0 is permeability of the free space and equals $4\pi \times 10^{-7} \frac{Henry}{m}$, μ_0 is the relative permeability of the substrate, ε_0 is the permittivity of free space and equals $8.854 \times 10^{-12} \frac{Farad}{m}$, ε_r is the relative permittivity of medium, d is the distance between spear and feedline, l is the length of the substrate and w is the width of the substrate. We note that the conductive plates in our study were irregularly shaped, e.g., a spear-shaped patch and strip-shaped feedline, so these formulas for L and C are only used as approximations, not for accurate calculations. Between biplanar plates, the L and C have the following relation regardless of the shape of the plates:

$$L \times C = \varepsilon_0 \varepsilon_r \mu_0 \mu_r l^2$$

This relation reveals that its capacitance is negatively related to its inductance between biplanar plates, given that ε_r μ_r l are fixed.

4.3 ACA Optimisation

4.3.1 Same Material for Both Substrates

First, we studied the effect of applying different dielectric materials as substrate material for an ACA. Performance of ACA was studied using different substrate materials with distinct relative permittivity. We studied representative materials including RT3010, RT3206, FR4, RT5880 and RT5880LZ, with relative permittivity of 11.2, 6.6, 4.3, 2.2 and 2.0, respectively. Since there are two layers of substrate for ACA, i.e., front and back substrate, we discussed applying both the same material scenario in this section and different material scenarios in section 4.3.2.

The return loss of the antenna with different substrates is shown in Fig. 4.6(b). Lower band-edge frequency and resonant frequency decrease with an increase in the substrate's relative permittivity. A wider bandwidth was observed with the use of lower relative permittivity material. In terms of the return loss performance alone, the performance of RT3010 was the most desired.

Furthermore, with regards to practical experiments, a noise level of -100 dB had to be considered, as microwaves with a transmission level lower than this noise floor cannot be detected. Therefore, we studied the transmission levels between antennas. Two antennas with the same materials and dimensions are arranged confronting each other at 120 mm, as shown in Fig. 4.6(a). We plot the S_{21} transmission coefficients of antenna with different substrate permittivity in Fig. 4.6(b). We could see that the transmission coefficient level of lower relative permittivity material was higher. Considering that the noise floor of our microwave imaging system was -100dB, antennas with higher coefficients were deemed more experimentally feasible. RT5880LZ with widest frequency range from 0.5 GHz to 1.2 GHz among these materials was comparatively suitable for our imaging system.

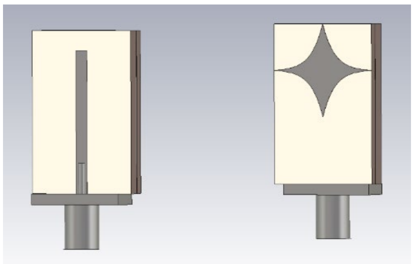

(a)

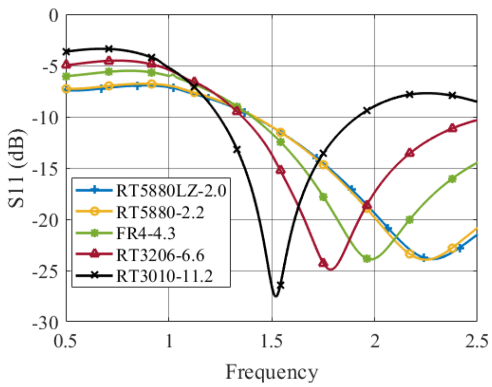

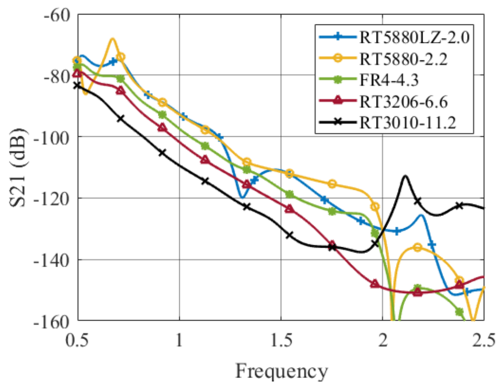

(b) (c)

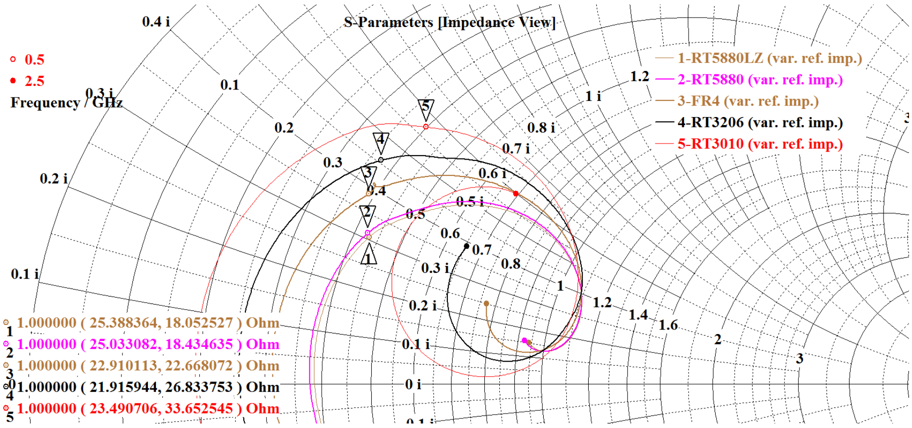

(d)

Figure 4.6 Substate material comparison: (a) Layout of antenna under test; (b) return loss; (c) S_{21}; (d) Smith chart.

The Smith chart in Fig.4.6 (d) shows the input impedance of the above-mentioned cases between 0.5GHz and 2.5GHz. The previous section discussed the noise level of the imaging system is -100 dB. Fig. 4.6(c) suggests transmission level of antenna using each substrate material is mostly higher than the noise floor except RT3010 at 1 GHz. In addition, a microwave imaging system can detect target in most case at 1 GHz. Subsequently, we mainly discussed the Smith chart at 1 GHz. Switching from low relative permittivity to high relative permittivity, the imaginary part increased from 15.4, 15.7, 19.2, 22.8 to 28.6. The resistance ranged from 21.5, 21.2, 19.5, 18.6 and 20, among which the RT5880LZ substrate was highest. We also noticed that the characteristic input impedance of the antenna with RT5880LZ substrate was 25.388364, which was the highest among all the materials. As discussed in our methodology, to optimise antenna performance, higher resistance and lower reactance are preferred. Therefore, RT5880LZ with the highest resistance, reactance and characteristic input impedance was preferred as the substrate material.

This can be explained by equivalent circuit theory. In capacitors, the relative permittivity ε_r is positively related to capacitance in the parallel plate, thus negatively related to X_C. We could see from the Smith chart that the positivity of the imaginary part was "+", suggesting the magnitude of inductance impedance dominated in the reactance impedance. The inductance was not changed with the increase of ε_r, the magnitude of capacitive reactance dropped with the increase of ε_r. As a result, the magnitude of reactance increased as ε_r gets bigger. Thus, the minimal magnitude of the reactance was achieved when ε_r was the smallest.

4.3.2 Different Materials for Front and Back Substrate

We studied the effect of using different substrate materials for the front and back substrates in one antenna by analysing Case 1 – 5 as detailed in Table 4.1. We note that Case 1 utilised RT5880LZ for both substrates and served as a control group; it is presented here for comparison with the other cases.

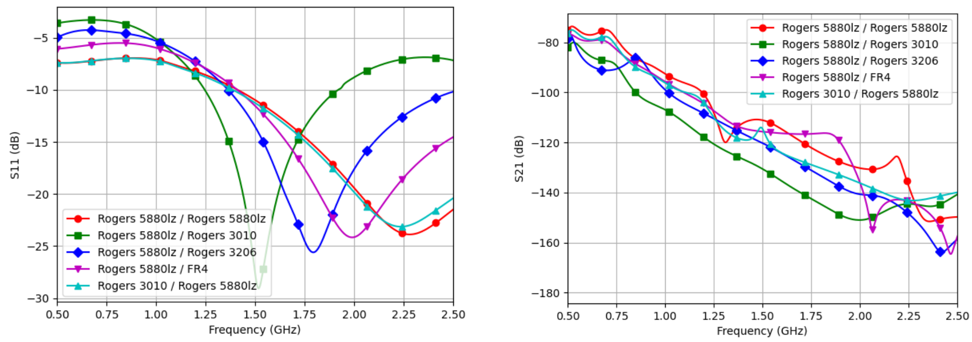

(a) (b)

Figure 4.7 Performance of antenna with different front and rear substrate materials: (a) S_{11} vs frequency; (b) S_{21} vs frequency.

The return loss vs frequency of these five cases is plotted in fig. 4.7 (a). The lower band-edge frequencies of Case 1 – 5 are 1.4 GHz, 1.25 GHz, 1.35 GHz, 1.4 GHz, 1.4 GHz, respectively. The higher band-edge frequencies of each case are above 1.9 GHz.

Transmission coefficients S_{21} for each case are plotted in Fig. 4.7(b) to compare experimentally operational frequency band, where the transmission level remains above the noise level of -100 dB. We approximated the capacitance of each case as shown in Table 4.1.

Since $d_1 = 2$ mm, $d_2 = 3$ mm and P is a fixed value, we can treat capacitance C as the function of ε_1 and ε_2:

$$C(\varepsilon_1, \varepsilon_2) = P\frac{\varepsilon_1\varepsilon_2}{3\varepsilon_1+2\varepsilon_2}$$

The partial derivatives of the above function are:

$$\frac{\partial C(\varepsilon_1,\varepsilon_2)}{\partial \varepsilon_1} = \mathrm{P}\frac{2{\varepsilon_2}^2}{(3\varepsilon_1+2\varepsilon_2)^2}$$

$$\frac{\partial C(\varepsilon_1,\varepsilon_2)}{\partial \varepsilon_2} = \mathrm{P}\frac{3{\varepsilon_1}^2}{(3\varepsilon_1+2\varepsilon_2)^2}$$

As we know P>0, ε_1>0 and ε_2>0, partial derivatives are positive, so lowest capacitance is achieved when ε_1, ε_2 were the smallest.

Among these five cases, we observed an increase in experimentally operational frequency bandwidth with an increase in capacitance: Case 1 with the smallest capacitance of 0.4P had the widest experimentally operational frequency range from 0.5 GHz to 1.2 GHz. The experimentally operational frequency range of Case 2 with the highest capacitance of 0.7887P was the narrowest, from 0.5 GHz to 0.85 GHz. This suggests the capacitance of Case 1, which used the same materials for both substrates, is more experimentally suitable in the desired frequency range between 0.5 GHz and 1.5 GHz.

Table 4.1 Parameters of substrates with different materials.

	Case 1	Case 2	Case 3	Case 4	Case 5
Front substrate	RT5880LZ 2.0	RT5880LZ 2.0	RT5880LZ 2.0	RT5880LZ 2.0	RT3010 11.2
Back substrate	RT5880LZ 2.0	RT3010 11.2	RT3206 6.6	FR4 4.3	RT5880LZ 2.0
Capacitance	0.4000P	0.7887P	0.6875P	0.589P	0.5957P

4.3.3 Total Thickness of Substrate

We also discussed the optimisation of substrate thickness. Considering the total thickness applied in section 4.3.2 was 5 mm, and the conclusion that a thicker substrate results in smaller total capacitance of substrates, we studied the effects of applying the RT5880LZ substrate with total thickness of 8 mm, 10 mm and 12 mm. Their total equivalent capacitance was 0.2500P, 0.2000P and 0.1667P, respectively.

Their return loss is plotted in Fig. 4.8(a). The starting frequency and resonant frequency decreased with the increase of the total thickness of the substrate, resulting in a wider bandwidth. The transmission coefficients for each case are plotted in Fig.

4.8(b). The transmission coefficient of the antenna showed a trend of climbing with an increase in thickness.

Considering that the lower band-edge frequency and resonant frequency of the 12 mm thickness were the smallest among the three thickness; and that the experimentally operational frequency range of both the 10 mm and 12 mm thickness were 0.5 GHz – 1.85 GHz, the final total thickness of two substrate was finalised as 12 mm. It is worth noting there are still optimisation potentials through enlarging the thickness of the substrate, but we stopped increasing its thickness because the antenna was already quite thick and continuing to thicken the substrate could result in only slight improvement to the antenna, as the total capacitance could only be reduced by a small mount. For example, the capacitance would only be reduced by 0.0238P when switching its thickness from 12 mm to 14 mm.

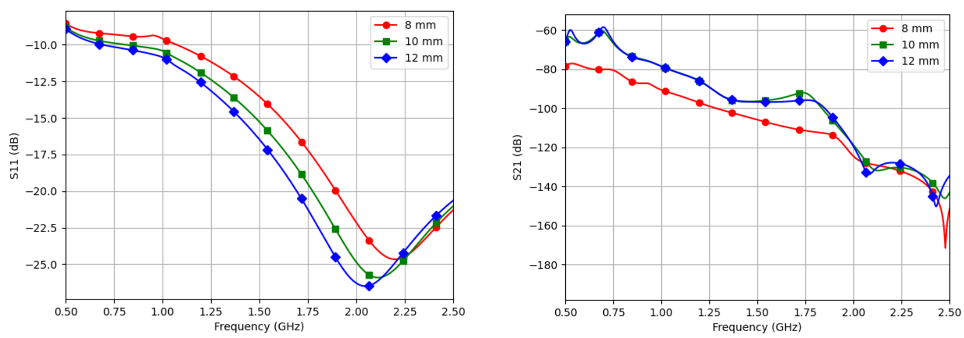

(a) (b)

Figure 4.8 Performance of antenna with 8, 10, 12 mm total thickness: (a) S_{11} vs frequency; (b) S_{21} vs frequency.

4.3.4 Thickness of Front and Back Substrate

In order to further optimise antenna performance, we studied the allocation of the front and back substrate thickness. Table II lists three cases with varying allocations of front and back substrate thickness, all having a total substrate thickness of 12 mm. Fig. 4.9(a) suggests that the return loss for Case 3 had the lowest starting frequency and resonant frequency. Fig. 4.9(b) shows small S_{21} differences between the three cases, but we observed that the S_{21} of Case 3 is slightly higher than the other two cases, especially at 1.0 GHz and 1.5 GHz, which were our preferred frequencies for image reconstruction. Consequently, Case 3 was selected, where the thickness of front substrate and back substrate were set as 1 mm and 11 mm, respectively.

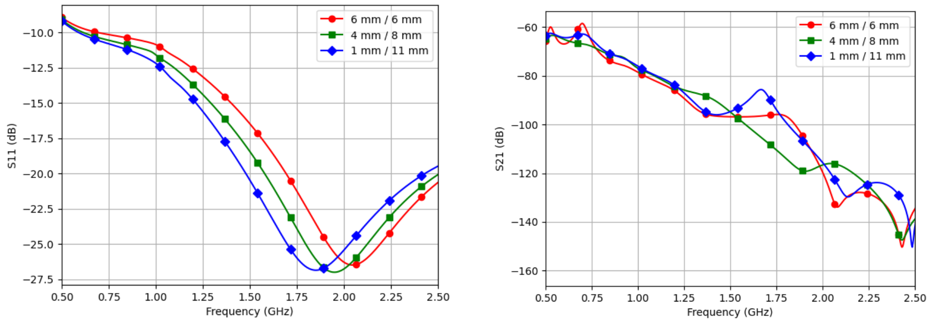

(a) (b)

Figure 4.9 Performance of antenna with different front and rear substrate thickness: (a) S_{11}vs Frequency; (b) S_{11} vs Frequency.

Table 4.2 Parameters of substrate with different thickness

	Front substrate thickness	Back substrate thickness	Front substrate Capacitance	Back substrate Capacitance
Case 1	6mm	6mm	0.33P	0.33P
Case 2	4mm	8mm	0.5P	0.25P
Case 3	1mm	11mm	2P	0.18P

Ultimately, compared with ECA, the length of the substrate was increased by 6 mm and its thickness was increased to 12 mm, while the width of substrate remained the same. The substrate's material was changed from FR-4 to Rogers RT5880LZ, with a relative permittivity of 2.0 and tanδ of 0.0021. The rectangular ground part on the back of the substrate was also eliminated. A 34.42 mm × 18.25 mm × 0.035 mm rectangular metal (PEC) ground plane with a 10 mm × 2 mm × 0.035 mm rectangular slot was inserted in the middle of the front and back substrates. The microstrip line was positioned on the back of ACA substrate. The geometry of the spear-shaped patch remained unchanged. The final dimensions of ACA were 34.42 mm × 18.25mm × 12.00 mm.

4.4 Comparison of Characteristics between ECA and AVA

4.4.1 Reflection Coefficient and VSWR

To assess the impact of the proposed aperture-coupled feeding approach, we compared the performance of the ACA with that of the ECA in simulations with CST Microwave Studio. The CST-calculated reflection coefficients for these two antennas placed in a tank with a mixture of 90% glycerine and 10% water are plotted in Fig. 4.10(b).

The proposed aperture-coupling design resulted in wider frequency bandwidth and deeper resonance. Importantly, the larger bandwidth provided more flexibility in the use of multiple frequencies, which has been shown to increase the robustness of iterative microwave tomographic algorithms [5], [71]. This enhancement from 0.5 GHz is particularly important for MWT applications, where antennas must operate efficiently below 1.5 GHz.

To evaluate their impedance matching status, we also calculated their voltage standing wave ratio (VSWR). The impedance bandwidth (VSWR < 2) of the ECA starts at 0.75 GHz and ends at 2.5 GHz. In comparison, the VSWRs of proposed ACA were maintained below 2.0 throughout our desired frequency range, with most of them lower than 1.5. This improved performance of VSWR and return loss confirms that the ACA is better matched than the ECA across the frequency range of interest.

4.4.2 Near-field Electric Field Characteristics

We also compared electric field (E-field) distributions for both antennas in the near-field, at an indicative distance of 25 cm. The E-field of ECA at 1.0, 1.3 and 1.5 GHz are shown in Fig. 4.10 (e) – (g), respectively. The E-field intensity of the ECA was highest in the direction perpendicular to the patch, with a maximum value of 1.68 V/m at 1.0 GHz. The E-field of ACA at 1.0, 1.3 and 1.5 GHz are shown in Fig. 4.10 (h) – (j). The peak E-field intensity for the ACA were observed in the direction normal to the patch, with a maximum value of 1.47 V/m at 1.0 GHz. Compared with the ECA, the ACA's E-field exhibited a more directional pattern, better aligning with our desired propagation direction towards the human head.

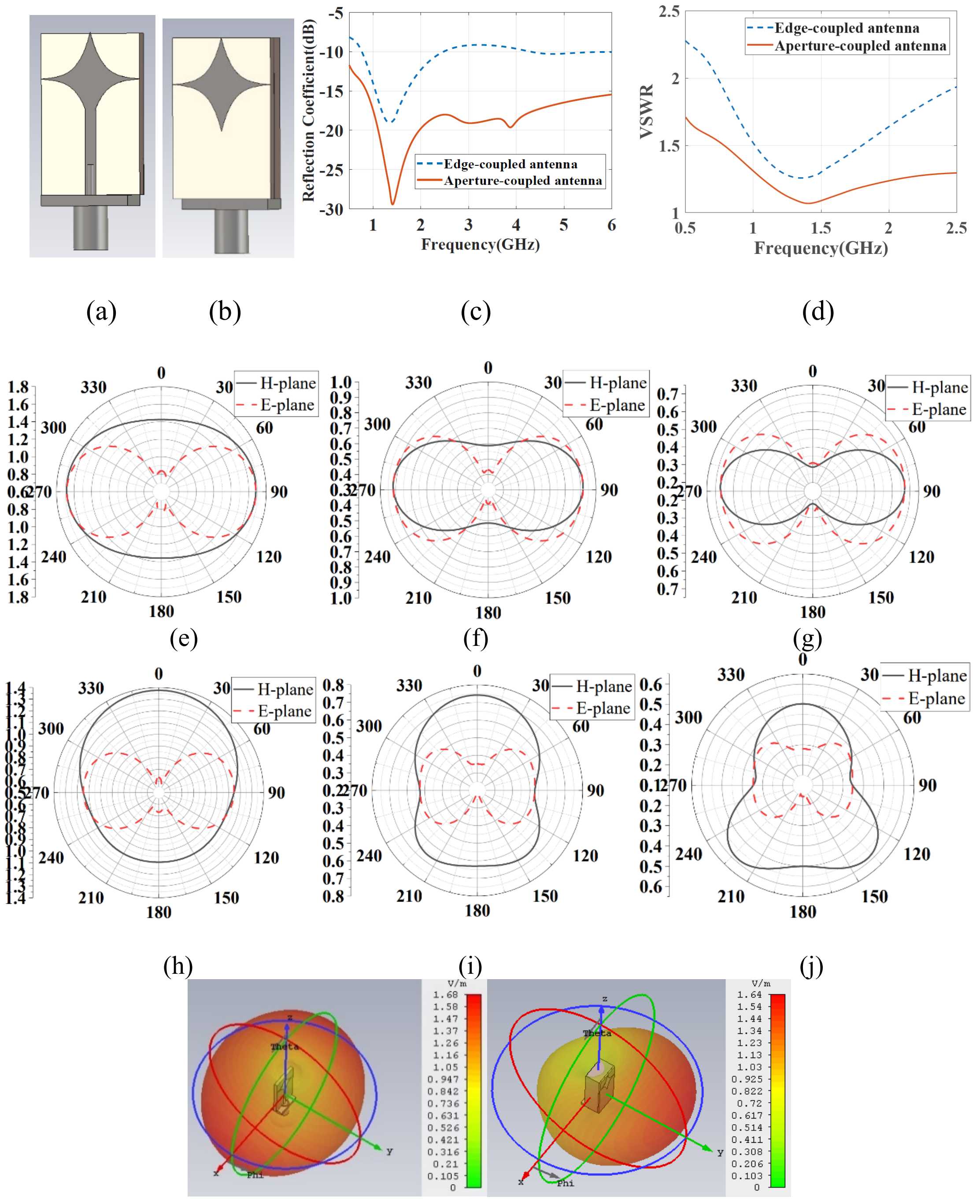

Figure 4.10 Characteristics of ECA and ACA: (a)(b) ECA and ACA structure; (c) reflection coefficients of ACA and ECA; (d) VSWRs of ACA and ECA; (e)-(g) E-field (0.25 m) of ECA at 1.0, 1.3 and 1.5 GHz; (h)-(j) E-field (0.25 m) of ACA at 1.0, 1.3 and 1.5 GHz; (k)(l) 3D E-field (0.25 m) of ECA and ACA at 1GHz.

3D E-field distributions of ECA and ACA are shown in Fig. 4.10(k)(l), respectively. We observed that the ACA's E-field was primarily distributed in front of the radiating patch, while ECA's E-field spread to the sides, resulting in less efficient coverage of our imaging region of interest. The observed near-field characteristics of the ACA suggest that it has the potential to not only reduce mutual coupling between adjacent antennas but also minimise the influence of undesired backscattering caused by other factors, such as the antenna or surrounding environment.

4.4.3 Far-field Characteristics

We also compared far-field characteristics for both antennas, such as directivity and realised gain. The results for three different frequencies are shown in Fig. 4.11.

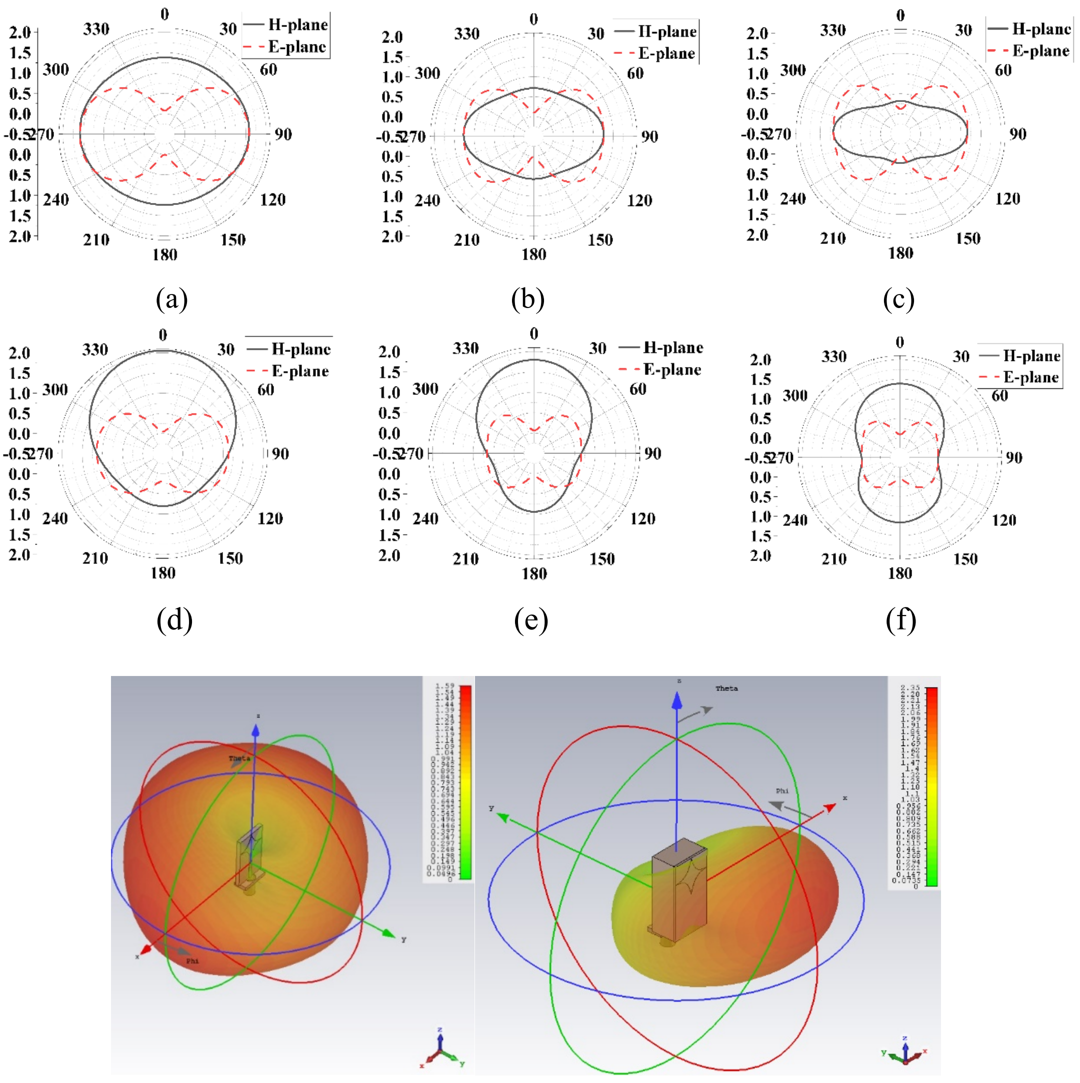

Figure 4.11 Far-field (1 m) radiation pattern: (a)–(c) radiation pattern of ECA at 1.0, 1.3 and 1.5 GHz; (d)–(f) radiation pattern of ACA at 1.0, 1.3 and 1.5 GHz; (g)(h) 3D E-field of ECA and ACA at 1 GHz.

The far-field directivity patterns for the ECA at 1.0, 1.3 and 1.5 GHz are plotted in Fig. 4.11(a)(b)(c), respectively. Its directivity was highest in the directions perpendicular to the patch of the antenna, with a maximum value of 2.0 dBi at 1.0 GHz. Then, we plotted the directivity at the same frequencies for ACA as shown in Figure 4.11 (d)(e)(f). Its directivity was highest in the direction normal to the patch of the antenna, with a peak value of 3.12 dBi at 1.0 GHz. Compared with the ECA, the ACA's directivity was much higher in the direction normal to the patch plane of the antenna, which was our desired propagation direction. Moreover, the ACA's directivity was lower in other directions relative to the ECA. The ECA's gain reached its maximum value of -22.6 dB at 1.0 GHz in the direction perpendicular to the patch, while the highest value of -23.1 dB was in the direction normal to the patch for the ACA.

We also studied the 3D far-field radiation patterns of ECA and the ACA in Fig.4.11(g)(h). Radiation patterns for both antennas were measured at 50 cm in the glycerine–water mixture coupling liquid. As a monopole antenna, the ECA showed a typical isotropic radiation pattern. In contrast, the ACA showed directive radiation pattern suggesting fewer signals directly travels to adjacent antennas without going through the brain phantom. Thus, more received signals in the ACA array carry useful information to differentiate the brain area's dielectric property difference between the with-target in the brain and no-target in the brain.

Chapter 5 Study of Antenna Arrays

5.1 Immersing Coupling Liquid

The use of coupling liquids is a promising technique for reducing the reflection of microwave signals when radiating into the human head. The electrical properties of the coupling liquid play a critical role in the performance of the technique. Free space has much lower conductivity and permittivity compared to head tissues, which results in significant signal loss and reflection.

In prior studies conducted by our research group, we developed various coupling liquids and experimentally measured their electrical properties [187]–[189]. This experimental approach allowed us to investigate the effectiveness of different liquids in reducing the reflection of microwave signals when radiating into the human head. Such studies are essential in guiding the selection of an appropriate coupling liquid for various applications, including medical imaging and wireless communication systems. The choice of a suitable coupling liquid can significantly impact the quality of the signal or image received, which underscores the importance of characterising the electrical properties of the liquid and selecting the appropriate material for a specific application.

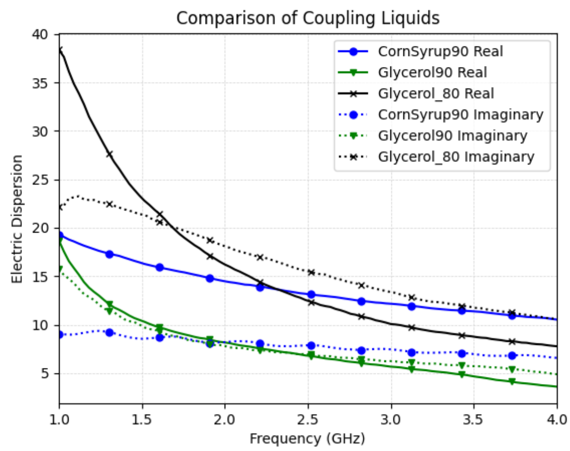

Figure 5.1 Electric dispersion comparison of coupling liquids.

In this study, we plotted the electric dispersion of three different matching liquids: Corn syrup, 80% glycerine-20% water mixture and 90% glycerine-10% water mixture, which were experimentally measured by Syed *et al.* in our research group to compare their electrical properties in enhancing received signals. The selection of the appropriate matching liquid was based on a comparison of the real and imaginary parts of permittivity (ε' and ε'') among the tested materials. Among the tested liquids, the real part of 90% glycerine was found to be similar to FR4, which has a permittivity of 4.3, making it a promising candidate for use as a matching liquid. Although the eps'' of 90% glycerine were not always the lowest among the three materials, the similarity of its real part to FR4 was deemed a critical factor in its selection. Therefore, 90% glycerine was applied as a coupling liquid throughout this study.

5.2 Design and Analysis of Microwave Imaging Scanners

Various kinds of head scanners for brain stroke systems have been introduced and presented and they share some common characteristics. Antennas for the array were designed as small as possible to enable more antenna elements while keeping the head scanner compact. They were designed to work in the frequency range of 0.5GHz and 1.5GHz, which maintains a good balance between penetration depth and imaging resolution [1], [30], [190]. They were placed in close proximity to the head, which minimises the form factor of the head scanner and increased the received signal strength by shortening the distance between the transmitter and receiver. A lossy coupling liquid with permittivity comparable to the average brain was utilised to reduce the mutual coupling of adjacent antennas and to decrease the signal loss at the inter-surface between scalp and environment.

5.2.1 Simulation of the Headband Scanner

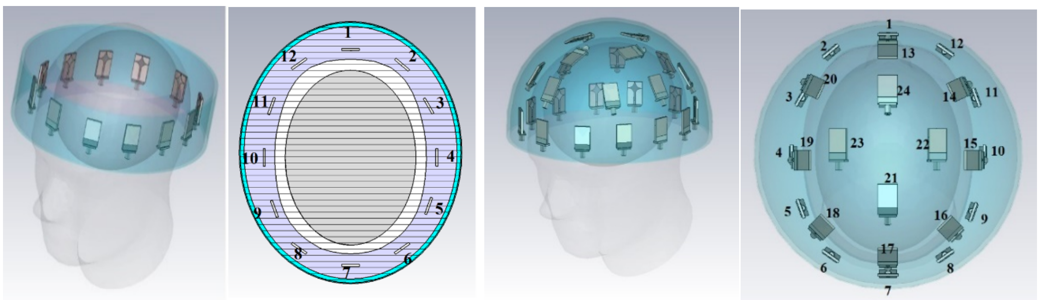

(a) (b) (c) (d)

Figure 5.2 Two proposed MWT scanners: (a) headband scanner; (b) antenna array layout in headband; (c) helmet scanner; (d) antenna array layout in helmet.

We incorporated the spear-shaped antenna studied in the previous section into two different head scanner designs, which we studied via CST simulations. The optimal number of antennas for MWI imaging of the head in terms of reconstruction stability, resolution and accuracy was studied in [141], [142]. Twelve antennas covering only a circular ring were used for the headband. The distance between adjacent antennas will have an impact on data quality due to mutual coupling, as will the distance between the antennas and the head due to signal attenuation. To balance the trade-off between minimising mutual coupling and other unwanted signals and maximising energy penetration into the head, a lossy coupling/immersion liquid was required. In this preliminary study, we used the same 90% glycerine mixture with 10% water, which was used by our initial imaging prototype, as shown in Fig. 5.2, and that was also used as ab immersion liquid for our antennas in the previous section.

Fig. 5.2 (a) and (b) show the perspective view and top view of the proposed headband scanner. The headband comprised 12 antennas arranged uniformly inside a lossless, Teflon-based elliptical headband filled with the mixture of 90% glycerine and 10% water. The array is placed in close distance to the skull, around 10.0 mm on average, facing the centre of the head. The height of the headband was 65.0 mm, and the major and minor axes of its elliptical cross-section were 260 mm and 220 mm, respectively.

5.2.2 Simulation of Helmet Scanner

Our proposed brain stroke MWI helmet comprises three main parts. The first part is the antenna array, which is made up of three rings of 24 evenly distributed antennas. Of these three rings, the bottom ring is composed of 12 antennas, the middle ring consists of 8 antennas and the top ring is made up of 4 antennas. The second part is the head phantom, which consists of two parts: the average brain and the skull. The last part of this system is the helmet, which consists of coupling liquid between antennas and head model, a tank holding the coupling liquid and an absorber as the outermost layer, which could minimise noise level and keep the system operating stably and reliably.

The geometry of the proposed helmet scanner is shown in Fig. 5.2(c)(d). To compare the performance with the headband, we assumed that the helmet was made of a material with the same properties as the mixture of 90% glycerine and 10% water used as the coupling liquid. We also considered an acrylic helmet holder and an

ECCOSORB MCS absorber with thickness of a 1.0 mm covering the helmet. The antennas were positioned a short distance from the skull, similar to the headband's distance (around 10mm) and facing the centre of the head. We constructed this helmet in CST Microwave Studio by using two separate objects – a hemisphere and a cylinder beneath the hemisphere, and then using the Boolean add operation to create the final helmet structure. The heights of the hemisphere and cylinder were 125 mm and 20 mm, respectively. The diameters and thicknesses of both the hemisphere and the cylinder were 250 mm and 4 mm, respectively.

5.3 Modelling of Head and Blood Targets

These scanners were designed in conjunction with the head model shown in Fig. 5.1(a), which was provided in CST (EN 50361 Specific Anthropomorphic Mannequin - SAM). This two-layer head phantom comprises a skull and homogeneous average brain tissue, with dielectric constants of 20 and 45.8, respectively. The major and minor axes of the elliptical phantom's axial slice at the height where the antennas are located are 153 mm and 112mm, respectively.

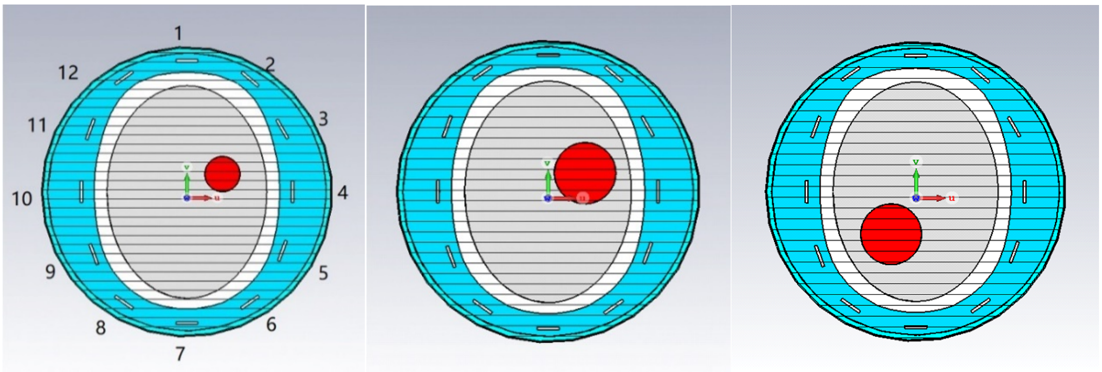

(a) (b) (c)

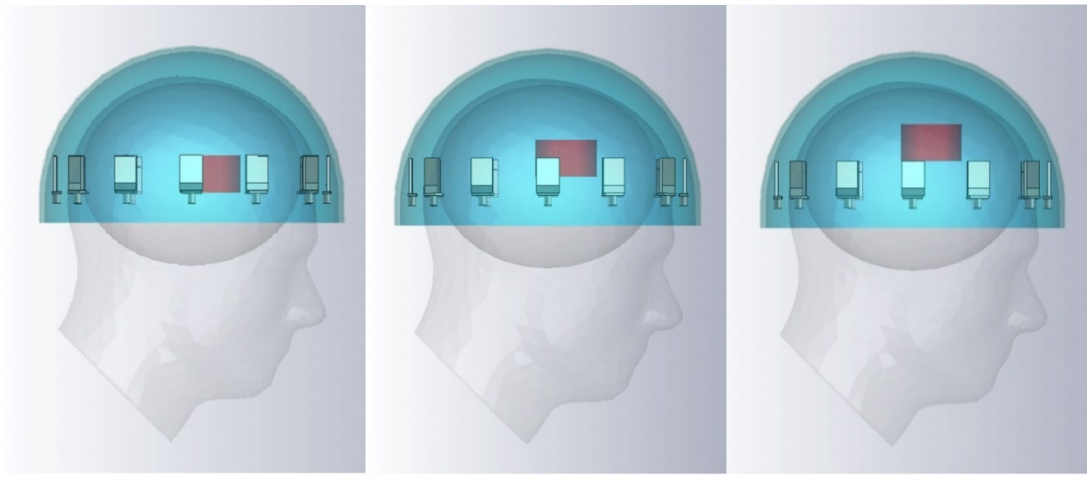

(d) (e) (f)

Figure 5.3 Illustration of target in helmet: (a) Target B at Location 1; (b) Target A at Location 1; (c) Target A at Location 2; (d) Target A at Height I; (e) Target A at Height II; (f) Target A at Height III.

To compare the detection capability of the two scanners, blood-like targets with different dimensions were inserted at different locations inside the head model, as shown in Fig.5.3 (a)-(f). The blood target has permittivity of 61.06 and conductivity of 1.58 at 1.0 GHz. Although the actual diameter of the smallest blooding area could be 1, 2 mm or even smaller, 30 mm and 50 mm in diameter are common, we start from this point, and we optimised the resolution step by step. We considered cylindrical targets in this study, as they will be easier to replicate in future experiments required to validate our designs.

Table 5.1 Dimension, position and height of target

Study Name	Size of Target	Target Position
a. Study on Different Target Size (A:50mm,30mm; B:30mm,20mm)	A	Location 1 &Height I
	B	
b. Study on Different Location (1: 30mm,20mm,0mm; 2: -20mm,30mm,20mm)	A	Location 1
		Location 2
c. Study on Different Height (I: 30mm,20mm,0mm; II: 30mm,20mm,15mm; III: 30mm,20mm,30mm)	A	Height I
		Height II
		Height III

To assess the detection capability of scanners, blood-like cylindrical targets with permittivity of 61.06 and conductivity of 1.58 at 1.0 GHz were inserted to the brain model, as shown in Fig.5.7(a). First, two sizes of target, i.e., Target A with dimension of 50 mm × 30 mm and target B with dimension of 30 mm × 20 mm, were modelled at the same location as shown in Fig. 5.3(a)(b) to assess the sensitivity to different sizes of target. Second, to assess the detection ability for different positions, Target A are modelled at position 1 with u, v, w (30 mm, 20 mm, 0 mm) and Position 2 with u, v, w (-20 mm, 30mm, 0 mm). Then, we modelled the target at three heights: Height I with u, v, w (30mm, 20mm, 0 mm), Height II with u, v, w (30 mm, 20 mm, 15 mm) and Height II with u, v, w (30 mm, 20 mm, 30 mm), to assess the detection capability for different height. The detailed modelling information of the blood target is displayed in Table 5.1. We considered cylindrical targets in this study, as they will be easier to replicate in future experiments required to validate our designs.

5.4 Transmission Level Comparison between Headband and Helmet Scanners

To compare signal transmission levels for the two scanners in the frequency range of interest, transmission coefficients were calculated at 0.5 GHz, 1.0 GHz and 1.5 GHz for the target location shown in Fig. 5.2 (a), (d).

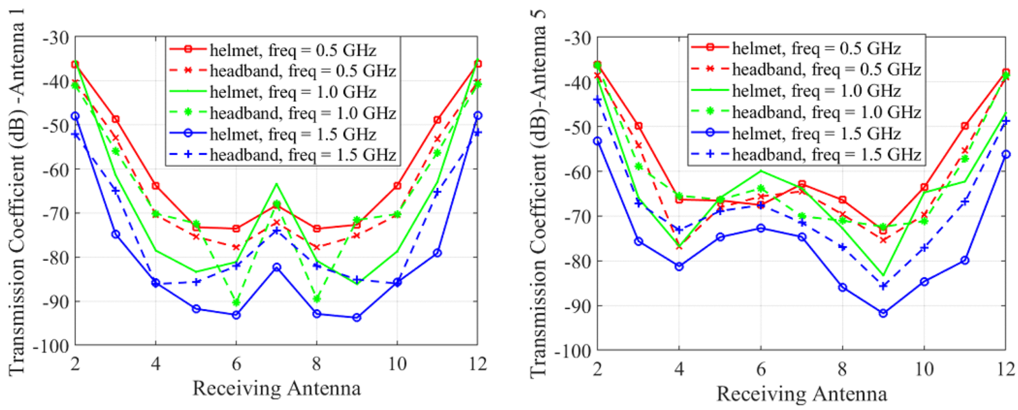

(a) (b)

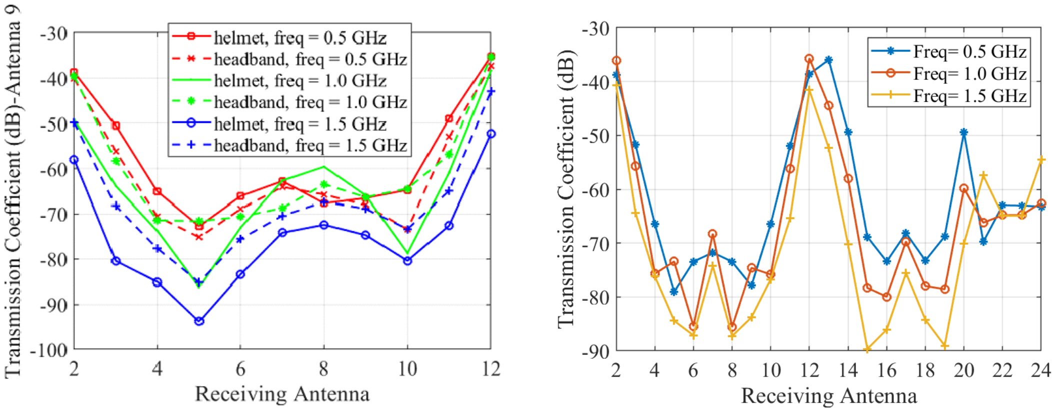

(c) (d)

Figure 5.4 Transmission coefficients of helmet and headband scanners for different antenna transmitters and three frequencies: (a) S_{n1} in head band; (b) S_{n5} in headband; (c) S_{n9} in headband; (d) S_{n1} at various frequencies in helmet.

Plots of transmission coefficients at each of the 12 receiving antennas are shown in Fig. 5.4, where the antennas were numbered in the clockwise direction shown in Fig. 5.2 (b). We chose to plot results for the following transmitters: Antenna 1 behind the head, Antenna 5 in the front-left of the head and Antenna 9 in the front-right of the head. These plots corresponded to the bottom 12-element ring of the helmet, which can be directly compared to the 12-element headband. The plots in Fig. 5.4 indicate that all transmission coefficients were higher than -100 dB, which was above the measurement noise level for our measurement equipment.

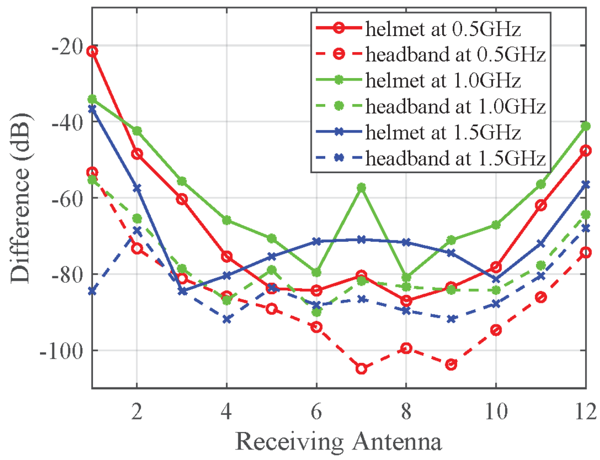

Figure 5.5 Transmission coefficient difference in dB between signals with and without the blood target for both scanners

To evaluate the sensitivity of the two scanners to the blood target, we have calculated the transmission coefficient difference of the signals with and without the target. We again compared results for the headband scanner (dashed lines) and the bottom array of the helmet scanner (solid lines) in Fig. 5.5 for transmitting Antennas 1 and 5. The differences in these plots were higher for the helmet scanner, suggesting that the helmet was more sensitive to the target response. Most of the signal differences were above the noise level, which implies that the target was detectable by both scanners.

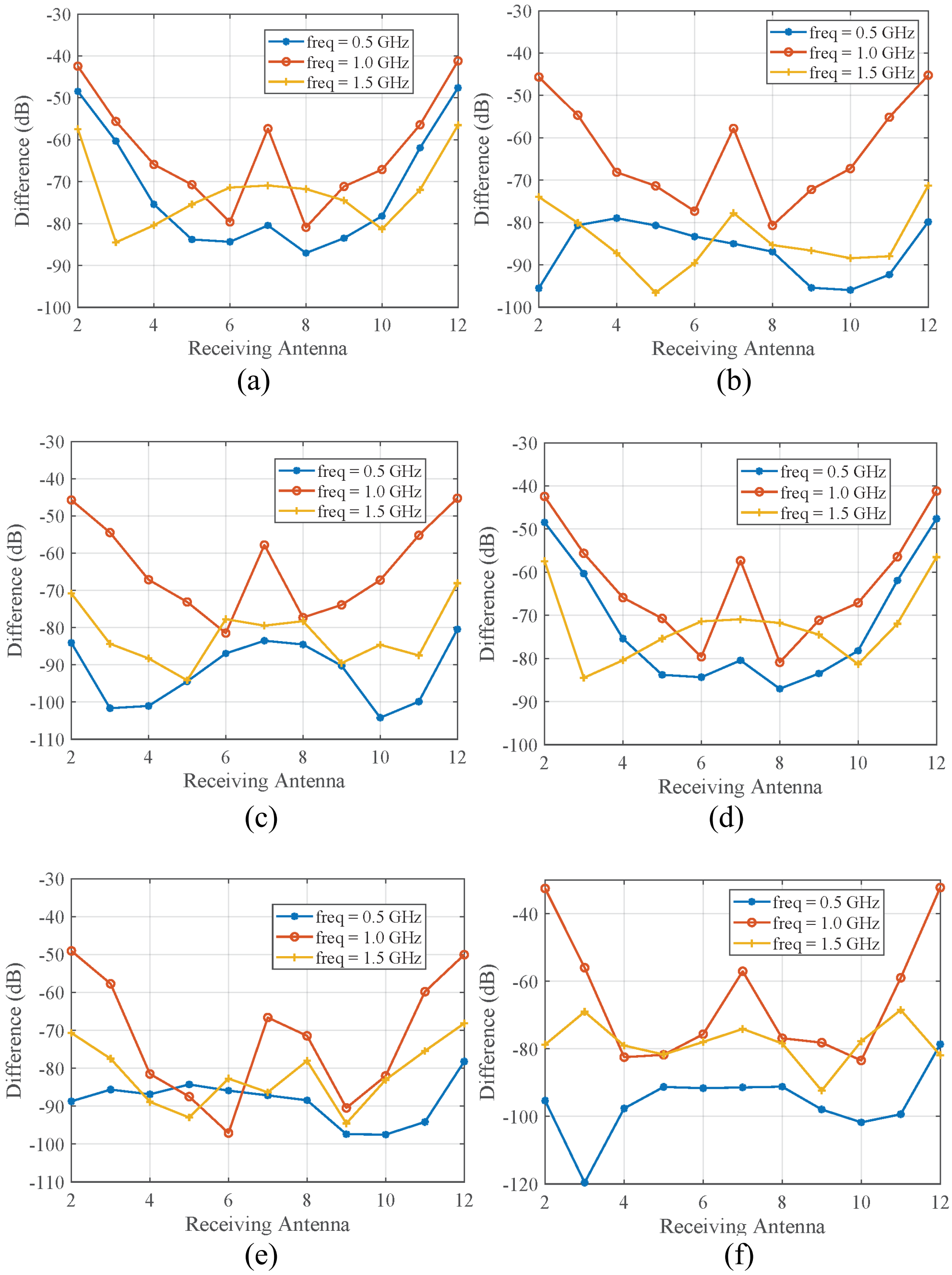

Figure 5.6 Magnitude difference of transmission coefficient in dB between signals with and without the blood target when antenna 1 transmits signal at three frequencies: (a) and (b) the results of Target size A and B, corresponding to the Study a in Table 5.1; (c) and (d) the results of Location 1 and 2, corresponding to the Study b. (b), (e)and (f) are the results of Height I, II and III, corresponding to the Study c.

To further assess the sensitivity of the helmet scanner to the target response, we plotted the same transmission coefficient difference as in headband in Fig. 5.5(a)-(f), but for the different target cases depicted in Fig. 5.7. Antenna 1 acted as transmitter in all of these cases. The plots in these figures suggest that the signal differences are correlated with the target size and location.

5.5 Model and Target Type, Size and Location

Our CST simulations use the SAM head model shown in Fig. 5.7(a) (EN 50361 Specific Anthropomorphic Mannequin) with a skull-mimicking layer (ε_r=20, σ=0.76 S/m at 1.0 GHz). We inserted an ellipsoid filled with a homogenous material mimicking average brain tissue (ε_r=45.8, σ =0.35 S/m at 1.0 GHz) inside the skull to construct a simplified two-layer head model. The head model was surrounded by 8- or 12-element elliptical arrays using the ECAs and ACAs, as shown in Figs. 5.7 (b) – (e). Analysing the results from 8 and 12 antenna arrays allowed us to assess the trade-off between increasing views and mutual coupling for the two different antenna designs.

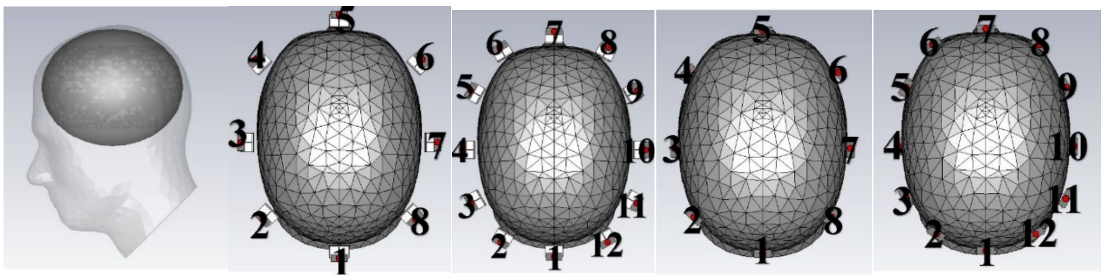

(a) (b) (c) (d) (e)

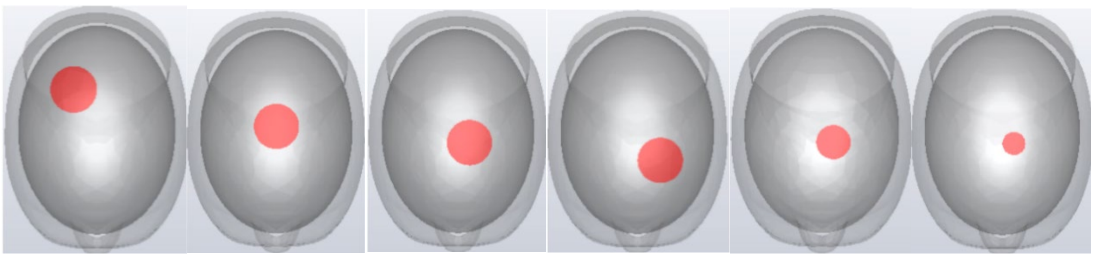

(f) (g) (h) (i) (j) (k)

Figure 5.7 Illustration of the head model and target.

Table 5.2 Target dimensions and locations

Parameter	Description	Location
Location I	Right rear	x, y, z (-20mm, 30mm, 0mm)
Location II	Centre	x, y, z (-0mm, 0mm, 0mm)
Location II	Left front	x, y, z (10mm, 15mm, 0mm)
Location IV	Left front	x, y, z (20mm, -30mm, 0mm)
Target A	Biggest size	Diameter, Height (40mm, 30mm)
Target B	Middle size	Diameter, Height (30mm, 30mm)
Target C	Smallest size	Diameter, Height (20mm, 30mm)

The antennas in these arrays were arranged uniformly at a distance of 5 mm from the skull, facing its geometric centre. The height of both arrays was 65.0 mm, and their major and minor axial lengths were 260.0 mm and 220.0 mm, respectively. We used a 90% glycerine–10%water mixture as a coupling and immersion liquid. To analyse the detection capability of the scanners, we placed a blood-like target at four different locations inside the head model, as shown in Fig. 5.7(f)–(i). We also modelled three different target sizes for one of these locations (Location III in Table I and Fig. 5.7(h), which are depicted in Fig. 5.7 (h)–(k). The target dimensions and locations are summarised in Table 5.2. The target material was blood-mimicking tissue with permittivity of 61.06 and conductivity of 1.58 at 1.0 GHz.

5.6 Transmission Level Comparison between ECA Array vs ACA Array

The previous section showed that aperture-coupled feeding can improve spear-shaped antenna characteristics. However, this comes at the expense of significantly increasing the substrate thickness, which results in weaker signal transmission and reception. The patch dimensions were the same for the two antenna designs, thereby allowing identical arrangements in the MWI arrays. The aim of this section is therefore to assess the benefits and challenges of using the ACA vs the ECA in MWI setups. For example, practical systems must take into account that the ability to accurately measure weak signals may be compromised by the presence of noise in standard MWI measurement equipment such as vector network analysers (VNAs). On the other hand, improving detection requires minimising unwanted coupling or multipath signals via careful antenna design.

To this end, we simulated the interaction of MWI arrays comprised of ACAS and ECAs with a simplified head and stroke model in the CST. To analyse and compare the impact of the two antenna designs on MWI array performance, we first calculated and plot signal transmission levels for the two arrays. We then studied the detection sensitivity and accuracy of MWI scanners comprised of 8- and 12-antenna arrays via MWT reconstructions with our DBIM-TwIST algorithm [71], [191], [192].

To evaluate the received signal sensitivity for the ECA and ACA arrays in these simple numerical experiments, we calculated the received signal strength at each receiver when one of the array elements was transmitting. Fig. 5.8 plots this signal strength as a function of the receiver number for each transmitter at 1.0 GHz. These plots represent the calculated signal difference (in dB) between the with-target and without-target cases when an antenna acted as transmitter, and the remaining antennas act as receivers. The x-axis label in these plots represents the antenna receiver in a sequence that started with the antenna that was next to the transmitter and moved clockwise, as in Fig.5.7 (b). For example, if Antenna 1 is a transmitter, then Antenna 2 is numbered as Receiver 2, Antenna 3 is numbered as Receiver 3. Fig. 5.8(a)(b) correspond to the no-target case scanned with the 12-ACA scanner and the 12-ECA scanner, respectively. These plots demonstrate that the signal strength of the ECA scanner was approximately 20 dB higher than that of the ACA scanner, confirming our previous observations regarding radiation loss caused by the aperture, reduced coupling efficiency of the aperture, and dielectric and conductor losses introduced by the thick substrate and ground plane. However, since the transmission coefficients for both ACA and ECA scanners were above -100 dB and -90 dB, respectively.

It is crucial to consider that the signal levels in practical experiments are influenced by a variety of factors. Measurement noise from instruments such as VNA can affect the accuracy of readings, making it challenging to obtain precise transmission coefficients at very low levels like -100 dB. In real-world scenarios, components such as cables, connectors, and adapters can introduce losses that reduce the overall signal strength, further complicating the maintenance of a -100 dB transmission level. Additionally, environmental factors like temperature, humidity, and electromagnetic interference can impact the performance of the antenna and the overall system, resulting in deviations from the theoretical transmission level. Manufacturing tolerances from the fabrication process can also introduce discrepancies in the antenna geometry or material properties, leading to differences between the theoretical and experimental performance.

While it is important to acknowledge the potential challenges in achieving a -100 dB level in practical experiments, the ACA offers several advantages such as reduced interference between adjacent antennas, improved signal-to-noise ratio, minimal risk of electromagnetic interference with other medical equipment, and reduced exposure to potentially harmful electromagnetic radiation for patients. These attributes are particularly important for imaging systems where multiple antennas are used in close proximity and in medical applications that require high signal quality and reliable communication while ensuring patient safety.

Moreover, Fig. 5.8(a) suggests that, with the exception of the transmission levels received at Receiver 5 and Receiver 9, which were below -100 dB, the transmission levels at other receivers were above -95 dB in the ACA array. Notably, the transmission levels at Receivers 2, 3, 6, 7, 8, 11, and 12 were above -80 dB. The transmission levels at most ports may be more than adequate for achieving satisfactory performance.

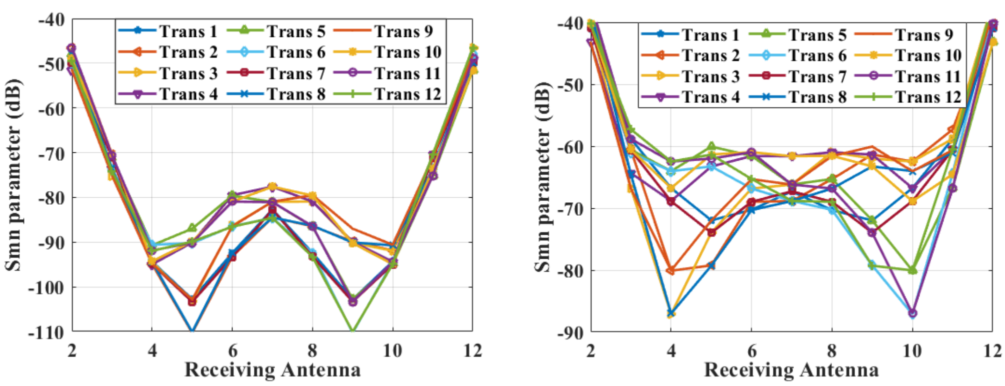

(a) (b)

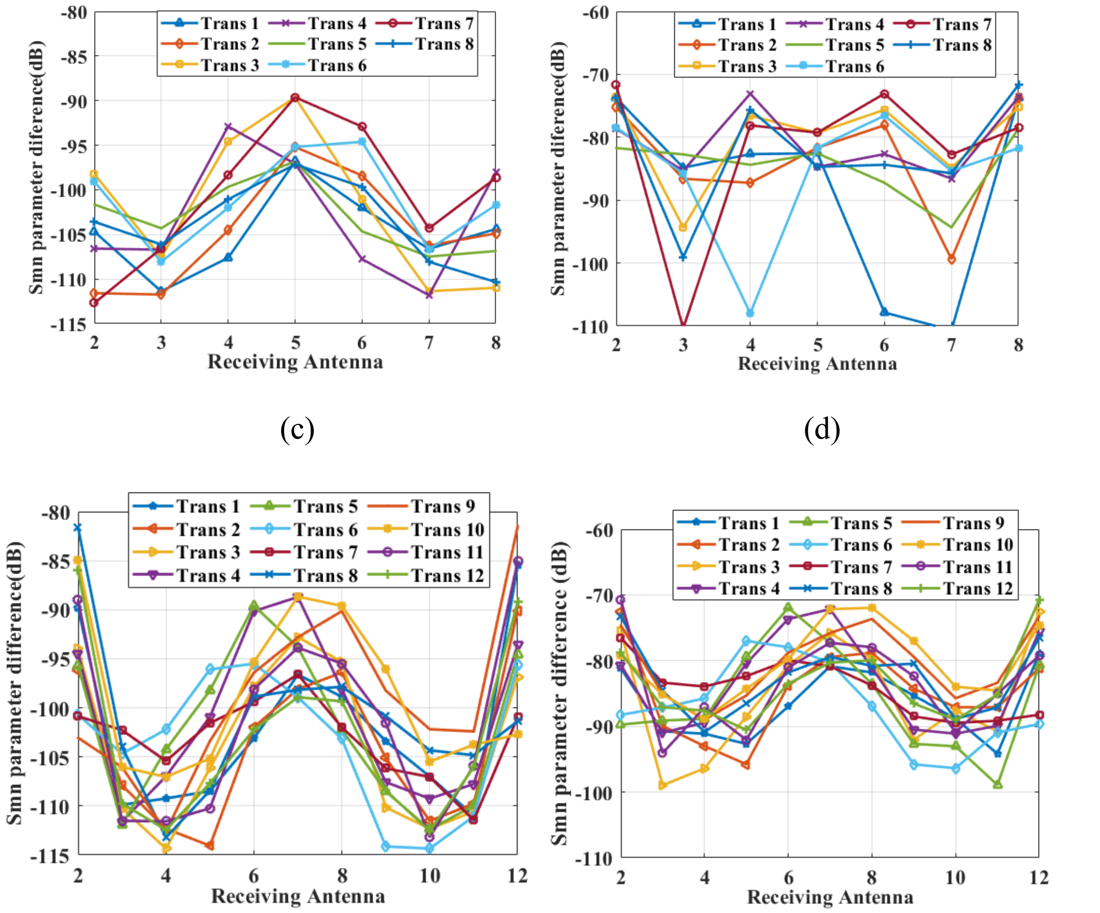

(c) (d)

(e) (f)

Figure 5.8 Received signal strength (in dB) for the ECA and ACA arrays at 1 GHz: (a) no-target case scanned with 12-ACA scanner; (b) no-target case scanned with 12-ECA scanner; (c) received signal strength difference between no-target case and with-target case (Target A at Location III) scanned with 8-ACA scanner (d) difference with 8-ECA scanner (e) difference with 12-ACA scanner; (f) difference with 12-ECA scanner.

To evaluate the scanner's detection ability, we repeated the same received signal strength calculations in the presence of Target A in Location III of Table 5.2, shown in Fig. 5.7(h). We then calculated and plotted the signal difference between the target and no-target cases (in dB) for 8-ACA, 8-ECA, 12-ACA and 12-ECA scanner in Fig. 5.8(c)–(f). respectively. The plots show that the target's response was 20 dB below the total signal and was above the -100 dB threshold for only some of the transmitter-receiver pairs. The number of these pairs was lower for the ACA array, which recorded lower signal levels. However, the signal plots for the different receivers were better correlated for the ACA arrays. This is particularly evident when comparing the plots in Fig. 5.8 (c) and (d). While the received signals for certain transmitter-receiver (transceiver) combinations were quite weak, our MWT system could still detect and estimate dielectric targets by using those transceiver combinations that led to signal levels above the VNA's noise level.

5.7 Reconstruction with DBIM-TwIST

A microwave tomography method based on the DBIM-TwIST algorithm was proposed in our previous study. The non-linear inverse scattering problem was approximated by an inadequately determined set of linear equations using the distorted Born iterative method (DBIM). A nonlinear integral equation, which serves as the foundation of the DBIM, can be expressed as [7], in its 2-D scalar form.

$$E_s(r_n, r_m) = E(r_n, r_m) - E_b(r_n, r_m) = \omega^2\mu \int_V G_b(r_n, r)\, E(r, r_m)(\varepsilon(r) - \varepsilon_b(r))dr$$

, where E, E_s, and E_b stand for total, scattered and background fields, respectively, and r_n and r_m stand for the locations of the transmitting and receiving antennae. The total field was measured at each antenna but was unknown inside the total region V. G_b was the background medium's Green's function inside the integral. For point source condition, the Green's function can be calculated from the electric field as $G_b(r_n, r) = \frac{j}{\omega\mu_0 J} E_b(r, r_n)$. It should be noted that the scalar integral equation mentioned above assumes two-dimensional (2D) transverse magnetic (TM) propagation and serves only as an approximation for the three-dimensional (3D) inverse problem at hand. Although there is a loss of information due to this approximation, 2D models can still generate images of satisfactory quality in numerous microwave imaging problems encountered in medical applications.

In every discrete Born iterative method (DBIM) iteration i, the integral equation can be discretized for each transmitter-receiver (TR) pair as:

$$E_s(r_n, r_m) = j\omega\varepsilon_0 \sum (\varepsilon(r) - \varepsilon_b(r))\, E_b(r_n, r) E_b(r, r_m)$$

, leading to an ill-posed linear system as:

$$\boldsymbol{A}\delta_\varepsilon = b$$

, where A is an M × N matrix (M ≪ N), consisting of M transmit-receive pairs and N voxels of the reconstruction region V, while b is an M × 1 vector of scattered fields. The matrix A is computed at each DBIM iteration using the forward solver, which yields E_b for a known background ε_b. The background field is employed to construct the linear system mentioned above, which is then solved by an inverse solver. Subsequently, the background profile is updated using $\varepsilon_b^{i+1}(r) = \varepsilon_b^{i+1}(r) + \delta_\varepsilon(r)$, and the DBIM proceeds to the next iteration i + 1.

The forward solver of our DBIM-TwIST algorithm employs the finite difference time domain (FDTD) method. The FDTD method simulates the electromagnetic (EM) wave propagation of the direct, "forward" problem based on Maxwell's equations. As previously mentioned, this work focuses on reconstructing 2D geometries using only 2D transverse magnetic (TM) waves. Additionally, our FDTD implementation uses a single-pole Debye model to represent frequency-dependent materials such as brain tissues, expressed as $\varepsilon = \varepsilon_\infty + \frac{\Delta\varepsilon}{1+j\omega\tau} + \frac{\sigma}{j\omega\varepsilon_o}$.

We utilise the two-step iterative shrinkage/thresholding (TwIST) algorithm as the solver for the ill-posed linear inverse problem at each DBIM iteration. Thresholding algorithms address the ill-conditioned linear system A x = b by finding a solution x that minimizes the least squares error function $F(x) = 1/2\, ||Ax - b||^2 + \lambda||x||_1$, with a regularization term λ||x||₁ to stabilize the solution by limiting its l1-norm. The general structure of the TwIST algorithm for solving this minimization problem is provided by [193]:

$$x_{t+1} = (1 - \alpha)x_{t-1} + (\alpha - \beta)x_t + \beta C_\lambda(x_t)$$

$$C_\lambda(x) = \Psi\lambda(x + A^{\mathrm{T}}(y - Ax))$$

The TwIST algorithm parameters are calculated as $\kappa = \xi_1/\xi_m$, $\rho = (1 - \sqrt{\kappa})/(1 + \sqrt{\kappa}))$, $\alpha = \rho^2 + 1$, and $\beta = 2\alpha/(\xi_1 + \xi_m)$, where ξ_1 and ξ_m are the smallest and largest eigenvalues of $A^{\mathrm{T}}A$, respectively. The shrinkage/thresholding operation is a soft-thresholding function: $\Psi_\lambda(x) = sign(x)\, max\{0, |x| - \lambda\}$. At each TwIST step, the new solution is updated based on the two previous solutions and the soft-thresholding function.

The stopping criterion for the TwIST algorithm can be set based on a tolerance value, which is the normalized difference between the previous and current values of F(x), defined as $tol = (F(x_{k+1}) - F(x_k))/F(x_k)$. The TwIST algorithm terminates when tol is smaller than a preset value, typically between 10^{-4} and 10^{-1}. This early termination of the iterative algorithm acts as an additional regularizer, similar to the Tikhonov approach[194]. The l_1-problem can be further regularized using the Pareto curve method, which provides the optimal trade-off between the residual error $||Ax - b||^2$ and the norm of the solution $||x||_1$ (similar to the L-curve method for l_2-problems)[195]. To reduce computational cost, a practical approach for selecting λ is based on the form $\lambda = \delta||A^{T}b||_{\infty}$, where δ is a factor with $0 < \delta < 1$ [195].

5.8 Reconstruction Images of ECA vs ACA

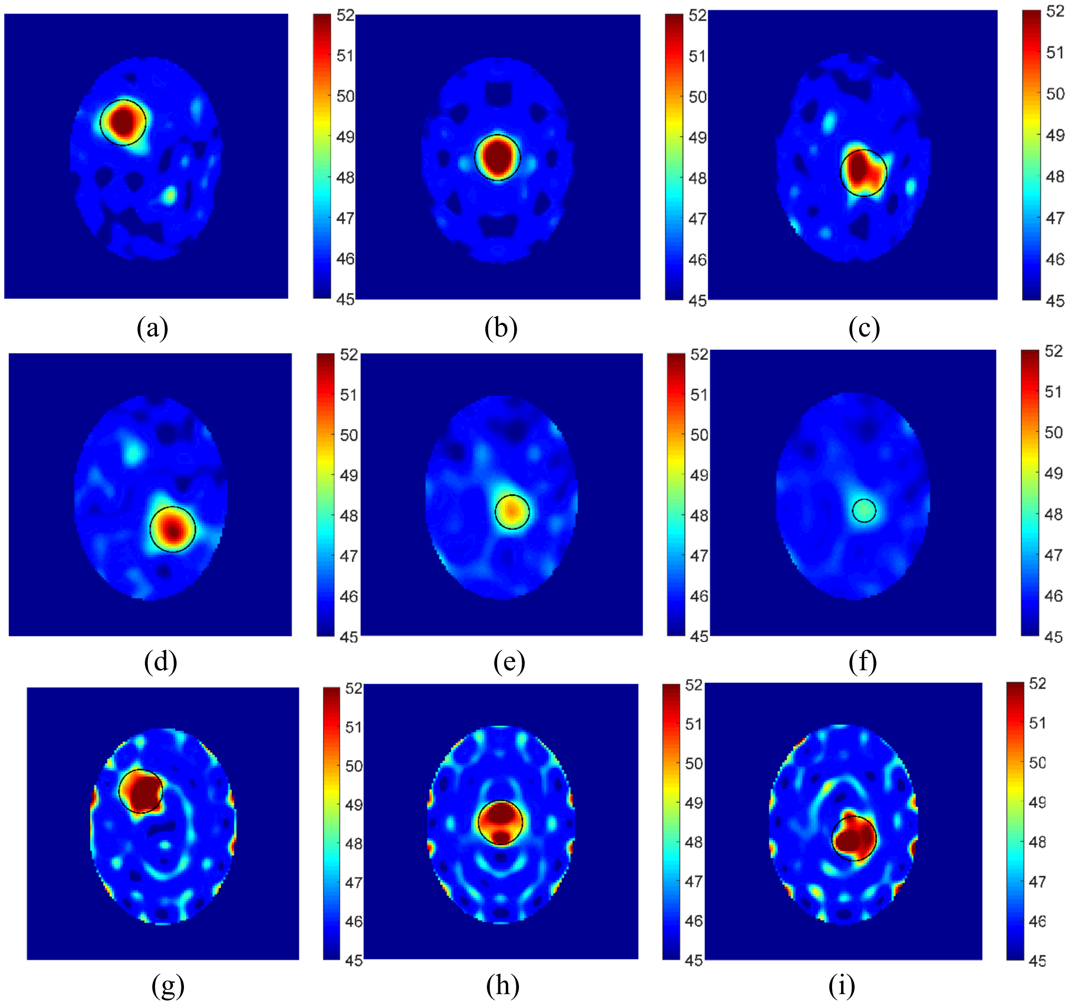

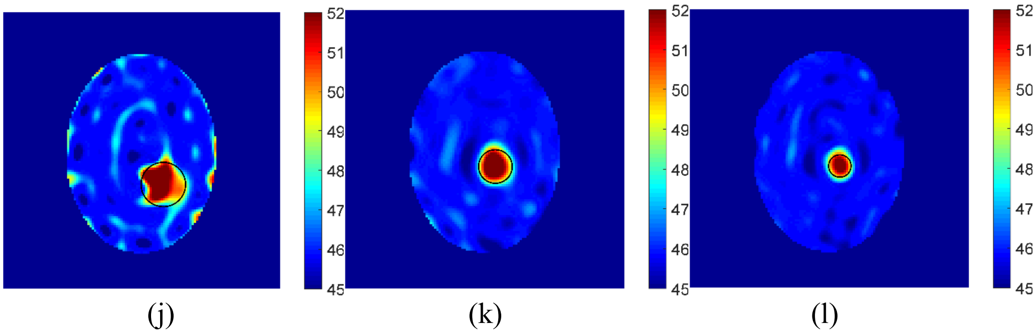

Figure 5.9 Reconstructed dielectric constant of the images brain area at 1.0 GHz using ECA array: (a)-(d)Target A at Location I to IV using 8-ECA array; (e)-(f) Target B and C at Location III using 8-ECA array; (g)-(i) Target A at Location I to IV using 12-ECA array; (j)-(l) Target B and C at Location III using 12-ECA array.

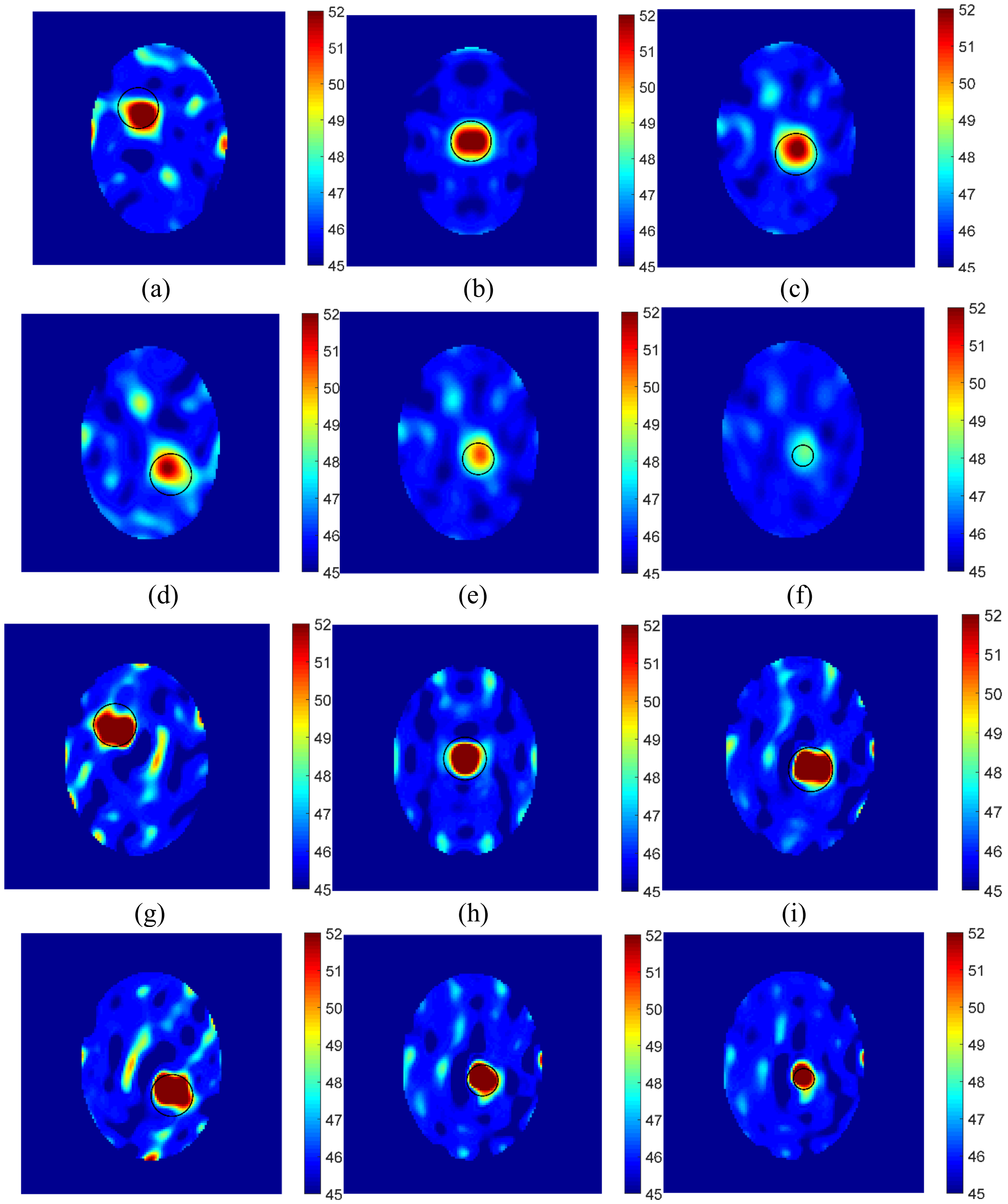

(j) (k) (l)

Figure 5.10 Reconstructed dielectric constant of the images brain area at 1.0 GHz using ACA array: (a)-(d)Target A at Location I to IV using 8-ACA array; (e)-(f) Target B and C at Location III using 8-ACA array; (g) - (i) Target A at Location I to IV using 12-ACA array; (j)-(l) Target B and C at Location III using 12-ACA array.

To better understand how these differences in acquired signals can translate into detection and localization performance, we reconstructed the dielectric properties of head model utilising our formerly developed DBIM-TwIST algorithm. Fig. 5.9 and Fig. 5.10 show the reconstructed dielectric constant of the images brain area for the four different array types, which is calculated from the estimated Debye parameters at 1.0 GHz.

To qualitatively compare the reconstruction performance of each array in various cases, we define a relative reconstruction error of target area as

$$\text{Relative Error}=\frac{|\varepsilon^{t}_{\infty original}-\varepsilon^{t}_{\infty original}|^2}{|\varepsilon^{t}_{\infty original}|^2}$$

, where t is the iteration number and ε_∞ denotes one of the reconstructed Debye parameters.

As we cannot know the true ε_∞ in a realistic application, we must also define a Residual error as:

$$\text{Residual} = |\mathrm{M}_t^E - \mathrm{M}_t^S|^2$$

, where M_t^E and $\mathrm{M}_t^S|^2$ are matrices of the “experimental” and “model” data at the t_{th} iteration. In this paper, the total iteration number of this study is 60, so we take the 60_{th} iteration results for all cases. We note that we selected this fixed number of 60 iterations for all cases as a practical way to ensure convergence for the DBIM for these imaging scenarios without having to run an excessive number of iterations.

In practice, we could also use a more rigorous convergence criterion by requiring, for example, that the residual error between two successive iterations does not drop for less than a predetermined value. While the residual error will always be available, the computed relative reconstruction error is only available if the ground truth is known and is therefore only useful as a performance metric. These two metrics are correlated for well-behaved inverse problems, but their correlation may be challenged for non-linear, ill-posed problems such as those typically encountered in MWT. The relative error and residual are listed in Table 5.3.

5.9 Optimal Antenna Number in Array

We marked the original shape, dimension and location of the target in all reconstruction images so that it would be convenient for readers to compare the reconstructed target with the original target. These images show the clear detection of the blood target by the 8- and 12- antenna arrays. The artefacts outside the target area in these images were due to modelling errors between the inverse model and the CST solver producing the numerical "measured" data. Amongst these errors, mutual coupling between antennas can be a dominant factor. By varying the number of antennas in the CST simulations, we assessed the mutual coupling effect on the reconstructed images. The reconstruction plots, the relative error of blood target area and the residual listed in Table 5.3 for the various cases helped us assess and compare the effectiveness of each of the four arrays.

Compared with 8-antenna arrays, 12-antenna arrays showed reduced relative error and residual of the reconstructed images. Switching from an ECA array to an ACA array also had a positive impact due to the ACA's nature of low return loss, low VSWR and high directivity in our desired frequency range. Benefiting from better impedance matching and less spurious radiation, the relative reconstruction and residual errors for the ACA-based reconstructed images were, in most cases, lower than those of the ECA-based images. The relative error and residual of the 12-ACA array were much lower than those of the other three arrays, and the residual was nearly half that of the 8-ACA array, which was the array with the second-best performance overall. From an image quality point of view, the plots suggest that the locations of the targets detected with 12-antenna arrays are better matched with the marked circles. The plots also indicate that the reconstructed targets with ACA arrays were more consistent with their true dimensions and locations.

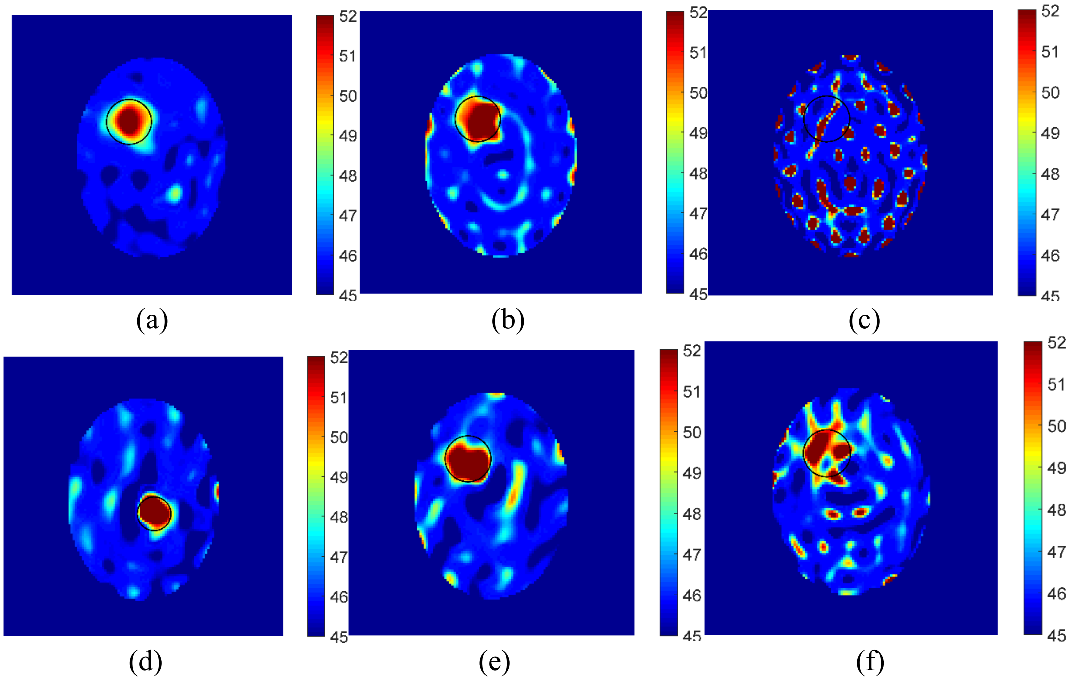

Figure 5.11 Reconstructed dielectric constant of the brain area images at 1.0 GHz using 8, 12, 16-element array: (a),(d) Target A at Location I using 8-ECA, 8-ACA array; (b),(e) Target A at Location I using 12-ECA, 12-ACA array; (c),(f) Target A at Location B.

To investigate the trade-off between mutual coupling and sufficient data for our MWT algorithms, we also compared the imaging performance of 8, 12 and 16-element antenna arrays for Target A at Location I. Moving from a 12-element to a 16-element antenna array, the imaging capability of both the ACA and the ECA scanner was degraded overall. In particular, the 16-ECA array failed to detect the target and led to image artefacts only, while the 16-ACA array can detect the target, but with increased image artifacts. The reconstruction relative errors of the 16-antenna arrays are included in Table 5.3 and are much higher than those of 12-antenna (or even the 8-antenna) arrays. This suggests that mutual antenna coupling must be taken into account in studies that attempt to optimise the number of antenna elements in MWT systems. Moreover, the much stronger degradation observed for the ECA elements confirms that the ACA design significantly reduces mutual coupling by minimising spurious radiation.

5.10 Imaging Quality Assessment

We presented a comparison of two antenna designs that are based on the same radiating patch but differ in their feeding method. The purpose of this comparison was to assess the impact of reducing spurious radiation by using a more efficient feeding method based on aperture coupling. The motivation behind this comparison lies in the well-known observation that unwanted signals can have a negative impact on microwave tomography algorithms.

Table 5.3 Relative error and residual of reconstruction at 1.0 GHz

Location of Target A	Location 1		Location II		Location III		Location IV	
	Error	Resi.	Error	Resi.	Error	Resi.	Error	Resi.
8-ECA array	0.1794	0.0415	0.0349	0.1754	0.1813	0.0357	0.1867	0.0254
12-ECA array	0.1568	0.0254	0.1609	0.0219	0.1649	0.0225	0.1637	0.0197
8-ACA array	0.1846	0.0260	0.1708	0.0179	0.1884	0.0153	0.1932	0.0143
12-ACA array	0.1486	0.0075	0.1701	0.0059	0.1555	0.0066	0.1533	0.0068

Target Size at Location III	Target Size A		Target Size B		Target Size C	
	Error	Resi.	Error	Resi.	Error	Resi.
8-ECA array	0.1813	0.0357	0.2286	0.0164	0.2395	0.0092
12-ECA array	0.1649	0.0225	0.2209	0.0075	0.2404	0.0063
8-ACA array	0.1884	0.0153	0.2270	0.0109	0.2363	0.0068
12-ACA array	0.1555	0.0066	0.2138	0.0056	0.2288	0.0042

Antenna Quantity	8-antenna Array		12-antenna Array		16-antenna Array	
	Error	Resi.	Error	Resi.	Error	Resi.
Error	0.1794	0.1846	0.1568	0.1486	0.3509	0.2644
Residual	0.0415	0.0260	0.0254	0.0075	1.4632	0.0066

To study this issue, we compared the stand-alone performance of the two antennas to confirm that the ACA design could lead to a more directive antenna. This could result in focusing energy more efficiently in the near field and hence reducing coupling of nearby antenna elements. We analysed the imaging quality of both antennas in reconstructed images to confirm that the relative error and residual of non-spurious ACA were mostly lower than those of ECA. In particular, the residual of ECA was 50 % smaller than that of ACA, which was the result of spurious radiation of ECA, causing greater inconsistence between the actual signal source size and the point source in the finite-difference time-domain (FDTD) modelling method. In addition, we investigated the mutual coupling effect and optimal antenna number by comparing the performance of 8, 12 and 16-elelment antenna array.

The quality of reconstructed images in microwave brain imaging is a critical factor for accurate diagnostics and treatment. In this study, we assess the imaging quality of reconstructed images using a combination of relative error and residual algorithms. Two antennas, ECA and ACA, are compared for their performance in microwave brain imaging. Both ECA and ACA have demonstrated good performance in microwave brain imaging; however, the ACA outperforms the ECA in terms of error and residual values. The error and residual values of ACA are less pronounced compared to those of ECA, indicating that ACA yields more accurate and reliable reconstructed images. This superior performance of ACA can be attributed to its adaptive nature, which allows it to adjust to the imaging environment more efficiently.

Additionally, we investigated the effect of optimal antenna number in array on the imaging quality. We compared three different antenna array setups: 8-element, 12-element, and 16-element arrays. Our results indicate that the 12-element antenna array provides better imaging quality than the other configurations for both ECA and ACA. The 12-element array exhibits lower error and smaller residual values, leading to enhanced precision and more accurate image reconstruction. The superior imaging quality obtained with the 12-element antenna array can be attributed to its optimal balance between spatial resolution and signal-to-noise ratio. This configuration allows for better signal coverage and improved imaging performance without causing excessive complexity in the system or sacrificing the reliability of the imaging process.

In conclusion, our research highlights the good performance of the proposed antenna, antenna array, and array scanner in microwave brain imaging. The Adaptive Capacitive Algorithm, combined with a 12-element antenna array, provides enhanced imaging quality, with lower error and smaller residual values. These findings have significant implications for the future development of microwave brain imaging systems, as they can guide the design and optimisation of antennas, antenna arrays, and array scanners to achieve the best possible imaging performance.

Chapter 6 Study of The Experimental MWI System

6.1 Experimental Phantom Preparation

As the aim of this work is to validate DBIM-TwIST in more realistic, yet simplified cases for brain stroke detection and classification, we constructed simple phantoms based on the materials and processes proposed in [191], [196]. Using different gelatine–oil concentrations compared to those for breast tissues, we fabricated tissue-mimicking materials with specific dielectric properties that mimic average brain tissue, cerebrospinal fluid (CSF), blood and ischaemia. First, a water–gelatine mixture was prepared and mixed at 70°, until the gelatine particles were fully dissolved in water and the mixture was transparent. Propanol was added to address the creation of air bubbles on the surface. Once heated to 70°C, we added a 50% kerosene–safflower oil solution into the water–gelatine mixture and stirred with Vertex Genie 2, as shown in Fig.6.1 (a), at the same temperature, until the emulsion had an opaque white colour, and the oil particles were fully dissolved. We continued stirring the mixture until the temperature dropped to 70°C, when we added the surfactant. Finally, we poured the prepared mixture into the mould when it reached 70°C, and let it set overnight before we conducted any measurements.

(a) (b)

Figure 6.1 Preparation of phantom: (a)Vortex Genie 2 used for stirring; (b)brain phantom prepared in the acrylonitrile butadiene styrene mould.

After preparation, the phantoms were placed in elliptical plastic acrylonitrile butadiene styrene (ABS) moulds that aimed to mimic the brain's shape and multi-layer structure, as shown in Fig. 6.1 (b). We first poured the CSF phantom into the outer layer with a thickness of 5 mm. After this was solidified, we extracted the inner mould and filled the remaining cavity with the brain phantom. For a one-layer model without CSF, we simply extracted the inner mould and poured the phantom directly into the outer mould. We used an additional cylindrical mould to create a hole (diameter = 30 mm) in the phantom, which could be filled with the phantom mimicking either blood or ischaemia, imitating the two cases of brain stroke termed 'h-stroke' for haemorrhagic and 'i-stroke' for ischaemic, respectively.

6.2 Calibration

Environmental noise, thermal noise, antenna mutual coupling, and machine noise are typically present in the experimental data assessed by hardware (such as multi-port vector network analysers). Denoising techniques can be used for white noise sources either after measurement or during the reconstruction process. However, for other types of inaccuracy, such as antenna coupling and interference, we needed to use a calibration method in our imaging algorithm, which used a streamlined 2-D solver with point sources acting as antennas to lessen the impact[197]. Applying the difference between measurements in the homogeneous medium and the inhomogeneous medium (with target) was a straightforward method based on measurement data (without target). The distinction is displayed as:

$$\triangle \Gamma_{dB} = |E_{inhomo}|_{dB} - |E_{homo}|_{dB}$$

$$\triangle \Phi = \Phi(E_{inhomo}) - \Phi(E_{homo})$$

The calibrated data can then be obtained as:

$$\Gamma_{E_M} = |E_{homo}|_{dB} + \triangle \Gamma_{dB}$$

$$\Phi_{E_M} = \Phi(E_{inhomo}) + \triangle \Phi$$

, where Γ is the frequency domain magnitude of the received signals and Φ represents the corresponding phase. The FDTD forward solver generated E_{homo} using the assumed background medium. To account for frequency dispersion using the Debye model, the corresponding Debye parameters of the background medium were obtained by applying the curved fitting approach to data from the experimental media measurement. Following that, the reconstruction algorithm processed the calibrated data Γ_{E_M} and Φ_{E_M} as input.

6.3 Vector Network Analyser

The fundamental principle of a VNA is to measure the amplitude and phase of both the incident and reflected waves at the various ports of the devices under test. The general design of a VNA is to stimulate an RF network at a given port with a stepped or swept continuous wave and measure the travelling waves at the stimulus port and all other ports of the network. The VNA is primarily used to determine the S-parameter for passive devices by solving a set of equations after measuring the ratios of wave quantities while exciting the device at its various ports. For RF and microwave components, the S-parameters provide complete linear insight into their behaviour. Thus, S-parameters are typically used to describe how the device being tested behaves and how it interacts with other devices. Over time, besides the S-parameter measurement, VNAs have also been used for the characterisation of dielectric properties of materials as the VNA can measure the reflection factor as a function of frequency and the results can be transformed into a time domain.

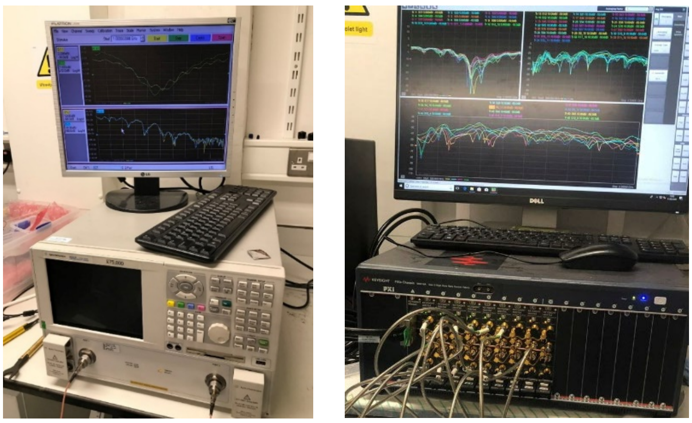

(a) (b)

Figure 6.2 Lab experimental setup: (a) two-port VNA; (b) fourteen-port Keysight m9370a VNA.

A VNA can be decomposed into different element blocks. First, the VNA source provides the stimulus used to characterise the response of a device under test. The signal from the source is typically a sine tone for RF and microwave applications. Such an ideal signal can be expressed as $V(t) = Asin(2\pi ft)$, where A is nominal amplitude and f is nominal frequency. In practical experiments, the signals are disturbed by noises and are expressed as $V(t) = [A + a(t)] \sin[2\pi ft + \Delta\varphi(t)]$, where $a(t)$ is random amplitude variation, referred to as 'amplitude noise', and $\Delta\varphi(t)$ represents phase variation of signals referred to as phase noise. The effect of $a(t)$ the amplitude noise term is to add instability to amplitude at frequency f_0.The $\Delta\varphi(t)$ phase noise term broadens the signal spectrum. The phase noise of the source contributes to the noise measured at the output, which cannot be neglected entirely.

In our previous studies[57], [191], [192], [198], a two-port PNA series VNA, as shown in Fig. 6.2(a), was applied. In the radar imaging system, a programmable motor that creates desirable motion steps was placed above the static base of the system to carry out a complete $360°$ sweep with a step of $22.5°$ for each position of the antenna. After examining the results with the rotary system for data acquisition, we understood the implications of tiny errors on the overall performance of the system, particularly on data collection and the inversion algorithm. We observed that the data lacked symmetry due to inaccurate positioning of the antennas and imaging chamber, along with other errors. Therefore, we designed our data acquisition hardware prototype with a multi-port VNA to reduce the sources of errors we observed in our previous study. In the tomographic imaging system, we used 8 antennas immersed in coupling liquid to detect with a 14-port KEYSIGHT M9370A VNA, as depicted in Fig. 6.2(b).

6.4 Experimental Validation

We used the proposed antenna with our microwave imaging prototype to investigate whether wide frequency operation results in improvement of the reconstruction quality. The prototype comprises an 8-antenna array, an imaging chamber, and coupling liquid as shown in Fig. 6.3(b). The imaging chamber is a cylinder with a diameter of 300 mm, and the coupling liquid is a mixture of 90% glycerine and 10% water. The system was tested with a head phantom with average brain tissue and a cylindrical blood target with a diameter of 30mm and a height of 20mm, placed at (-30, 30) with respect to the centre of the head.

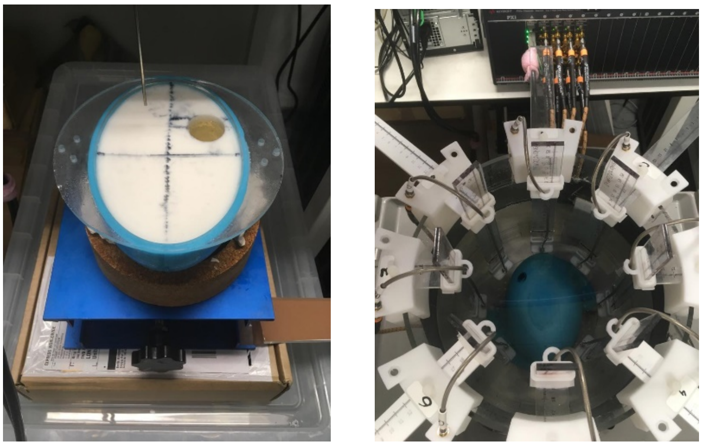

(a) (b)

Figure 6.3 Experimental MWT setup to evaluate performance with the proposed spear-shaped design: (a) The imaging system connected to Keysight's multi-port VNA; (b) a constructed head phantom filled with an average brain tissue mimicking phantom.

(a)

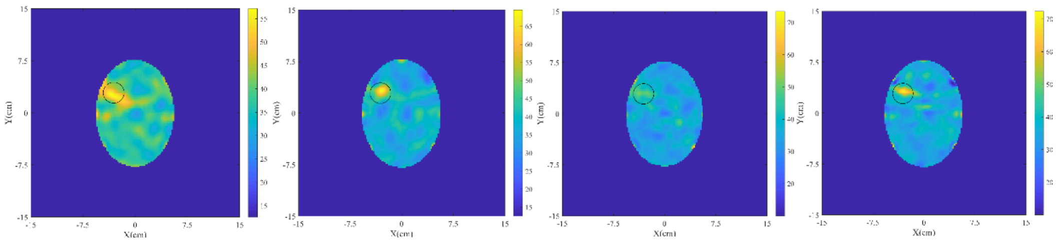

(b) (c) (d) (e)

Figure 6.4 Comparison of phantom reconstructions using two different PRMA designs across multiple frequencies: (a) Photos of the triangular-shaped and spear-shaped patch antennas; (b)-(e) Dielectric constant reconstructions using the TwIST-DBIM algorithm.

While this simulation-based analysis is very useful for studying limitations in the antenna array design and their impact on imaging performance, the findings from this analysis require experimental validation. To this end, we measured and validated the ECA's stand-alone and in-array experimental performance in [70]. We used our previously reported DBIM-TwIST algorithm to reconstruct images from the system shown in Fig. 6.3(b). To evaluate the performance of our proposed antenna, we compared its resulting reconstructions with those from our previously deployed triangular-shaped antenna, which did not optimally match above 1.5 GHz. Examples of reconstructions at 1.5 GHz and 2.2 GHz are presented in Fig. 6.4 for triangular-shaped patch monopole and spear-shaped patch monopole antenna arrays. These results show a clear improvement in image quality for the spear-shaped antenna, which experimentally confirms that improving the bandwidth of the antenna translates directly to benefits in reconstruction quality.

We have not been able to perform similar experiments with the ACA, however, as the manufacture of this more recently designed antenna has not been possible due to supply issues caused by the COVID-19 crisis. We hope that these issues will be resolved soon so that our future work can include measurements of the manufactured ACA stand-alone performance, as well as an experimental comparison of results from the ACA and ECA arrays, similar to the simulations presented in this paper.

This experimental comparison will also be required to investigate other important issues that can affect the system's imaging performance such as the selection of the best reconstruction frequencies based on the measured data, and the influence of factors such as the impact of cables or insertion loss in port-switching networks. Our previous experimental validation studies have shown encouraging results that these issues can be addressed successfully via careful calibration and selection of the imaging algorithm's parameters.

Chapter 7 Conclusion and Future Work

7.1 Conclusion

The work in this thesis represents a first step in King's College London's construction of a microwave tomography system. The main issues in microwave tomography, namely penetration depth and picture resolution, were addressed. We successfully created and put into use a basic hardware prototype for microwave tomography that is applicable to medical imaging.

We conducted a comprehensive literature review, examining the dimensions, frequency ranges, and other advantages and disadvantages of various antenna types. Based on this review, we designed several antennas, including Vivaldi antennas, microstrip patch antennas, dielectric resonator antennas, printed monopole antenna, probe-fed coaxial antenna, aperture-coupled fed antenna, etc. We encountered challenges with certain antenna types, such as larger-than-desired dimensions or operation at higher frequencies than anticipated. However, these challenges ultimately led us to identify the most suitable antenna designs for our microwave imaging system. Through our research, we found that printed monopole antennas and aperture-coupled fed microstrip antennas emerged as the most suitable choices for our microwave imaging system. The printed monopole antennas offer a compact size, low cost, easy fabrication, wideband operation, and easy integration with other circuitries. The aperture-coupled fed microstrip antennas provide low spurious radiation, directive radiation, increased substrate space for antenna elements and feed lines, and theoretically zero cross-polarisation.

We also proposed a variety of antenna design techniques for tomography. Our goal was to create a small, reliable antenna that would work for microwave tomography, so we introduced a series of techniques as a guide to design and optimise the antenna. We investigated equivalent circuit approximation analytical techniques. Adopting this technique, the antenna could be modelled to the equivalent capacitances and inductances in series or parallel connection. The frequency characteristics could be predicted according to the concept of the LC resonant circuit. We then studied the conjugate impedance matching method. Conjugate matching allows for maximum possible antenna efficiency, which enhances antenna performance at a particular frequency. We presented the two-port network model and scattering parameter formulas as guides for designing our antenna. With our proposed formula, the magnitude scale of s_{21} and s_{11} could be enhanced. We also applied a power transfer efficiency analysis technique to analyse the voltage gain s_{21} between the transmitter and the receiver.

The monopole antenna that we propose is a miniaturised rectangular shape and has desirable performance for UWB antennas. The goal is to achieve increased bandwidth. The reduction in size is also a consideration in the design of this antenna, which would be more easily integrated into the system and reduce clutter. We designed various regular-shaped patch monopole antennas, including hexagonal, square, circular and triangular patch antennas. We followed Ray's equation to estimate the performance of the antenna, which we regarded as a crucial antenna optimisation criterion. This formula allows for the modification of antenna performance by altering the dimensions of various antenna components. These regular-shaped patch monopole antennas perform well in terms of the reflection coefficient and antenna dimension. However, it needs to be modified to function with our microwave imaging system. We then designed our initial prototype antenna, which is a spear-shaped patch antenna. With dimensions of 25.0 mm × 16.0 mm × 1.6 mm, it is small. It operates between 1.2 GHz and over 4.0 GHz with a resonant frequency of 2.3 GHz. We then optimised the antenna to a smaller size of 21.0 mm × 14.0 mm × 1.7 mm with a wider operation bandwidth from 0.7 GHz to over 4.0 GHz and with much deeper resonant S_{11} -30 dB at 1.7 GHz. Monopole antennas have a straightforward construction, which leaves little possibility for conjugate impedance match and leakage radiation optimisation. The idea of aperture-coupled feeding was proposed. The dimension of the optimised aperture-coupled antenna is 34.42 mm × 18.25 mm × 12.00 mm. We examined the stand-alone performance of the two antennas and found that the ACA design could result in a more directional antenna. As a result, energy may be focused more effectively in the near field, reducing the coupling of nearby antenna elements.

We investigated the effectiveness of our arrayed antennas. We began our research on 8-antenna arrays operating in a glycerine-filled tank. The effectiveness of arrays with and without highly scattering target objects was investigated experimentally and numerically in the setup. We modelled our straightforward tomography system with 8 antennas that operate in a cylinder filled with glycerine–water media in the 3D electromagnetic CST Microwave Studio. To create the most accurate simulation model for the system under study, we produced phantoms (matching medium) and measured them with a probe kit using a Keysight M9019 PLIE VNA. We then imported the data into the CST Microwave Studio to model the phantoms numerically.

We studied the layout and optimal total antenna number in an imaging scanner. To evaluate the imaging quality of various head scanners, we submerged a simplified head model (SAM) in a glycerine–water solution. We suggested two types of scanners: a headband scanner and a helmet scanner. In the headband scanner, 8, 12 or 16 confocal antennas encircle the head. The purpose of the helmet scanner, which has three rows of antennas (with the top row having four antennas, the middle row eight antennas and the bottom row twelve antennas), is to gather more data for the resolution of an ill-posed microwave imaging algorithm. The transmission coefficient S_{n1} of both scanners at 0.5 GHz, 1.0 GHz, and 1.5 GHz is over -100 dB, and the S_{n1} magnitude difference between with and without the target is above -100 dB. The simulated results were above the noise floor of the VNA -100 dB, allowing both scanners to be used in experiments.

We measured the impact of this need on a 20 dB signal loss recorded by the MWT array to quantify the trade-off in achieving the ACA design, which requires a significantly thicker (and thus lossier) substrate. We examined the imaging quality of both antennas in the reconstructed images to confirm that the relative error and residual of the non-spurious ACA are typically lower than those of the ECA. In particular, the residual of the ECA is 50% smaller than that of the ACA, which is the result of spurious radiation of the ECA, causing a greater discrepancy between the actual signal source size and the point source in the FDTD modelling method. By evaluating the performance of an 8-, 12- and 16-element antenna array, we also looked into the impact of mutual coupling and the ideal number of antennas.

7.2 Future Work

Moving forward, the fabrication and experimental validation of the ACA are essential steps to assess its practical performance. Developing a prototype that accurately reflects the design parameters derived from theoretical analysis will enable us to compare the antenna's actual behaviour in real-world scenarios with theoretical expectations. Evaluating radiation patterns, impedance matching, and overall efficiency will identify any discrepancies or areas for improvement. Further investigations into different fabrication techniques and materials could lead to enhancements in the ACA's performance, reliability, and long-term stability. Ultimately, these steps are crucial for ensuring the antenna's suitability for use in microwave imaging systems and advancing the field of microwave tomography.

In addition, temperature fluctuations, humidity, and electromagnetic interference can significantly impact the antenna's efficiency, radiation patterns, and impedance matching. Rigorous testing and experimentation in controlled environments simulating various operating conditions are necessary to ensure the antenna's optimal performance under different circumstances. These investigations will provide valuable insight into the antenna's robustness and reliability when exposed to real-world challenges and contribute to the development of a more suitable antenna for microwave imaging systems.

In our study, the head model was simplified as a two-layer structure, but in reality, the human brain comprises multiple complex layers. To improve the accuracy and applicability of our microwave imaging system, it is essential to incorporate more layers into the head model. By simulating the intricate structure of the brain, we can better understand how microwave signals interact with various brain tissues and improve the imaging system's ability to detect abnormalities or changes within the brain. Future work should focus on refining the head model by adding more layers and accounting for the diverse properties of different brain tissues. This would involve a comprehensive study of the dielectric properties and electromagnetic behaviour of various brain tissue types at different frequencies. The improved head model would enable more accurate simulations and help optimize the antenna designs and signal processing techniques for better performance in practical applications. Additionally, incorporating a more realistic head model would also enable a better understanding of potential challenges and limitations of the microwave imaging system. It would provide valuable insights into the imaging resolution, penetration depth, and sensitivity to different brain structures, leading to the development of more advanced and reliable microwave tomography systems for medical imaging purposes.

Future work should also address various challenges and factors influencing the antenna’s performance. Issues such as machining inaccuracies can affect the antenna’s geometry or material properties, leading to deviations in performance. Conducting a thorough investigation of fabrication techniques and their impact on performance is essential for overcoming these challenges. Additionally, understanding the effects of environmental factors, such as temperature fluctuations, on the imaging system's performance will be crucial in designing robust and reliable microwave imaging systems for various applications.

Reference

[1] P. Kosmas and L. Crocco, “Introduction to Special Issue on ‘Electromagnetic Technologies for Medical Diagnostics: Fundamental Issues, Clinical Applications and Perspectives,’” *Diagnostics*, vol. 9, no. 1, p. 19, Feb. 2019, doi: 10.3390/diagnostics9010019.

[2] A. Abbosh, “Microwave systems for head imaging: Challenges and recent developments,” *2013 IEEE MTT- Int. Microw. Workshop Ser. RF Wirel. Technol. Biomed. Healthc. Appl. IMWS-BIO 2013 - Proc.*, pp. 18–20, 2013, doi: 10.1109/IMWS-BIO.2013.6756184.

[3] M. Persson *et al.*, “Microwave-Based Stroke Diagnosis Making Global Prehospital Thrombolytic Treatment Possible,” vol. 61, no. 11, pp. 2806–2817, 2014, doi: 10.1109/TBME.2014.2330554.

[4] S. Mustafa, B. Mohammed, and A. Abbosh, “Novel Preprocessing Techniques for Accurate Microwave Imaging of Human Brain,” *IEEE Antennas Wirel. Propag. Lett.*, vol. 12, pp. 460–463, 2013, doi: 10.1109/LAWP.2013.2255095.

[5] M. Hopfer, R. Planas, A. Hamidipour, T. Henriksson, and S. Semenov, “Electromagnetic tomography for detection, differentiation, and monitoring of brain stroke: A virtual data and human head phantom study,” *IEEE Antennas Propag. Mag.*, vol. 59, no. 5, pp. 86–97, 2017, doi: 10.1109/MAP.2017.2732225.

[6] A. T. Mobashsher and A. M. Abbosh, “On-site Rapid Diagnosis of Intracranial Hematoma using Portable Multi-slice Microwave Imaging System,” *Sci. Rep.*, vol. 6, no. 1, p. 37620, Nov. 2016, doi: 10.1038/srep37620.

[7] R. Scapaticci, L. Di Donato, I. Catapano, and L. Crocco, “A FEASIBILITY STUDY ON MICROWAVE IMAGING FOR BRAIN STROKE MONITORING,” *Prog. Electromagn. Res. B*, vol. 40, pp. 305–324, 2012, doi: 10.2528/PIERB12022006.

[8] X. Wan, D. Yang, M. Cai, S. Han, S. Wu, and W. Hao, “The latest research status and prospect on microwave technology for monitoring concerned brain activity,” *Mechatron. Autom. ICMA 2015 IEEE Int. Conf. On*, pp. 297–302, 2015, doi: 10.1109/ICMA.2015.7237500.

[9] D. O. Rodriguez-Duarte, C. Origlia, J. A. T. Vasquez, R. Scapaticci, L. Crocco, and F. Vipiana, “Experimental Assessment of Real-Time Brain Stroke

Monitoring via a Microwave Imaging Scanner," *IEEE Open J. Antennas Propag.*, vol. 3, pp. 824–835, 2022, doi: 10.1109/OJAP.2022.3192884.

[10] J. A. Tobon Vasquez *et al.*, "A feasibility study for cerebrovascular diseases monitoring via microwave imaging," in *2017 International Conference on Electromagnetics in Advanced Applications (ICEAA)*, Verona: IEEE, Sep. 2017, pp. 1280–1282. doi: 10.1109/ICEAA.2017.8065506.

[11] I. Dilman, M. N. Akinci, M. Cayoren, and I. Akduman, "Differential microwave imaging of the stroke-affected brain via diffraction tomography," in *2017 25th Telecommunication Forum (TELFOR)*, Belgrade: IEEE, Nov. 2017, pp. 1–4. doi: 10.1109/TELFOR.2017.8249382.

[12] S. Y. Semenov *et al.*, "Microwave Tomography: Two-Dimensiorial System for Biological 1magin.g".

[13] M. Persson *et al.*, "Microwave based diagnostics and treatment in practice," in *2013 IEEE MTT-S International Microwave Workshop Series on RF and Wireless Technologies for Biomedical and Healthcare Applications (IMWS-BIO)*, Singapore, Singapore: IEEE, Dec. 2013, pp. 1–3. doi: 10.1109/IMWS-BIO.2013.6756231.

[14] M. R. Casu *et al.*, "A COTS-Based Microwave Imaging System for Breast-Cancer Detection," *IEEE Trans. Biomed. Circuits Syst.*, vol. 11, no. 4, pp. 804–814, Aug. 2017, doi: 10.1109/TBCAS.2017.2703588.

[15] T. M. Grzegorczyk, P. M. Meaney, P. A. Kaufman, R. M. di Florio-Alexander, and K. D. Paulsen, "Fast 3-D Tomographic Microwave Imaging for Breast Cancer Detection," *IEEE Trans. Med. Imaging*, vol. 31, no. 8, pp. 1584–1592, Aug. 2012, doi: 10.1109/TMI.2012.2197218.

[16] M. Guardiola, S. Capdevila, S. Blanch, J. Romeu, and L. Jofre, "UWB high-contrast robust tomographic imaging for medical applications," in *2009 International Conference on Electromagnetics in Advanced Applications*, Torino, Italy: IEEE, Sep. 2009, pp. 560–563. doi: 10.1109/ICEAA.2009.5297370.

[17] X. Wang, Y. Miao, J. Chen, C. Gong, Y. Wei, and Y. Yang, "High-Resolution Microwave Frequency Measurement Based on Optical Frequency Comb and Image Rejection Photonics Channelized Receiver," in *2022 IEEE 7th Optoelectronics Global Conference (OGC)*, Shenzhen, China: IEEE, Dec. 2022, pp. 30–35. doi: 10.1109/OGC55558.2022.10050949.

[18] A. F. Laine, “In the Spotlight: Biomedical Imaging,” *IEEE Rev. Biomed. Eng.*, vol. 1, pp. 4–7, 2008, doi: 10.1109/RBME.2008.2008221.

[19] N. Goel, A. Yadav, and B. M. Singh, “Medical image processing: A review,” in *2016 Second International Innovative Applications of Computational Intelligence on Power, Energy and Controls with their Impact on Humanity (CIPECH)*, Ghaziabad, India: IEEE, Nov. 2016, pp. 57–62. doi: 10.1109/CIPECH.2016.7918737.

[20] K. Hausegger, P. Lind, P. Reinprecht, I. Igerc, and T. Beyer, “Advantages and limitations of FDG PET in the follow-up of breast cancer,” *Eur. J. Nucl. Med. Mol. Imaging*, vol. 31, no. 0, pp. S125–S134, Jun. 2004, doi: 10.1007/s00259-004-1535-8.

[21] L. K. Niraj, “MRI in Dentistry- A Future Towards Radiation Free Imaging – Systematic Review,” *J. Clin. Diagn. Res.*, 2016, doi: 10.7860/JCDR/2016/19435.8658.

[22] P. Vilela and H. A. Rowley, “Brain ischemia: CT and MRI techniques in acute ischemic stroke,” *Eur. J. Radiol.*, vol. 96, pp. 162–172, Nov. 2017, doi: 10.1016/j.ejrad.2017.08.014.

[23] H. F. Cook, “The dielectric behaviour of some types of human tissues at microwave frequencies,” *Br. J. Appl. Phys.*, vol. 2, no. 10, pp. 295–300, Oct. 1951, doi: 10.1088/0508-3443/2/10/304.

[24] M. Lazebnik *et al.*, “A large-scale study of the ultrawideband microwave dielectric properties of normal, benign and malignant breast tissues obtained from cancer surgeries,” *Phys. Med. Biol.*, vol. 52, no. 20, pp. 6093–6115, Oct. 2007, doi: 10.1088/0031-9155/52/20/002.

[25] C. Gabriel, S. Gabriel, and E. Corthout, “The dielectric properties of biological tissues: I. Literature survey,” *Phys. Med. Biol.*, vol. 41, no. 11, pp. 2231–2249, Nov. 1996, doi: 10.1088/0031-9155/41/11/001.

[26] T. K. Bera, “A Review on The Medical Applications of Electroencephalography (EEG),” in *2021 Seventh International conference on Bio Signals, Images, and Instrumentation (ICBSII)*, Chennai, India: IEEE, Mar. 2021, pp. 1–6. doi: 10.1109/ICBSII51839.2021.9445153.

[27] V. Davis and S. Devane, “Diagnosis & classification of brain hemorrhage,” in *2017 International Conference on Advances in Computing, Communication and*

Control (ICAC3), Mumbai: IEEE, Dec. 2017, pp. 1–6. doi: 10.1109/ICAC3.2017.8318764.

[28] H. Kuang, B. K. Menon, and W. Qiu, “Segmenting Hemorrhagic and Ischemic Infarct Simultaneously From Follow-Up Non-Contrast CT Images in Patients With Acute Ischemic Stroke,” *IEEE Access*, vol. 7, pp. 39842–39851, 2019, doi: 10.1109/ACCESS.2019.2906605.

[29] J. Ljungqvist, S. Candefjord, M. Persson, L. Jönsson, T. Skoglund, and M. Elam, “Clinical Evaluation of a Microwave-Based Device for Detection of Traumatic Intracranial Hemorrhage,” *J. Neurotrauma*, vol. 34, no. 13, pp. 2176–2182, Jul. 2017, doi: 10.1089/neu.2016.4869.

[30] R. Chandra, H. Zhou, I. Balasingham, and R. M. Narayanan, “On the Opportunities and Challenges in Microwave Medical Sensing and Imaging,” *IEEE Trans. Biomed. Eng.*, vol. 62, no. 7, pp. 1667–1682, Jul. 2015, doi: 10.1109/TBME.2015.2432137.

[31] M. Sagheer, H. Sami, K. Riaz, M. Qasim Mehmood, and M. Zubair, “Performance Comparison of Image Reconstruction Algorithms in Microwave Imaging for Breast Cancer Screening,” in *2021 1st International Conference on Microwave, Antennas & Circuits (ICMAC)*, Islamabad, Pakistan: IEEE, Dec. 2021, pp. 1–2. doi: 10.1109/ICMAC54080.2021.9678274.

[32] N. Alsbou, K. Espinosa, N. Ashley, N. Wickware, and I. Ali, “Microwave Imaging System for Soft Tissue Imaging of Cancer Patients,” in *2021 IEEE 21st Annual Wireless and Microwave Technology Conference (WAMICON)*, Sand Key, FL, USA: IEEE, Apr. 2021, pp. 1–4. doi: 10.1109/WAMICON47156.2021.9443581.

[33] W. X. Tan, Y. L. Qi, Y. P. Wang, W. Hong, and X. L. Yang, “Reserch on the microwave snapshot imaging radar based on antenna array,” in *IET International Radar Conference 2013*, Xi’an, China: Institution of Engineering and Technology, 2013, pp. 0535–0535. doi: 10.1049/cp.2013.0190.

[34] L. E. Larsen and J. H. Jacobi, “Microwave scattering parameter imagery of an isolated canine kidney,” *Med. Phys.*, vol. 6, no. 5, pp. 394–403, Sep. 1979, doi: 10.1118/1.594595.

[35] A.-J. Berteaud and M. Dardalhon, “Biological Effects by Microwaves,” in *7th European Microwave Conference, 1977*, Copenhagen, Denmark: IEEE, Oct. 1977, pp. 581–589. doi: 10.1109/EUMA.1977.332396.

[36] C. H. Sutton and F. B. Carroll, “Changes in Tumor Blood Flow Produced by Microwave Induced Hyperthermia (Abstract),” in *MTT-S International Microwave Symposium Digest*, San Diego, CA, USA: MTT005, 1977, pp. 258–258. doi: 10.1109/MWSYM.1977.1124426.

[37] E. R. Atkinson, “Microwave-Induced Hyperthermia Dose Definition,” *IEEE Trans. Microw. Theory Tech.*, vol. 26, no. 8, pp. 595–598, Aug. 1978, doi: 10.1109/TMTT.1978.1129443.

[38] A. Priou and A. Deficis, “Applications of Microwaves to Medical Diagnostic First approach of an active microwave imaging,” in *11th European Microwave Conference, 1981*, Amsterdam, Netherlands: IEEE, Oct. 1981, pp. 438–442. doi: 10.1109/EUMA.1981.332928.

[39] T. C. Guo, W. W. Guo, and L. E. Larsen, “A Local Field Study of a Water-Immersed Microwave Antenna Array for Medical Imagery and Therapy,” *IEEE Trans. Microw. Theory Tech.*, vol. 32, no. 8, pp. 844–854, Aug. 1984, doi: 10.1109/TMTT.1984.1132781.

[40] J. Krug and P. Edenhofer, “Microwave Acoustic Imaging for Medical Applications,” in *15th European Microwave Conference, 1985*, Paris, France: IEEE, Oct. 1985, pp. 655–660. doi: 10.1109/EUMA.1985.333552.

[41] J. B. Andersen, “Medical Applications of Microwaves,” in *17th European Microwave Conference, 1987*, Rome, Italy: IEEE, Oct. 1987, pp. 50–56. doi: 10.1109/EUMA.1987.333695.

[42] M. T. Islam, M. Z. Mahmud, M. T. Islam, S. Kibria, and M. Samsuzzaman, “A Low Cost and Portable Microwave Imaging System for Breast Tumor Detection Using UWB Directional Antenna array,” *Sci. Rep.*, vol. 9, no. 1, p. 15491, Oct. 2019, doi: 10.1038/s41598-019-51620-z.

[43] A. W. Preece, R. H. Johnson, J. L. Green, and M. P. Robinson, “Dielectric imaging for localisation and detection of breast tumours,” in *1993 IEEE MTT-S International Microwave Symposium Digest*, Atlanta, GA, USA: IEEE, 1993, pp. 1145–1146. doi: 10.1109/MWSYM.1993.277073.

[44] E. C. Fear and M. A. Stuchly, “Confocal microwave imaging for breast tumor detection: a study of resolution and detection ability,” in *2001 Conference Proceedings of the 23rd Annual International Conference of the IEEE Engineering in Medicine and Biology Society*, Istanbul, Turkey: IEEE, 2001, pp. 2355–2358. doi: 10.1109/IEMBS.2001.1017250.

[45] S. C. Hagness, A. Taflove, and J. E. Bridges, “Three-dimensional FDTD analysis of a pulsed microwave confocal system for breast cancer detection: design of an antenna-array element,” *IEEE Trans. Antennas Propag.*, vol. 47, no. 5, pp. 783–791, May 1999, doi: 10.1109/8.774131.

[46] K. D. Paulsen, S. P. Poplack, Dun Li, M. W. Fanning, and P. M. Meaney, “A clinical prototype for active microwave imaging of the breast,” *IEEE Trans. Microw. Theory Tech.*, vol. 48, no. 11, pp. 1841–1853, Nov. 2000, doi: 10.1109/22.883861.

[47] D. Li, P. M. Meaney, M. W. Fanning, Q. Fang, S. A. Pendergrass, and T. Raynolds, “Spectrum analysis of microwave breast examination data and reconstructed images,” in *Proceedings IEEE International Symposium on Biomedical Imaging*, Washington, DC, USA: IEEE, 2002, pp. 62–65. doi: 10.1109/ISBI.2002.1029193.

[48] P. M. Meaney *et al.*, “Microwave breast imaging with an under-determined reconstruction parameter mesh,” in *2004 2nd IEEE International Symposium on Biomedical Imaging: Macro to Nano (IEEE Cat No. 04EX821)*, Arlington, VA, USA: IEEE, 2004, pp. 1369–1372. doi: 10.1109/ISBI.2004.1398801.

[49] W. C. Chew and Y. M. Wang, “Reconstruction of two-dimensional permittivity distribution using the distorted Born iterative method,” *IEEE Trans. Med. Imaging*, vol. 9, no. 2, pp. 218–225, Jun. 1990, doi: 10.1109/42.56334.

[50] P. Mojabi and J. LoVetri, “Overview and Classification of Some Regularization Techniques for the Gauss-Newton Inversion Method Applied to Inverse Scattering Problems,” *IEEE Trans. Antennas Propag.*, vol. 57, no. 9, pp. 2658–2665, Sep. 2009, doi: 10.1109/TAP.2009.2027161.

[51] P. M. van den Berg and R. E. Kleinman, “A contrast source inversion method,” *Inverse Probl.*, vol. 13, no. 6, pp. 1607–1620, Dec. 1997, doi: 10.1088/0266-5611/13/6/013.

[52] B. Amin, C. Sheridan, D. Kelly, A. Shahzad, M. O’Halloran, and M. A. Elahi, “Microwave bone imaging: experimental evaluation of calcaneus bone phantom and imaging prototype,” in *2020 IEEE MTT-S International Microwave Biomedical Conference (IMBioC)*, Toulouse, France: IEEE, Dec. 2020, pp. 1–3. doi: 10.1109/IMBIoC47321.2020.9385055.

[53] K. C. Santos, Carlos. A. Fernandes, and J. R. Costa, “A study on the sensitivity of microwave imaging for detecting small-width bone fractures,” in *2021 15th*

European Conference on Antennas and Propagation (EuCAP), Dusseldorf, Germany: IEEE, Mar. 2021, pp. 1–4. doi: 10.23919/EuCAP51087.2021.9411065.

[54] Yong-zhong Hu and Zheng-ou Zhou, “Simulation on 2D microwave imaging of finger joint with a Newton iterative method,” in *2010 International Conference on Bioinformatics and Biomedical Technology*, Chengdu, China: IEEE, 2010, pp. 279–282. doi: 10.1109/ICBBT.2010.5478961.

[55] A. M. Abbosh, S. A. Rezaeieh, and K. Bialkowski, “Microwave techniques as diagnostic tool for congestive heart failure,” in *2014 IEEE MTT-S International Microwave Workshop Series on RF and Wireless Technologies for Biomedical and Healthcare Applications (IMWS-Bio2014)*, London, United Kingdom: IEEE, Dec. 2014, pp. 1–3. doi: 10.1109/IMWS-BIO.2014.7032406.

[56] J. C. Lin and M. J. Clarke, “Microwave imaging of cerebral edema,” *Proc. IEEE*, vol. 70, no. 5, pp. 523–524, 1982, doi: 10.1109/PROC.1982.12341.

[57] N. Ghavami *et al.*, “The Use of Metasurfaces to Enhance Microwave Imaging: Experimental Validation for Tomographic and Radar-Based Algorithms,” *IEEE Open J. Antennas Propag.*, vol. 3, pp. 89–100, 2022, doi: 10.1109/OJAP.2021.3135146.

[58] I. El Kanfoud *et al.*, “Whole-microwave system modeling for brain imaging,” in *2015 IEEE Conference on Antenna Measurements & Applications (CAMA)*, Chiang Mai: IEEE, Nov. 2015, pp. 1–4. doi: 10.1109/CAMA.2015.7428123.

[59] J. Hakala, J. Kilpijarvi, M. Sarestoniemi, M. Hamalainen, S. Myllymaki, and T. Myllyla, “Microwave Sensing of Brain Water – a Simulation and Experimental Study Using Human Brain Models,” *IEEE Access*, vol. 8, pp. 111303–111315, 2020, doi: 10.1109/ACCESS.2020.3001867.

[60] M. Hopfer, R. Planas, A. Hamidipour, T. Henriksson, and S. Semenov, “Electromagnetic Tomography for Detection, Differentiation, and Monitoring of Brain Stroke: A Virtual Data and Human Head Phantom Study,” *IEEE Antennas Propag. Mag.*, vol. 59, no. 5, pp. 86–97, Oct. 2017, doi: 10.1109/MAP.2017.2732225.

[61] B. Mohammed, A. Abbosh, and D. Ireland, “Directive wideband antenna for microwave imaging system for brain stroke detection,” in *2012 Asia Pacific Microwave Conference Proceedings*, Kaohsiung, Taiwan: IEEE, Dec. 2012, pp. 640–642. doi: 10.1109/APMC.2012.6421688.

[62] "Learn about stroke," *World Stroke Organization*. https://www.world-stroke.org/world-stroke-day-campaign/why-stroke-matters/learn-about-stroke (accessed Mar. 22, 2023).

[63] T. Thayabaranathan *et al.*, "Global stroke statistics 2022," *Int. J. Stroke*, vol. 17, no. 9, pp. 946–956, Oct. 2022, doi: 10.1177/17474930221123175.

[64] "Burden of Stroke in Europe." https://www.ahajournals.org/doi/epub/10.1161/STROKEAHA.120.029606 (accessed Mar. 22, 2023).

[65] P.-H. Tournier *et al.*, "Numerical Modeling and High-Speed Parallel Computing: New Perspectives on Tomographic Microwave Imaging for Brain Stroke Detection and Monitoring," *IEEE Antennas Propag. Mag.*, vol. 59, no. 5, pp. 98–110, Oct. 2017, doi: 10.1109/MAP.2017.2731199.

[66] Y. Béjot, H. Bailly, J. Durier, and M. Giroud, "Epidemiology of stroke in Europe and trends for the 21st century," *Presse Médicale*, vol. 45, no. 12, pp. e391–e398, Dec. 2016, doi: 10.1016/j.lpm.2016.10.003.

[67] A. Fhager and M. Persson, "A microwave measurement system for stroke detection," in *2011 Loughborough Antennas & Propagation Conference*, Loughborough, United Kingdom: IEEE, Nov. 2011, pp. 1–2. doi: 10.1109/LAPC.2011.6114001.

[68] A. Naghibi and A. R. Attari, "Near-Field Radar-Based Microwave Imaging for Breast Cancer Detection: A Study on Resolution and Image Quality," *IEEE Trans. Antennas Propag.*, vol. 69, no. 3, pp. 1670–1680, Mar. 2021, doi: 10.1109/TAP.2020.3016407.

[69] R. de L. Kronig, "On the Theory of Dispersion of X-Rays," *J. Opt. Soc. Am.*, vol. 12, no. 6, p. 547, Jun. 1926, doi: 10.1364/JOSA.12.000547.

[70] S. Ahsan, W. Guo, O. Karadima, and P. Kosmas, "Experimental Comparison of Two Printed Monopole Antenna Designs for Microwave Tomography," in *2019 IEEE Asia-Pacific Microwave Conference (APMC)*, Singapore, Singapore: IEEE, Dec. 2019, pp. 500–502. doi: 10.1109/APMC46564.2019.9038734.

[71] Ziwen Guo, Zhenzhuang Miao, and P. Kosmas, "Application of the DBIM-TwIST Algorithm to 3-D Microwave Tomography Data," in *12th European Conference on Antennas and Propagation (EuCAP 2018)*, London, UK: Institution of Engineering and Technology, 2018, p. 405 (4 pp.)-405 (4 pp.). doi: 10.1049/cp.2018.0764.

[72] A. Munawar Qureshi, Z. Mustansar, and S. Mustafa, “Finite-element analysis of microwave scattering from a three-dimensional human head model for brain stroke detection,” *R. Soc. Open Sci.*, vol. 5, no. 7, p. 180319, Jul. 2018, doi: 10.1098/rsos.180319.

[73] D. O. Rodriguez-Duarte, J. A. T. Vasquez, R. Scapaticci, L. Crocco, and F. Vipiana, “Assessing a Microwave Imaging System for Brain Stroke Monitoring via High Fidelity Numerical Modelling,” *IEEE J. Electromagn. RF Microw. Med. Biol.*, vol. 5, no. 3, pp. 238–245, Sep. 2021, doi: 10.1109/JERM.2020.3049071.

[74] F. Mesa and D. R. Jackson, “The danger of high-frequency spurious effects on wide microstrip line,” in *2002 IEEE MTT-S International Microwave Symposium Digest (Cat. No.02CH37278)*, Seattle, WA, USA: IEEE, 2002, pp. 945–948. doi: 10.1109/MWSYM.2002.1011785.

[75] A. Joshi, L. K. Verma, and R. Singhal, “Spurious radiation suppression in slotted hexagonal antenna using complementary split ring resonators,” in *2017 Progress in Electromagnetics Research Symposium - Fall (PIERS - FALL)*, Singapore: IEEE, Nov. 2017, pp. 683–688. doi: 10.1109/PIERS-FALL.2017.8293222.

[76] E. Noh and K. Kim, “Effects of MWT Radiation on Sidelobe Levels in mm-Wave Microstrip Array Antenna,” in *2019 IEEE International Symposium on Antennas and Propagation and USNC-URSI Radio Science Meeting*, Atlanta, GA, USA: IEEE, Jul. 2019, pp. 873–874. doi: 10.1109/APUSNCURSINRSM.2019.8888767.

[77] B. K. Kanaujia, S. K. Gupta, J. Kishor, and D. Gangwar, Eds., *Printed Antennas: Theory and Design*, 1st ed. First edition. | Boca Raton, FL : CRC Press, 2021.: CRC Press, 2020. doi: 10.1201/9780367420451.

[78] D. Anandkumar and R. G. Sangeetha, “Design and analysis of aperture coupled micro strip patch antenna for radar applications,” *Int. J. Intell. Netw.*, vol. 1, pp. 141–147, 2020, doi: 10.1016/j.ijin.2020.11.002.

[79] P. D. M. Pozar, “A Review of Aperture Coupled Microstrip Antennas: History, Operation, Development, and Applications”.

[80] M. Civerolo and D. Arakaki, “Aperture coupled patch antenna design methods,” in *2011 IEEE International Symposium on Antennas and Propagation (APSURSI)*, Spokane, WA: IEEE, Jul. 2011, pp. 876–879. doi: 10.1109/APS.2011.5996415.

[81] Mohamad Kamal A Rahim, *Advanced antenna technology design*. Skudai, Johor: Penerbit Universiti Teknologi Malaysia, 2007.

[82] N. Iqbal and S. Karamzadeh, "UWB Microstrip Antenna Design for Microwave Imaging Systems," *Int. J. Electron. Mech. Mechatron. Eng.*, vol. 7, no. 2, pp. 1411–1417, Jun. 2017, doi: 10.17932/IAU.IJEMME.21460604.2017.7/2.1411-1417.

[83] B. Yeboah-Akowuah, P. Kosmas, and Y. Chen, "A Q-Slot Monopole for UWB Body-Centric Wireless Communications," *IEEE Trans. Antennas Propag.*, vol. 65, no. 10, pp. 5069–5075, Oct. 2017, doi: 10.1109/TAP.2017.2740977.

[84] N. K. Nikolova, *Introduction to microwave imaging*. in EuMA high frequency technologies series. Cambridge New Nork, NY Port Melbourne Delhi Singapore: Cambridge University Press, 2017.

[85] Constantine A. Balanis, Ed., *Antenna Theory Analysis and Design*. in NCRP report, no. 69. Bethesda, Md, 1981.

[86] V. Hamsakutty, A. Lonappan, G. Bindu, J. Jacob, J. Yohannan, and K. T. Mathew, "Coupling medium for microwave medical imaging applications," vol. 39, no. 21, 2003, doi: 10.1049/el.

[87] B. J. Mohammed, A. M. Abbosh, and M. E. Bialkowski, "Design of tapered slot antenna operating in coupling liquid for ultrawideband microwave imaging systems," in *2011 IEEE International Symposium on Antennas and Propagation (APSURSI)*, Spokane, WA: IEEE, Jul. 2011, pp. 145–148. doi: 10.1109/APS.2011.5996662.

[88] B. Sohani, G. Tiberi, N. Ghavami, M. Ghavami, S. Dudley, and A. Rahmani, "Microwave Imaging for Stroke Detection: Validation on Head-mimicking Phantom," in *2019 PhotonIcs & Electromagnetics Research Symposium - Spring (PIERS-Spring)*, Rome, Italy: IEEE, Jun. 2019, pp. 940–948. doi: 10.1109/PIERS-Spring46901.2019.9017851.

[89] P. J. Gibson, "The Vivaldi Aerial," in *1979 9th European Microwave Conference*, Brighton, UK: IEEE, Sep. 1979, pp. 101–105. doi: 10.1109/EUMA.1979.332681.

[90] G. E., "Improved design of theVivaldi antenna," *IEE ProcHMicrow Antennas Propag*, vol. 135, no. 2, p. 89, 1988.

[91] A. Z. Hood, T. Karacolak, and E. Topsakal, "A Small Antipodal Vivaldi Antenna for Ultrawide-Band Applications," *IEEE Antennas Wirel. Propag. Lett.*, vol. 7, pp. 656–660, 2008, doi: 10.1109/LAWP.2008.921352.

[92] M. Moosazadeh and S. Kharkovsky, "A Compact High-Gain and Front-to-Back Ratio Elliptically Tapered Antipodal Vivaldi Antenna With Trapezoid-Shaped Dielectric Lens," *IEEE Antennas Wirel. Propag. Lett.*, vol. 15, pp. 552–555, 2016, doi: 10.1109/LAWP.2015.2457919.

[93] S. A. AbdelBaky and H. F. Hammad, "Modified Elliptical Antipodal Vivaldi Antenna with Elliptical Tapered Slot Edge and Circular loads," in *2017 International Workshop on Antenna Technology: Small Antennas, Innovative Structures, and Applications (iWAT)*, Athens, Greece: IEEE, 2017, pp. 199–202. doi: 10.1109/IWAT.2017.7915357.

[94] B. Biswas, R. Ghatak, and D. R. Poddar, "A Fern Fractal Leaf Inspired Wideband Antipodal Vivaldi Antenna for Microwave Imaging System," *IEEE Trans. Antennas Propag.*, vol. 65, no. 11, pp. 6126–6129, Nov. 2017, doi: 10.1109/TAP.2017.2748361.

[95] S. Ahsan, B. Yeboah-Akowuah, K. Panagiotis, H. Cano García, G. Palikaras, and E. Kallos, "Balanced Antipodal Vivaldi Antenna for Microwave Tomography," in *Proceedings of the 4th International Conference on Wireless Mobile Communication and Healthcare - "Transforming healthcare through innovations in mobile and wireless technologies,"* Athens, Greece: ICST, 2014. doi: 10.4108/icst.mobihealth.2014.257515.

[96] M. Wang, L. Crocco, S. Costanzo, R. Scapaticci, and M. Cavagnaro, "A Compact Slot-Loaded Antipodal Vivaldi Antenna for a Microwave Imaging System to Monitor Liver Microwave Thermal Ablation," *IEEE Open J. Antennas Propag.*, vol. 3, pp. 700–708, 2022, doi: 10.1109/OJAP.2022.3183750.

[97] J. T. Bernhard, P. E. Mayes, D. Schaubert, and R. J. Mailloux, "A Commemoration of Deschamps and Sichak's Microstrip Microwave Antennas:50 Years of Development, Divergence, and New Directions:," Defense Technical Information Center, Fort Belvoir, VA, Nov. 2006. doi: 10.21236/ADA457574.

[98] D. M. Pozar, "Microstrip antennas," *Proc. IEEE*, vol. 80, no. 1, pp. 79–91, Jan. 1992, doi: 10.1109/5.119568.

[99] Ramesh Garg, *Microstrip Antenna Design Handbook*. Artech House.

[100] E. Bogatin, "Design rules for microstrip capacitance," *IEEE Trans. Compon. Hybrids Manuf. Technol.*, vol. 11, no. 3, pp. 253–259, Sep. 1988, doi: 10.1109/33.16649.

[101] Kai-Fong Lee and Kin-Fai Tong, “Microstrip Patch Antennas—Basic Characteristics and Some Recent Advances,” *Proc. IEEE*, vol. 100, no. 7, pp. 2169–2180, Jul. 2012, doi: 10.1109/JPROC.2012.2183829.

[102] A. Bouvy, G. J. Mazzaro, K. A. Gallagher, K. Sherbondy, and N. Behdad, “A Dual-Band Patch Antenna Employing a Folded Probe Feed for Nonlinear Radar Applications,” *IEEE Trans. Antennas Propag.*, vol. 71, no. 3, pp. 2070–2081, Mar. 2023, doi: 10.1109/TAP.2022.3233450.

[103] M. Ostadrahimi, P. Mojabi, S. Noghanian, L. Shafai, S. Pistorius, and J. LoVetri, “A Novel Microwave Tomography System Based on the Scattering Probe Technique,” *IEEE Trans. Instrum. Meas.*, vol. 61, no. 2, pp. 379–390, Feb. 2012, doi: 10.1109/TIM.2011.2161931.

[104] J. E. Ruyle and J. T. Bernhard, “Signal Flow Graph for a Probe-Fed Microstrip Patch Antenna,” *IEEE Antennas Wirel. Propag. Lett.*, vol. 8, pp. 935–938, 2009, doi: 10.1109/LAWP.2009.2027726.

[105] S. M. Aguilar, M. A. Al-Joumayly, M. J. Burfeindt, N. Behdad, and S. C. Hagness, “Multiband Miniaturised Patch Antennas for a Compact, Shielded Microwave Breast Imaging Array,” *IEEE Trans. Antennas Propag.*, vol. 62, no. 3, pp. 1221–1231, Mar. 2014, doi: 10.1109/TAP.2013.2295615.

[106] M. A. Al-Joumayly, S. M. Aguilar, N. Behdad, and S. C. Hagness, “Dual-Band Miniaturised Patch Antennas for Microwave Breast Imaging,” *IEEE Antennas Wirel. Propag. Lett.*, vol. 9, pp. 268–271, 2010, doi: 10.1109/LAWP.2010.2045871.

[107] Md. Rokunuzzaman, Md. Samsuzzaman, and M. T. Islam, “Unidirectional Wideband 3-D Antenna for Human Head-Imaging Application,” *IEEE Antennas Wirel. Propag. Lett.*, vol. 16, pp. 169–172, 2017, doi: 10.1109/LAWP.2016.2565610.

[108] S. Ahsan, Z. Guo, I. Gouzouasis, E. Kallos, and P. Kosmas, “Development of a slotted triangular patch antenna for microwave tomography,” in *2016 10th European Conference on Antennas and Propagation (EuCAP)*, Davos, Switzerland: IEEE, Apr. 2016, pp. 1–2. doi: 10.1109/EuCAP.2016.7481670.

[109] L. Wang, X.-X. Yang, T. Lou, and S. Gao, “A Miniaturised Differentially Fed Patch Antenna Based on Capacitive Slots,” *IEEE Antennas Wirel. Propag. Lett.*, vol. 21, no. 7, pp. 1472–1476, Jul. 2022, doi: 10.1109/LAWP.2022.3171841.

[110] W. C. Mok, S. H. Wong, K. M. Luk, and K. F. Lee, “Single-Layer Single-Patch Dual-Band and Triple-Band Patch Antennas,” *IEEE Trans. Antennas Propag.*, vol. 61, no. 8, pp. 4341–4344, Aug. 2013, doi: 10.1109/TAP.2013.2260516.

[111] D. Guha and C. Kumar, “Microstrip Patch versus Dielectric Resonator Antenna Bearing All Commonly Used Feeds: An experimental study to choose the right element,” *IEEE Antennas Propag. Mag.*, vol. 58, no. 1, pp. 45–55, Feb. 2016, doi: 10.1109/MAP.2015.2501231.

[112] D. M. Pozar, “A Microstrip Antenna Aperture Coupled to a Microstrip Line,” *Electron. Lett.*, vol. 21, pp. 49–50, Jan. 1985.

[113] J. P. Daniel, G. Dubost, C. Terret, J. Citerne, and M. Drissi, “Research on planar antennas and arrays: ‘structures Rayonnantes,’” *IEEE Antennas Propag. Mag.*, vol. 35, no. 1, pp. 14–38, Feb. 1993, doi: 10.1109/74.210827.

[114] M. J. Veljovic and A. K. Skrivervik, “Aperture-Coupled Low-Profile Wideband Patch Antennas for CubeSat,” *IEEE Trans. Antennas Propag.*, vol. 67, no. 5, pp. 3439–3444, May 2019, doi: 10.1109/TAP.2019.2900428.

[115] S. Bonam, J. Joseph, C. Hemanth Kumar, A. K. Panigrahi, S. R. K. Vanjari, and S. G. Singh, “Fabrication of On-Silicon Aperture Coupled Patch Antenna Through Micromachining and Cu-Cu Thermocompression Bonding,” *IEEE Trans. Semicond. Manuf.*, vol. 35, no. 4, pp. 626–632, Nov. 2022, doi: 10.1109/TSM.2022.3201300.

[116] M. M. Honari, A. Abdipour, and G. Moradi, “Bandwidth and Gain Enhancement of an Aperture Antenna With Modified Ring Patch,” *IEEE Antennas Wirel. Propag. Lett.*, vol. 10, pp. 1413–1416, 2011, doi: 10.1109/LAWP.2011.2178998.

[117] J. Zhang, S. Yan, X. Hu, and G. A. E. Vandenbosch, “Aperture-coupled wearable antenna with miniature feeding network,” in *2017 11th European Conference on Antennas and Propagation (EUCAP)*, Paris, France: IEEE, Mar. 2017, pp. 1031–1034. doi: 10.23919/EuCAP.2017.7928293.

[118] I. Zhou, L. Jofre, and J. Romeu, “Technology Assessment of Aperture Coupled Slot Antenna Array in Groove Gapwaveguide for 5G Millimeter Wave Applications,” *IEEE Access*, vol. 9, pp. 139556–139564, 2021, doi: 10.1109/ACCESS.2021.3119748.

[119] Q. Rao and R. H. Johnston, “Modified Aperture Coupled Microstrip Antenna,” *IEEE Trans. Antennas Propag.*, vol. 52, no. 12, pp. 3397–3401, Dec. 2004, doi: 10.1109/TAP.2004.836415.

[120] J.-S. Row and J.-F. Wu, “Aperture-Coupled Microstrip Antennas With Switchable Polarization,” *IEEE Trans. Antennas Propag.*, vol. 54, no. 9, pp. 2686–2691, Sep. 2006, doi: 10.1109/TAP.2006.880785.

[121] P. Kumari, R. K. Gangwar, and R. K. Chaudhary, “An Aperture-Coupled Stepped Dielectric Resonator UWB MIMO Antenna With AMC,” *IEEE Antennas Wirel. Propag. Lett.*, vol. 21, no. 10, pp. 2040–2044, Oct. 2022, doi: 10.1109/LAWP.2022.3189694.

[122] K. P. Ray, “Design Aspects of Printed Monopole Antennas for Ultra-Wide Band Applications,” vol. 2008, 2008, doi: 10.1155/2008/713858.

[123] N. Ojaroudi, M. Ojaroudi, and N. Ghadimi, “UWB Omnidirectional Square Monopole Antenna for Use in Circular Cylindrical Microwave Imaging Systems,” *IEEE Antennas Wirel. Propag. Lett.*, vol. 11, pp. 1350–1353, 2012, doi: 10.1109/LAWP.2012.2227137.

[124] K. P. Ray, “Design Aspects of Printed Monopole Antennas for Ultra-Wide Band Applications,” *Int. J. Antennas Propag.*, vol. 2008, pp. 1–8, 2008, doi: 10.1155/2008/713858.

[125] A. T. Mobashsher and A. M. Abbosh, “Performance of Directional and Omnidirectional Antennas in Wideband Head Imaging,” *IEEE Antennas Wirel. Propag. Lett.*, vol. 15, pp. 1618–1621, 2016, doi: 10.1109/LAWP.2016.2519527.

[126] F. Sadeghikia, “Analysis of Plasma Monopole Antenna Using Numerical Method and an Equivalent Circuit,” *IEEE Antennas Wirel. Propag. Lett.*, vol. 16, pp. 1711–1714, 2017, doi: 10.1109/LAWP.2017.2669091.

[127] Qi Luo, J. R. Pereira, and H. M. Salgado, “Compact Printed Monopole Antenna With Chip Inductor for WLAN,” *IEEE Antennas Wirel. Propag. Lett.*, vol. 10, pp. 880–883, 2011, doi: 10.1109/LAWP.2011.2166049.

[128] M. Alibakhshikenari *et al.*, “Wideband printed monopole antenna for application in wireless communication systems,” *IET Microw. Antennas Propag.*, vol. 12, no. 7, pp. 1222–1230, Jun. 2018, doi: 10.1049/iet-map.2017.0894.

[129] H. M. E. Misilmani, T. Naous, S. K. A. Khatib, and K. Y. Kabalan, “A Survey on Antenna Designs for Breast Cancer Detection Using Microwave Imaging,” *IEEE Access*, vol. 8, pp. 102570–102594, 2020, doi: 10.1109/ACCESS.2020.2999053.

[130] J. J. J. Sheela, S. Vanaja, R. Krishnan, V. Avinash., D. Aruna, and D. Harini, “Novel Directional Antennas for Microwave Breast Imaging Applications,” in

2020 International Conference on Smart Electronics and Communication (ICOSEC), Trichy, India: IEEE, Sep. 2020, pp. 599–603. doi: 10.1109/ICOSEC49089.2020.9215243.

[131] W. Guo, S. Ahsan, M. He, M. Koutsoupidou, and P. Kosmas, "Printed Monopole Antenna Designs for a Microwave Head Scanner," in *2018 18th Mediterranean Microwave Symposium (MMS)*, Istanbul: IEEE, Oct. 2018, pp. 384–386. doi: 10.1109/MMS.2018.8611962.

[132] C. P. Wen, "Coplanar Waveguide: A Surface Strip Transmission Line Suitable for Nonreciprocal Gyromagnetic Device Applications," *IEEE Trans. Microw. Theory Tech.*, vol. 17, no. 12, pp. 1087–1090, Dec. 1969, doi: 10.1109/TMTT.1969.1127105.

[133] Y. X. Wang, "Coplanar Waveguide Short-Gap Resonator for Medical Applications," *IEEE Trans. Microw. Theory Tech.*, vol. 33, no. 12, pp. 1310–1312, Dec. 1985, doi: 10.1109/TMTT.1985.1133218.

[134] E. Ponchak, D. Akinwande, R. Ciocan, S. R. LeClair, and M. Tabib-Azar, "Evanescent microwave probes using coplanar waveguide and stripline for super-resolution imaging of materials," in *1999 IEEE MTT-S International Microwave Symposium Digest (Cat. No.99CH36282)*, Anaheim, CA, USA: IEEE, 1999, pp. 1859–1862. doi: 10.1109/MWSYM.1999.780335.

[135] H.-W. Liu, C.-H. Ku, and C.-F. Yang, "Novel CPW-Fed Planar Monopole Antenna for WiMAX/WLAN Applications," *IEEE Antennas Wirel. Propag. Lett.*, vol. 9, pp. 240–243, 2010, doi: 10.1109/LAWP.2010.2044860.

[136] Chao Deng, Yong-jun Xie, and Ping Li, "CPW-Fed Planar Printed Monopole Antenna With Impedance Bandwidth Enhanced," *IEEE Antennas Wirel. Propag. Lett.*, vol. 8, pp. 1394–1397, 2009, doi: 10.1109/LAWP.2009.2039743.

[137] Meng-Ju Chiang, Tian-Fu Hung, Jia-Yi Sze, and Sheau-Shong Bor, "Miniaturised Dual-Band CPW-Fed Annular Slot Antenna Design With Arc-Shaped Tuning Stub," *IEEE Trans. Antennas Propag.*, vol. 58, no. 11, pp. 3710–3715, Nov. 2010, doi: 10.1109/TAP.2010.2071333.

[138] H. Chen, X. Yang, Y. Z. Yin, S. T. Fan, and J. J. Wu, "Triband Planar Monopole Antenna With Compact Radiator for WLAN/WiMAX Applications," *IEEE Antennas Wirel. Propag. Lett.*, vol. 12, pp. 1440–1443, 2013, doi: 10.1109/LAWP.2013.2287312.

[139] A. A. Omar, M. C. Scardelletti, Z. M. Hejazi, and N. Dib, “Design and Measurement of Self-Matched Dual-Frequency Coplanar Waveguide-Fed-Slot Antennas,” *IEEE Trans. Antennas Propag.*, vol. 55, no. 1, pp. 223–226, Jan. 2007, doi: 10.1109/TAP.2006.888475.

[140] A. K. Gautam, S. Yadav, and B. K. Kanaujia, “A CPW-Fed Compact UWB Microstrip Antenna,” *IEEE Antennas Wirel. Propag. Lett.*, vol. 12, pp. 151–154, 2013, doi: 10.1109/LAWP.2013.2244055.

[141] R. K. Raj, M. Joseph, C. K. Aanandan, K. Vasudevan, and P. Mohanan, “A New Compact Microstrip-Fed Dual-Band Coplanar Antenna for WLAN Applications,” *IEEE Trans. Antennas Propag.*, vol. 54, no. 12, pp. 3755–3762, Dec. 2006, doi: 10.1109/TAP.2006.886505.

[142] T. Shanmuganantham, K. Balamanikandan, and S. Raghavan, “CPW-Fed Slot Antenna for Wideband Applications,” *Int. J. Antennas Propag.*, vol. 2008, pp. 1–4, 2008, doi: 10.1155/2008/379247.

[143] A. Hossain, M. T. Islam, M. E. H. Chowdhury, and Md. Samsuzzaman, “A Grounded Coplanar Waveguide-Based Slotted Inverted Delta-Shaped Wideband Antenna for Microwave Head Imaging,” *IEEE Access*, vol. 8, pp. 185698–185724, 2020, doi: 10.1109/ACCESS.2020.3029595.

[144] Md. Z. Mahmud, M. T. Islam, N. Misran, S. Kibria, and Md. Samsuzzaman, “Microwave Imaging for Breast Tumor Detection Using Uniplanar AMC Based CPW-Fed Microstrip Antenna,” *IEEE Access*, vol. 6, pp. 44763–44775, 2018, doi: 10.1109/ACCESS.2018.2859434.

[145] H. M. Jafari, M. J. Deen, S. Hranilovic, and N. K. Nikolova, “A Study of Ultrawideband Antennas for Near-Field Imaging,” *IEEE Trans. Antennas Propag.*, vol. 55, no. 4, pp. 1184–1188, Apr. 2007, doi: 10.1109/TAP.2007.893405.

[146] M. A. Ashraf, K. Jamil, A. Telba, M. A. Alzabidi, and A. R. Sebak, “Design and Development of a Wideband Planar Yagi Antenna Using Tightly Coupled Directive Element,” *Micromachines*, vol. 11, no. 11, p. 975, Oct. 2020, doi: 10.3390/mi11110975.

[147] Z.-Y. Qian, W.-J. Sun, X.-F. Zhang, and J.-X. Chen, “An X-band magnetic dipole quasi-Yagi antenna based on a dielectric resonator,” *Int. J. Microw. Wirel. Technol.*, vol. 12, no. 3, pp. 240–245, Apr. 2020, doi: 10.1017/S1759078719001223.

[148] N. Kaneda, W. R. Deal, Yongxi Qian, R. Waterhouse, and T. Itoh, "A broadband planar quasi-Yagi antenna," *IEEE Trans. Antennas Propag.*, vol. 50, no. 8, pp. 1158–1160, Aug. 2002, doi: 10.1109/TAP.2002.801299.

[149] L. Yuan, W. Tang, and J. Liu, "Miniaturised broadband Quasi-Yagi antenna for wireless communication and recognition," in *2017 International Symposium on Intelligent Signal Processing and Communication Systems (ISPACS)*, Xiamen, China: IEEE, Nov. 2017, pp. 550–553. doi: 10.1109/ISPACS.2017.8266539.

[150] S. Fu, A. Xiong, W. Chen, and S. Fang, "A compact planar Moxon-Yagi composite antenna with end-fire radiation for dual-band applications," *Microw. Opt. Technol. Lett.*, vol. 62, no. 6, pp. 2328–2334, Jun. 2020, doi: 10.1002/mop.32331.

[151] C. G. Kakoyiannis, I. S. Karanasiou, M. Koutsoupidou, and N. Uzunoglu, "A unidirectional wideband printed Quasi-Yagi antenna for microwave breast imaging".

[152] S. A. Rezaeieh, M. A. Antoniades, and A. M. Abbosh, "Miniaturised Planar Yagi Antenna Utilizing Capacitively Coupled Folded Reflector," *IEEE Antennas Wirel. Propag. Lett.*, vol. 16, pp. 1977–1980, 2017, doi: 10.1109/LAWP.2017.2690973.

[153] B.-J. Liu, J.-H. Qiu, C.-L. Wang, and G.-Q. Li, "Pattern-Reconfigurable Cylindrical Dielectric Resonator Antenna Based on Parasitic Elements," *IEEE Access*, vol. 5, pp. 25584–25590, 2017, doi: 10.1109/ACCESS.2017.2771296.

[154] S.-J. Sun, Y.-C. Jiao, and Z. Weng, "Wide-Beam Dielectric Resonator Antenna With Attached Higher-Permittivity Dielectric Slabs," *IEEE Antennas Wirel. Propag. Lett.*, vol. 19, no. 3, pp. 462–466, Mar. 2020, doi: 10.1109/LAWP.2020.2968416.

[155] R. S., P. P. Kumar, and P. Saxena, "A Sub-1GHz Rectangular Dielectric Resonator Antenna for IoT," in *2019 IEEE International WIE Conference on Electrical and Computer Engineering (WIECON-ECE)*, Bangalore, India: IEEE, Nov. 2019, pp. 1–4. doi: 10.1109/WIECON-ECE48653.2019.9019920.

[156] K. S. Ryu and A. A. Kishk, "Evaluation of Dielectric Resonator Sensor for Near-Field Breast Tumor Detection," *IEEE Trans. Antennas Propag.*, vol. 59, no. 10, pp. 3738–3745, Oct. 2011, doi: 10.1109/TAP.2011.2163790.

[157] X. S. Fang, L. P. Weng, and Z. Fan, "Design of the Wideband and Low-Height Omnidirectional Cylindrical Dielectric Resonator Antenna Using Arced-

Apertures Feeding," *IEEE Access*, vol. 11, pp. 20128–20135, 2023, doi: 10.1109/ACCESS.2023.3249819.

[158] X. Lin, Y. Chen, Z. Gong, B.-C. Seet, L. Huang, and Y. Lu, "Ultrawideband Textile Antenna for Wearable Microwave Medical Imaging Applications," *IEEE Trans. Antennas Propag.*, vol. 68, no. 6, pp. 4238–4249, Jun. 2020, doi: 10.1109/TAP.2020.2970072.

[159] I. M. Saied, S. Chandran, and T. Arslan, "Integrated Flexible Hybrid Silicone-Textile Dual-Resonant Sensors and Switching Circuit for Wearable Neurodegeneration Monitoring Systems," *IEEE Trans. Biomed. Circuits Syst.*, vol. 13, no. 6, pp. 1304–1312, Dec. 2019, doi: 10.1109/TBCAS.2019.2951500.

[160] M. Wagih *et al.*, "Microwave-Enabled Wearables: Underpinning Technologies, Integration Platforms, and Next-Generation Roadmap," *IEEE J. Microw.*, vol. 3, no. 1, pp. 193–226, Jan. 2023, doi: 10.1109/JMW.2022.3223254.

[161] M. M. H. Mahfuz *et al.*, "Wearable Textile Patch Antenna: Challenges and Future Directions," *IEEE Access*, vol. 10, pp. 38406–38427, 2022, doi: 10.1109/ACCESS.2022.3161564.

[162] C. Hertleer, A. Tronquo, H. Rogier, L. Vallozzi, and L. Van Langenhove, "Aperture-Coupled Patch Antenna for Integration Into Wearable Textile Systems," *IEEE Antennas Wirel. Propag. Lett.*, vol. 6, pp. 392–395, 2007, doi: 10.1109/LAWP.2007.903498.

[163] B. Ivsic, D. Bonefacic, and J. Bartolic, "Considerations on Embroidered Textile Antennas for Wearable Applications," *IEEE Antennas Wirel. Propag. Lett.*, vol. 12, pp. 1708–1711, 2013, doi: 10.1109/LAWP.2013.2297698.

[164] H. Li, S. Sun, B. Wang, and F. Wu, "Design of Compact Single-Layer Textile MIMO Antenna for Wearable Applications," *IEEE Trans. Antennas Propag.*, vol. 66, no. 6, pp. 3136–3141, Jun. 2018, doi: 10.1109/TAP.2018.2811844.

[165] K. W. Lui, O. H. Murphy, and C. Toumazou, "A Wearable Wideband Circularly Polarized Textile Antenna for Effective Power Transmission on a Wirelessly-Powered Sensor Platform," *IEEE Trans. Antennas Propag.*, vol. 61, no. 7, pp. 3873–3876, Jul. 2013, doi: 10.1109/TAP.2013.2255094.

[166] H. Yang and X. Liu, "Wearable Dual-Band and Dual-Polarized Textile Antenna for On- and Off-Body Communications," *IEEE Antennas Wirel. Propag. Lett.*, vol. 19, no. 12, pp. 2324–2328, Dec. 2020, doi: 10.1109/LAWP.2020.3032540.

[167] G. A. Casula, G. Montisci, and G. Muntoni, “A Novel Design for Dual-Band Wearable Textile Eighth-Mode SIW Antennas,” *IEEE Access*, vol. 11, pp. 11555–11569, 2023, doi: 10.1109/ACCESS.2023.3242602.

[168] M. L. Scarpello, I. Kazani, C. Hertleer, H. Rogier, and D. Vande Ginste, “Stability and Efficiency of Screen-Printed Wearable and Washable Antennas,” *IEEE Antennas Wirel. Propag. Lett.*, vol. 11, pp. 838–841, 2012, doi: 10.1109/LAWP.2012.2207941.

[169] Y. Huang, A. Alieldin, and C. Song, “Equivalent Circuits and Analysis of a Generalized Antenna System”.

[170] Yu-Shin Wang and Shyh-Jong Chung, “A Short Open-End Slot Antenna With Equivalent Circuit Analysis,” *IEEE Trans. Antennas Propag.*, vol. 58, no. 5, pp. 1771–1775, May 2010, doi: 10.1109/TAP.2010.2044471.

[171] Chen-To Tai, “Theory of terminated monopole,” *IEEE Trans. Antennas Propag.*, vol. 32, no. 4, pp. 408–410, Apr. 1984, doi: 10.1109/TAP.1984.1143326.

[172] N. R. Ccoillo-Ramos, N. Aboserwal, Z. Qamar, and J. L. Salazar-Cerreno, “Improved Analytical Model for a Proximity Coupled Microstrip Patch Antenna (PC-MSPA),” *IEEE Trans. Antennas Propag.*, vol. 69, no. 10, pp. 6244–6252, Oct. 2021, doi: 10.1109/TAP.2021.3082570.

[173] J. H. Park, D. I. Kim, and K. W. Choi, “Analysis and Experiment on Multi-Antenna-to-Multi-Antenna RF Wireless Power Transfer,” *IEEE Access*, vol. 9, pp. 2018–2031, 2021, doi: 10.1109/ACCESS.2020.3047485.

[174] Y. Narita, K. Nozawa, and H. Hirayama, “Characteristic Mode Analysis of H-shaped Slot Patch Antenna with Class-F Load Function,” in *2022 Wireless Power Week (WPW)*, Bordeaux, France: IEEE, Jul. 2022, pp. 739–742. doi: 10.1109/WPW54272.2022.9901366.

[175] L. Jiang and J. Chen, “Design and Analysis of Microwave Energy Transmission System Based on 5.8GHz,” in *2020 IEEE 3rd International Conference on Electronic Information and Communication Technology (ICEICT)*, Shenzhen, China: IEEE, Nov. 2020, pp. 276–279. doi: 10.1109/ICEICT51264.2020.9334309.

[176] J. P. K. Sampath, A. Alphones, L. Y. Y. Kenneth, and D. M. Vilathgamuwa, “Analysis on normalized distance and scalability in designing wireless power transfer,” in *2015 IEEE PELS Workshop on Emerging Technologies: Wireless*

Power (2015 WoW), Daejeon, South Korea: IEEE, Jun. 2015, pp. 1–6. doi: 10.1109/WoW.2015.7132849.

[177] M. N. Abdallah, T. K. Sarkar, and M. Salazar-Palma, "Maximum power transfer versus efficiency," in *2016 IEEE International Symposium on Antennas and Propagation (APSURSI)*, Fajardo, PR, USA: IEEE, Jun. 2016, pp. 183–184. doi: 10.1109/APS.2016.7695800.

[178] X. Zeng, A. Fhager, and M. Persson, "Effects of noise on tomographic breast imaging," in *2011 XXXth URSI General Assembly and Scientific Symposium*, Istanbul: IEEE, Aug. 2011, pp. 1–4. doi: 10.1109/URSIGASS.2011.6051372.

[179] A. T. Mobashsher, K. S. Bialkowski, A. M. Abbosh, and S. Crozier, "Design and Experimental Evaluation of a Non-Invasive Microwave Head Imaging System for Intracranial Haemorrhage Detection," *PLOS ONE*, vol. 11, no. 4, p. e0152351, Apr. 2016, doi: 10.1371/journal.pone.0152351.

[180] D. M. Nguyen, N. D. Au, and C. Seo, "Aperture-Coupled Patch Antenna With Flat-Top Beam for Microwave Power Transmission," *IEEE Antennas Wirel. Propag. Lett.*, vol. 21, no. 10, pp. 2130–2134, Oct. 2022, doi: 10.1109/LAWP.2022.3193376.

[181] Md. Abdullah-Al-Mamun, Md. S. Anower, Md. R. Billah, and S. Datto, "Wideband Aperture Coupled Line Feeding Microstrip Patch Antenna Design Using Different Shaped Patches," in *2021 International Conference on Computer Communication and Informatics (ICCCI)*, Coimbatore, India: IEEE, Jan. 2021, pp. 1–6. doi: 10.1109/ICCCI50826.2021.9402296.

[182] M. K. A. Rahim, Z. W. Low, P. J. Soh, A. Asrokin, M. H. Jamaluddin, and T. Masri, "Aperture Coupled Microstrip Antenna with Different Feed Sizes and Aperture Positions," in *2006 International RF and Microwave Conference*, Putra Jaya: IEEE, Sep. 2006, pp. 31–35. doi: 10.1109/RFM.2006.331031.

[183] B. Jamali and T. Cook, "Comparative study of microstrip patch antenna feed network," in *2013 International Conference on Radar*, Adelaide, Australia: IEEE, Sep. 2013, pp. 179–183. doi: 10.1109/RADAR.2013.6651981.

[184] M. I. Nawaz, Z. Huiling, M. S. Sultan Nawaz, K. Zakim, S. Zamin, and A. Khan, "A review on wideband microstrip patch antenna design techniques," in *2013 International Conference on Aerospace Science & Engineering (ICASE)*, Islamabad, Pakistan: IEEE, Aug. 2013, pp. 1–8. doi: 10.1109/ICASE.2013.6785554.

[185] J. Zhang, J.-D. Zhang, W. Wu, and D.-G. Fang, “An Aperture-Coupled Shorted-Edge Patch Antenna With Low Cross Polarization, Adjustable Beamwidth, Wideband, and High Gain,” *IEEE Antennas Wirel. Propag. Lett.*, vol. 20, no. 10, pp. 2018–2022, Oct. 2021, doi: 10.1109/LAWP.2021.3102124.

[186] K. Naishadham, “Antenna design strategies to reduce coupling and interference in wireless communications systems,” in *2013 IEEE Radio and Wireless Symposium*, Austin, TX, USA: IEEE, Jan. 2013, pp. 61–63. doi: 10.1109/RWS.2013.6486641.

[187] M. Koutsoupidou *et al.*, “Dielectric permittivity of human blood of different lactate levels measured at millimeter waves,” in *2019 41st Annual International Conference of the IEEE Engineering in Medicine and Biology Society (EMBC)*, Berlin, Germany: IEEE, Jul. 2019, pp. 1183–1186. doi: 10.1109/EMBC.2019.8857488.

[188] A. Moradpour, O. Karadima, I. Alic, M. Ragulskis, F. Kienberger, and P. Kosmas, “Development of a Solid and Flexible Matching Medium for Microwave Medical Diagnostic Systems,” *Diagnostics*, vol. 11, no. 3, p. 550, Mar. 2021, doi: 10.3390/diagnostics11030550.

[189] S. N. Ahsan, “Design of a Microwave Tomography System for Medical Imaging Applications”.

[190] T. K. Das, “Design of a wideband Unidirectional Antenna for Microwave Head Imaging System,” *2018 3rd Int. Conf. Microw. Photonics ICMAP*, no. ICMAP, pp. 1–2, 2018, doi: 10.1109/ICMAP.2018.8354599.

[191] O. Karadima, P. Lu, I. Sotiriou, and P. Kosmas, “Experimental Validation of the DBIM-TwIST Algorithm for Brain Stroke Detection and Differentiation Using a Multi-Layered Anatomically Complex Head Phantom,” *IEEE Open J. Antennas Propag.*, vol. 3, pp. 274–286, 2022, doi: 10.1109/OJAP.2022.3150100.

[192] S. Ahsan *et al.*, “Design and Experimental Validation of a Multiple-Frequency Microwave Tomography System Employing the DBIM-TwIST Algorithm,” *Sensors*, vol. 18, no. 10, p. 3491, Oct. 2018, doi: 10.3390/s18103491.

[193] J. M. Bioucas-Dias and M. A. T. Figueiredo, “A New TwIST: Two-Step Iterative Shrinkage/Thresholding Algorithms for Image Restoration,” *IEEE Trans. Image Process.*, vol. 16, no. 12, pp. 2992–3004, Dec. 2007, doi: 10.1109/TIP.2007.909319.

[194] J. D. Shea, P. Kosmas, S. C. Hagness, and B. D. Van Veen, “Three-dimensional microwave imaging of realistic numerical breast phantoms via a multiple-frequency inverse scattering technique: Microwave imaging of realistic numerical breast phantoms,” *Med. Phys.*, vol. 37, no. 8, pp. 4210–4226, Jul. 2010, doi: 10.1118/1.3443569.

[195] Z. Miao and P. Kosmas, “Multiple-Frequency DBIM-TwIST Algorithm for Microwave Breast Imaging,” *IEEE Trans. Antennas Propag.*, vol. 65, no. 5, pp. 2507–2516, May 2017, doi: 10.1109/TAP.2017.2679067.

[196] O. Karadima, N. Ghavami, I. Sotiriou, and P. Kosmas, “Performance assessment of microwave tomography and radar imaging using an anthropomorphic brain phantom,” in *2020 XXXIIIrd General Assembly and Scientific Symposium of the International Union of Radio Science*, Rome, Italy: IEEE, Aug. 2020, pp. 1–4. doi: 10.23919/URSIGASS49373.2020.9232402.

[197] J. Corcoles, P. Lu, and P. Kosmas, “Finite Element Analysis of a Wideband Microwave Tomography System for Potential Medical Imaging,” in *2019 Joint International Symposium on Electromagnetic Compatibility, Sapporo and Asia-Pacific International Symposium on Electromagnetic Compatibility (EMC Sapporo/APEMC)*, Sapporo, Japan: IEEE, Jun. 2019, pp. 358–361. doi: 10.23919/EMCTokyo.2019.8893660.

[198] O. Karadima, P. Lu, I. Sotiriou, and P. Kosmas, “Evaluation of prior information in microwave tomography experiments for brain stroke detection,” in *2021 IEEE Conference on Antenna Measurements & Applications (CAMA)*, Antibes Juan-les-Pins, France: IEEE, Nov. 2021, pp. 535–539. doi: 10.1109/CAMA49227.2021.9703553.

Appendix

1. Fundamental Parameters of Antennas

Near field and far field: The reactive near field which is the near-field region immediately surrounding the antenna is defined as:

$$r < \sqrt{D^3/\lambda}$$

Radiating near field or Fresnel region refers to the region connecting reactive near field and far field, it is defined as $\sqrt{D^3/\lambda} < r < 2D^2/\lambda$; Far field is commonly taken to exist at distances greater than $2D^2/\lambda$ from the antenna.

Radiation pattern: Radiation pattern is defined as a mathematical function or a graphical representation of the radiation properties of the antenna as a function of space coordinates. In most cases, the radiation pattern is determined in the far-field region and is represented as a function of the directional coordinates. Radiation properties include power flux density, radiation intensity, field strength, directivity, phase or polarisation.

Radiation intensity: the power radiated from an antenna per unit solid angle.

Directivity: 1983 version of IEEE Standard Definitions of Terms for Antennas defines the directivity as the radiation intensity in a given direction from the antenna to the radiation intensity averaged over all directions. If the direction is not specified, directivity is typically given as the maximal directivity found among all possible angles.

Total efficiency: the ratio of power radiated by the antenna to the power incident from the network. The main losses are reflections between transmission line and antenna due to mismatch and conduction and dielectric losses.

Radiation efficiency: the ratio of the power radiated by the antenna to the power that gets into the antenna. The heat-producing ohmic loss from each antenna component is the main loss of power.

Gain: the ratio of the intensity in a given direction to the radiation intensity that would be obtained. It is defined as the product of efficiency and directivity of the antenna.

Bandwidth of antenna: the range of frequencies within which the performance of the antenna, with respect to some characteristic, conforms to a specified standard.

Specifically, -10dB is typically defined as the maximum limit for reflection coefficient in microwave imaging applications, thus frequency range whose return loss smaller than -10dB is bandwidth.

Input impedance: the impedance presented by an antenna at its terminals or the ratio of the voltage to current at a pair of terminals or the ratio of the appropriate components of the electric to magnetic fields at a point. Input impedance of an antenna is typically defined as $Z_A = R_A + jX_A$, where Z_A the antenna impedance, R_A the antenna resistance and X_A the antenna reactance. Generally, the antenna resistance R_A consists of radiation resistance R_r and loss resistance R_L. $R_A = R_r + R_L$

Antenna radiation efficiency: the ratio of the power radiated through R_r to the total power delivered to load resistance R_L and radiation resistance R_r.

2. Scattering Parameter

In the context of designing a microwave imaging system for brain stroke detection, understanding the behaviour of the multiport network and its S-parameter matrix is crucial. The incident power wave is defined as $a_i = \frac{1}{2}k_i(V_i + Z_i I_i)$, where $k_i = \frac{1}{\sqrt{R\{Z_i\}}}$. The reflected power wave is defined as $b_i = \frac{1}{2}k_i(V_i - Z_i^* I_i)$. As the same antenna is used for each port, the impedance of each port Z_i takes the same value Z_0. The relationship between the incident and reflected waves for each port is captured in the S-parameter matrix S. For a generic N-port network, the relationship between the incident and reflected waves can be expressed as $b = Sa$, where a and b are vectors of incident and reflected waves, respectively, and S is an N-by-N matrix of complex coefficients.

In the case of a two-port network, the relationship between the incident and reflected waves can be expressed as $b_1 = s_{11}a_1 + s_{12}a_2$ and $b_i = \frac{1}{2}k_i(V_i - Z_i^* I_i)$. Here, s_{11} is the input port voltage reflection coefficient, which measures the amount of incident voltage that is reflected to the source. The reverse voltage gain, s_{12}, measures the amount of voltage from port 2 that is fed back into port 1. The forward voltage gain, s_{21}, measures the amount of voltage from port 1 that is transmitted to port 2. Finally, the output port voltage reflection coefficient, s_{22}, measures the amount of reflected voltage at port 2.

In designing a microwave imaging system for brain stroke detection, understanding the behaviour of the multiport network and the S-parameter matrix is crucial for optimizing the performance of the system. By carefully selecting the impedance of each port and using the appropriate coupling methods, it is possible to minimize losses and optimise the signal-to-noise ratio, leading to improved imaging resolution and accuracy.

3. Maxwell Equation and Dielectric Property

Maxwell's equations mathematically describe the properties of electric and magnetic field. Having brought electricity, magnetism, and optical phenomena, together into one unif ied theory, Maxwell formulated the relationships between varying electric and magnetic fields systematically. Considering the differential and integral formulations are mathematically equivalent, we mention differential form here for brevity.

Gauss' s law: $\vec{\nabla} \cdot \vec{E} = \rho$

Gauss' s law in magnetism: $\vec{\nabla} \cdot \vec{B} = 0$

Faraday's Law: $\vec{\nabla} \times \vec{E} = -\frac{\partial \vec{B}}{\partial t}$

Ampere's Law: $\vec{\nabla} \times \vec{H} = -\frac{\partial \vec{D}}{\partial t} + \vec{J}$

where $\vec{E}$ is electric field with MKS units $\frac{V}{m}$, $\vec{H}$ is magnetic intensity with the units $\frac{A}{m}$, $\vec{D}$ is the electric displacement with the units of $\frac{C}{\mathrm{m}^2}$, $\vec{B}$ is the magnetic flux density, with units $\frac{Wb}{\mathrm{m}^2}$, $\vec{J}$ is the electric current density in $\frac{A}{\mathrm{m}^2}$ and ρ is the electric charge density with the units of $\frac{C}{\mathrm{m}^3}$.

The following constitutive equations describe the relations between the magnetic intensity, magnetic flux density and the electric displacement.

$$\vec{D} = \varepsilon \vec{E}$$

$$\vec{B} = \mu \vec{H}$$

$$\vec{J} = \sigma \vec{E}$$

,where ε is the permittivity of the medium in $\frac{\text{Farad}}{m}$, ε_0 is the permittivity in vacuum $4\pi \times 10^{-7}$ $\frac{\text{Henry}}{m}$, μ is the permeability of the medium in $\frac{\text{Henry}}{m}$. σ is the material conductivity in $\frac{S}{m}$.

When applying an electric field on dielectric materials, the dipoles in the medium are polarised, which gives rise to electric displacement, we can write:

$$\vec{P}=\varepsilon_0\chi\vec{E}$$

$$\vec{D} = \varepsilon_0\vec{E} + \vec{P}$$

,where $\vec{P}$ electric polarisation or the sum of all the induced dipoles in the medium, χ is the electric susceptibility.

The complex permittivity of lossy dielectrics of printed antenna components and human tissues are given by

$$\varepsilon = \varepsilon_r(1 - jtan\delta)\varepsilon_0$$

where ε_r is the relative permittivity of material, tan δ is the loss tangent and ε0 is the permittivity of free space.